Applied Research Laboratory

Technical Report

Design and Testing of an Erosion Resistant Ultrasonic De-Icing System for Rotorcraft Blades

by
Jared T. Soltis, Dr. Jose Palacios and
Dr. Douglas E. Wolfe

Approved for public release, distribution unlimited.

PENNSTATE

The Pennsylvania State University
The Applied Research Laboratory
P.O. Box 30
State College, PA 16804

Design and Testing of an Erosion Resistant Ultrasonic De-Icing System for Rotorcraft Blades

By
Jared T. Soltis and Dr. Douglas E. Wolfe

Technical Report No. TR 14-007
August 2013

Supported By:

Applied Research Laboratory, Exploratory and Foundational Research Program

Approved for public release, distribution unlimited

REPORT DOCUMENTATION PAGE	Form Approved OMB No. 0704-0188

The public reporting burden for this collection of information is estimated to average 1 hour per response, including the time for reviewing instructions, searching existing data sources, gathering and maintaining the data needed, and completing and reviewing the collection of information. Send comments regarding this burden estimate or any other aspect of this collection of information, including suggestions for reducing the burden, to the Department of Defense, Executive Service Directorate (0704-0188). Respondents should be aware that notwithstanding any other provision of law, no person shall be subject to any penalty for failing to comply with a collection of information if it does not display a currently valid OMB control number.

PLEASE DO NOT RETURN YOUR FORM TO THE ABOVE ORGANIZATION.

1. REPORT DATE *(DD-MM-YYYY)*	2. REPORT TYPE	3. DATES COVERED *(From - To)*
06-18-15	Technical Report	August 2013-June 2015

4. TITLE AND SUBTITLE
Design and Testing of an Erosion Resistant Ultrasonic De-Icing System for Rotocraft Blades

5a. CONTRACT NUMBER

5b. GRANT NUMBER

5c. PROGRAM ELEMENT NUMBER

6. AUTHOR(S)
Jared T. Soltis
Douglas E. Wolfe

5d. PROJECT NUMBER

5e. TASK NUMBER

5f. WORK UNIT NUMBER

7. PERFORMING ORGANIZATION NAME(S) AND ADDRESS(ES)
Applied Research Laboratory
The Pennsylvania State University
PO Box 30
State College, PA 16804

8. PERFORMING ORGANIZATION REPORT NUMBER
TR 14-007

9. SPONSORING/MONITORING AGENCY NAME(S) AND ADDRESS(ES)
Defense Advance Research Projects Agency
Tactical Technology Office
675 N. Randolph Street
Arlington, VA 22203-2114
Attn: Kevin Massey

10. SPONSOR/MONITOR'S ACRONYM(S)
DARPA

11. SPONSOR/MONITOR'S REPORT NUMBER(S)

12. DISTRIBUTION/AVAILABILITY STATEMENT
Approved for Public Release: distribution unlimited

13. SUPPLEMENTARY NOTES

14. ABSTRACT
See attached

15. SUBJECT TERMS

16. SECURITY CLASSIFICATION OF:			17. LIMITATION OF ABSTRACT	18. NUMBER OF PAGES	19a. NAME OF RESPONSIBLE PERSON
a. REPORT	b. ABSTRACT	c. THIS PAGE			Douglas E. Wolfe
Unclassified	Unclassified	Unclassified	UU	102	19b. TELEPHONE NUMBER *(Include area code)* 814-865-0316

20151210106

The Pennsylvania State University

The Graduate School

College of Engineering

DESIGN AND TESTING OF AN EROSION RESISTANT ULTRASONIC DE-ICING SYSTEM FOR ROTORCRAFT BLADES

A Thesis in

Aerospace Engineering

by

Jared T. Soltis

© 2013 Jared T. Soltis

Submitted in Partial Fulfillment
of the Requirements
for the Degree of

Master of Science

August 2013

Approved for public release; distribution unlimited

The thesis of Jared T. Soltis was reviewed and approved* by the following:

Jose L. Palacios
Thesis Co-Advisor
Research Associate

Douglas Wolfe
Thesis Co-Advisor
Associate Professor of Materials Science and Engineering

Edward Smith
Professor of Aerospace Engineering

George A. Lesieutre
Professor of Aerospace Engineering
Department Head of Aerospace Engineering

*Signatures are on file in the Graduate School

Abstract

The goal of this research was to design a helicopter rotor blade lead edge that had high sand erosion resistance and was conducive to ultrasonic ice protection systems (IPSs). The first section of research tried to tailor the leading edge to promote ice interfacial transverse shear stress created by the ultrasonic vibration of piezoelectric actuators. Previous work done to tailor leading edges removed material from the inside of the cap. However, there were concerns about structural integrity and erosion wear when material was removed. A new system of adding material to the inside of the leading edge instead of removing material to create stress concentrations was researched for this thesis. Finite element analysis was used to determine the optimal locations for the discontinuities for the ultrasonic IPS. The discontinuities located in the optimal location are called Tailored Stress Concentrators (TSCs). Using the finite element results, it was determined that the best location for the TSCs were in regions of normally low stress in the baseline model before the addition of the TSCs. The addition of the TSCs creates stress concentrations as well as increased the original local maximum stresses. Initial models showed increases in average interfacial shear stress of 20%. Since the first FEM was not practical to construct as a bench top experiment, a second model was developed. Next, a bench top experiment and matching finite element model were built to validate the finite element analysis. The finite element model predicted a decrease of 9% in interfacial shear stress when TSCs were added to the bench top model. The bench top experiments confirmed the ineffectiveness of TSCs. There was no reduction in power required to de-ice when the TSCs were added to the bench top model.

The next part of the research focused on the material used for the leading edge erosion cap. Coating systems based on titanium nitride (TiN) applied via cathodic arc physical vapor deposition (CA-PVD) were developed for rotorcraft erosion caps to protect against sand and rain erosion. Erosion resistant materials must also be compatible with ice protection systems. The ice adhesion strength of titanium nitride and titanium aluminum nitride (TiAlN) were evaluated experimentally and compared to the ice adhesion strength of uncoated metallic materials currently used on rotor blade leading edge caps: stainless steel 430, Inconel 625, and titanium grade 2. Experimental studies presented in this paper

investigated which environmental and material parameters are most influential on impact ice adhesion strength. The effects of median volumetric diameter, liquid water content, ambient temperature, surface roughness, and material grain direction were tested on stainless steel 430. Tests revealed that surface roughness and temperature have the greatest effect on ice adhesion strength. There was an increase in adhesion strength of 670% from -8°C to -16°C and 250% increase from 24 *Ra* μin to 105 *Ra* μin. An increase in water droplet size from 20 μm to 40 μm decreased the ice adhesion strength by 65%. The adhesion strength increased 15% when shear forces were applied 90° with respect to the grain direction as compared to a 0° loading configuration. While inside the Federal Aviation Regulation Part 25 and Part 29 Appendix C icing envelop for liquid water content, an increase from 0.5 to 2 g/m^3 had a 7% reduction in ice adhesion strength. A test matrix to evaluate ice adhesion strength of erosion resistant materials was developed, investigating the effects of temperature and coating surface roughness. An empirical extrapolation method to predict ice adhesion strength with varying temperature is presented and validated on metallic materials. The data for each material was reduced down to an average adhesion strength over the test conditions. The average ice adhesion for the TiAlN and TiN coatings together was 51.5% higher than the three uncoated metallic materials together. Titanium aluminum nitride has the highest average adhesion strength of 75.1 psi and titanium grade 2 has the lowest with 36.9 psi over all of the test conditions.

The final phase of research compared a modern electrothermal IPS to a one of a kind laboratory test model for a ultrasonic IPS with a TiAlN coating on a 0.04" titanium grade 2 leading edge in the Adverse Environment Rotor Test Stand. The IPSs were evaluated for power required to de-ice and de-icing effectiveness. Both de-icing systems were tested at two different icing conditions. The ultrasonic IPS required 289 W at -15°C and 243 W at -8°C. The ultrasonic IPS was able to de-ice the majority main ice shape and some of the ice feathers at both temperatures. When the electrothermal IPS was tested at similar powers as the ultrasonic IPS, the electrothermal system de-iced as well as the ultrasonic system. Lastly, the electrothermal system was tested at a more typical higher power of 416 W. At the higher power, the electrothermal system was able to remove all of the ice at -8°C and all but a few feathers at -

15°C. The ultrasonic system could not be tested at higher powers due to the fracture limit of the actuator. Actuator failure was observed at high applied voltages and power.

Contents

List of Figures

List of Tables

Acknowledgments

I would like to sincerely thank my advisor and mentor Jose Palacois for his time and dedication to my Masters of Science degree program. He has been indispensable over the last two years helping me design and run my experiments and computer models and teaching me about, sensors, actuators, data acquisition, and LabVIEW. Without his guidance and expertise my research would not have been a success. I would not have been able to complete my degree without my second advisor Douglas Wolfe. His expansive knowledge of material sciences and advanced coatings made it possible to research state of the art erosion resistant materials. Since I have little knowledge in the world of material science and coatings, Dr. Wolfe's teachings were a great help. The last key player in my degree was Edward Smith. His vast experiences in the rotorcraft industry made my research stronger though his recommendations and critiques. I am also grateful for the time and recommendations given by my fellow graduate students Austin Overmeyer and Nic Diplacido.

I would also like to thank the Pennsylvania State University Applied Research Laboratory for the Walker Graduate Assistantship program and the Vertical Lift Consortium for funding my academic and research endeavors. This project was funded by NASA Leading Edge Aeronautics Research Grant Number NNX13AB78A and the Vertical Lift Consortium, formerly the Center for Rotorcraft Innovation and the National Rotorcraft Technology Center (NRTC), U.S. Army Aviation and Missile Research, Development and Engineering Center (AMRDEC) under Technology Investment Agreement W911W6-06-2-0002, entitled National Rotorcraft Technology Center Research Program. The authors would like to acknowledge that this research and development was accomplished with the support and guidance of NASA, NRTC and VLC. The views and conclusions contained in this document are those of the authors and should not be interpreted as representing the official policies, either expressed or implied, of the AMRDEC or the U.S. Government. The U.S. Government is authorized to reproduce and distribute reprints for Government purposes notwithstanding any copyright notation thereon.

1. Introduction

1.1. Icing Overview

1.1.1. Aircraft Ice Testing History

Aircraft icing was not a concern for early aviators, mainly because the lack of technical instrumentation meant that pilots had to fly by Visual Flight Rules (VFR), thereby avoiding flying though clouds. With the advent of flight instrumentation in the mid 1920s, pilots started to increase the flying envelope to include Instrument Flight Rules (IFR). As part of their efforts to keep service on time, the U.S. Air Mail Service was the first group to fly in IFR conditions and encounter icing on the New York-Chicago route. In their opinion, these pilots deemed icing the greatest hazard of their flights (1).

Given this new problem of aircraft icing, the National Advisory Council for Aeronautics (NACA) began testing the first icing wind tunnel at Langley in 1928. Two nozzles up stream of the test chamber injected water particles into the airflow to create an artificial cloud. The two major downsides to this first icing wind tunnel were the small size of the test section, only six inches in diameter, and the inability to create small representative water particle sizes. Commercial nozzles at the time could not create natural icing conditions. In the spring of 1942, the NACA started construction of the 6 ft by 9 ft Icing Research Tunnel (IRT) at then the Aircraft Engine Research Laboratory, now NASA Glenn, in Cleveland Ohio. The IRT is a modified version of the 7 ft by 10 ft tunnel at NACA Ames in California. In the event the Germans attacked NACA Ames during WWII, the IRT could run the same experiments. In August 1942, the first icing experiments were conducted on a propeller at the IRT, signaling the beginning of icing research and development (1).

Since the construction of the IRT, many private icing wind tunnels have been built: the Boeing Aerodynamic Icing Tunnel (2), Goodrich Icing Tunnel (3), Cox Icing Tunnel (4), and the Icing Wind Tunnel at CIRA in Italy (5). Other facilities have been built for full-scale helicopter icing testing: the NRC Spray Rig (currently closed) (6), Helicopter Icing Spray System (HISS) (7), and the McKinley Climatic Laboratory (8). The Pennsylvania State University Adverse Environment Rotor Test Stand

(AERTS), established in November 2009, is a hover test stand for small scale rotor testing in icing conditions (9)(10)(11).

The scope of testing abilities of these facilities ranges from flight certification to fundamental physics, including ice protection prototype testing. Although much has been learned about icing physics since the construction of the IRT, de-icing systems still consume a lot of power, and research into more efficient ice protection systems is recommended.

1.1.2. Ice Accretion Physics

As aircraft fly through icing clouds, super-cooled water droplets impact the aircraft and ice accretes. Super-cooled water is water below the freezing point but has not yet frozen. This occurs in pure water when there is no seed crystal to build upon. To create these conditions in the laboratory, water is purified through a reverse osmosis filtration system to remove all impurities. In order to create an artificial icing cloud, the purified water and air are pumped through a series of nozzles that aerosolize the water. The number of active nozzles and the difference between the air and water pressure controls the amount of water and the size of the water droplets in the icing cloud (4). The shape of the ice and rate at which the ice accretes on the aircraft is dependent upon a number of atmospheric conditions in the icing cloud and airspeed. The parameters controlling ice accretion are the atmospheric temperature, droplet size, water content in the cloud, and accretion time. The droplets in the cloud have a distribution of sizes, so the particle size is defined by the median volumetric diameter (MVD) of the particles in the cloud in μm (12). The water content in the cloud is defined as liquid water content (LWC) in g/m^3. Ambient temperature, MVD, and LWC parameterize the icing envelope. The Federal Aviation Administration (FAA) has defined two icing envelopes in the Federal Aviation Regulations Part 25 and Part 29 Appendix C for aircraft and rotorcraft respectively (13). The icing standard is the same for both fixed-wing aircraft and rotorcraft. The icing envelope is defined by the ambient temperature, the MVD of the water droplets, and the LWC of the cloud. The relationship between the three atmospheric parameters determines the icing condition; the greater the LWC, the higher the icing accretion severity. The icing envelope is

divided into continuous and intermittent icing. During continuous icing, less severe icing conditions are seen by the vehicle, as shown in Figure 1. The LWC ranges from 0.06 g/m^3 to 0.8 g/m^3, and the MVD ranges from 10 μm to 40 μm (13).

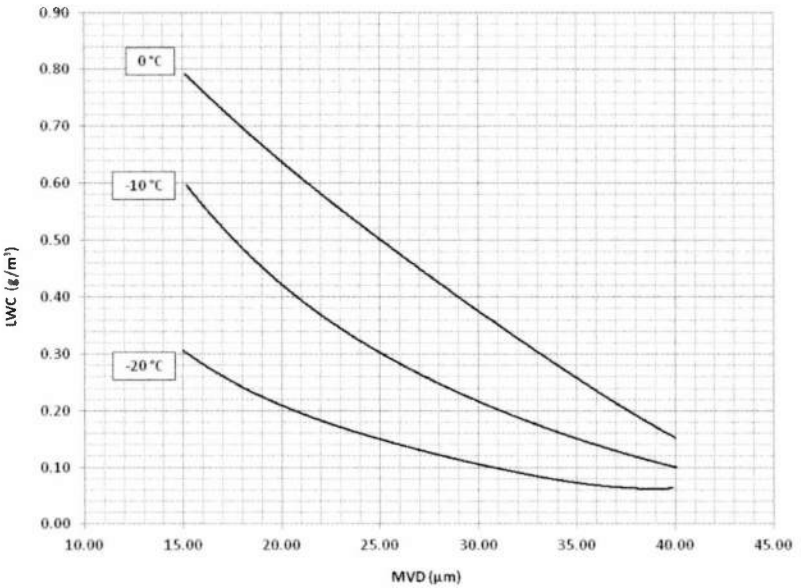

Figure 1: Continuous icing envelope (13)

During icing encounters, high severity conditions could be experienced for a short time. These high ice accretion rates occur intermittently. The intermittent icing envelope is shown in Figure 2. The LWC ranges from 0.3 g/m^3 to 2.9 g/m^3, and the MVD ranges from 15 μin to 50 μin. These icing envelopes must be used in all artificial icing test facilities to create conditions representative of natural icing (13).

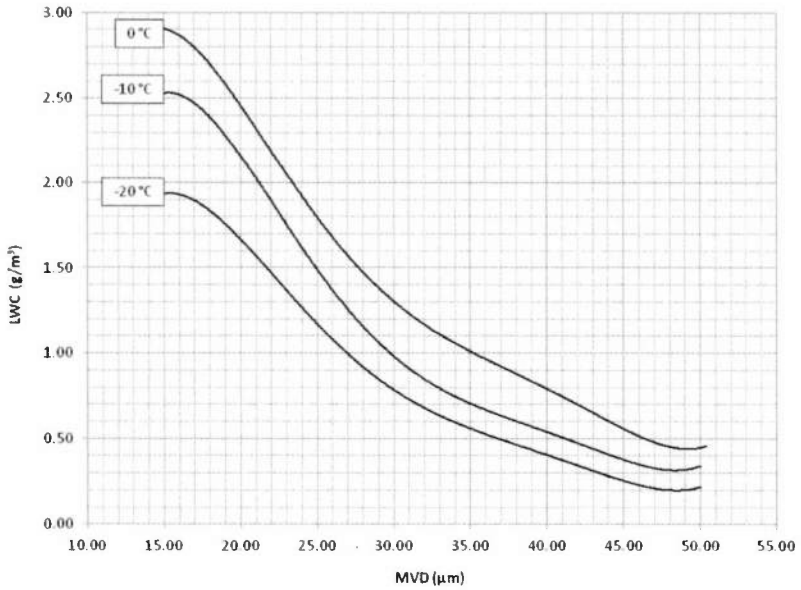

Figure 2: Intermittent icing envelope (13)

There are three icing regimes that accrete on aircraft wings: glaze, mixed, and rime. Predicting what ice regime will accrete is a difficult task because the regime has a complex dependency on temperature, LWC, and MVD. A loose guide line is presented in Figure 3. It is easier to classify the ice regime after the ice has accreted (Figure 4). Glaze ice is typically characterized by a clear ice color and the large protrusions known as horns. The glaze ice regime is normally encountered at relatively warm temperatures, large MVDs, and high LWCs. As depicted in Figure 5, when the droplets impact the surface, the water has a chance to splash and run along the surface before freezing. At the other end of the regime spectrum is rime ice. Rime ice conforms tightly to the shape of the object that it accretes on and has an opaque color. The color is due to air pockets trapped within the ice since the droplets freeze on impact. Rime ice is typically encountered at cold temperatures, small MVDs, and low LWCs. There is no distinct line where the ice regime changes from glaze to rime due to many complex conditions (14). The transition between glaze ice and rime ice is the mixed ice regime. Typically, the main ice shape is clear like the glaze regime, and the feathers aft of the main ice shape are rime in nature (12).

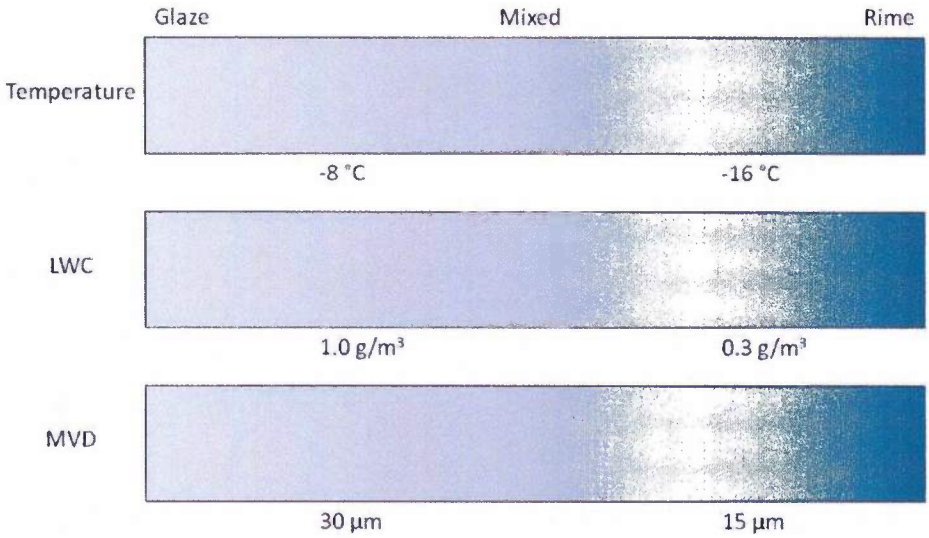

Figure 3: General guide lines for ice regime

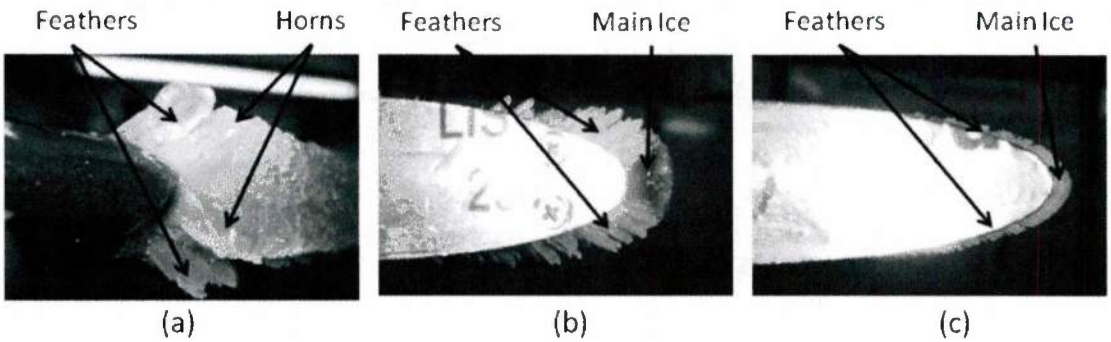

Figure 4: Ice regimes glaze (a), mixed (b), and rime (c)

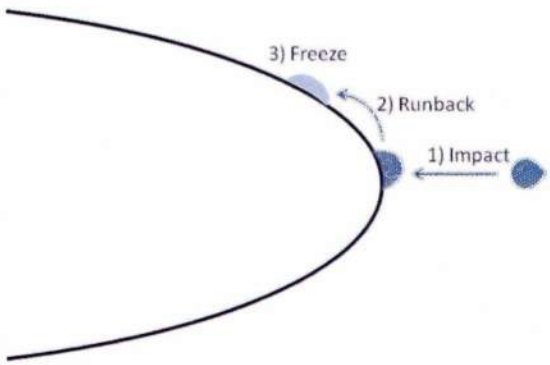

Figure 5: Glaze ice process

1.1.3. Rotorcraft Icing Issues

As ice accretes on the rotorcraft blades, the aerodynamic performance of the aircraft is greatly degraded. As ice on the blades sheds unevenly, the imbalance created by centrifugal forces on the rotor can create high vibratory loads. The excessive loads can damage the rotor and make piloting the craft difficult.

Recent wind tunnel experiments performed by Han et al. determined the change in lift, drag, and pitching moment coefficients due to ice accretion on a NACA 0012 airfoil (14). The ice accretion tests were conducted in the Pennsylvania State University Adverse Environment Rotor Test Stand. Then, the ice shape was cast in hard plastic and tested in a wind tunnel. One of the ice shapes tested can be seen in Figure 6. The ice in the case shown below was accreted at -9.7 °C, 58.1 m/s, 20 μm MVD, and 2.1 g/m^3 LWC for 5 minutes with no angle of attack (14).

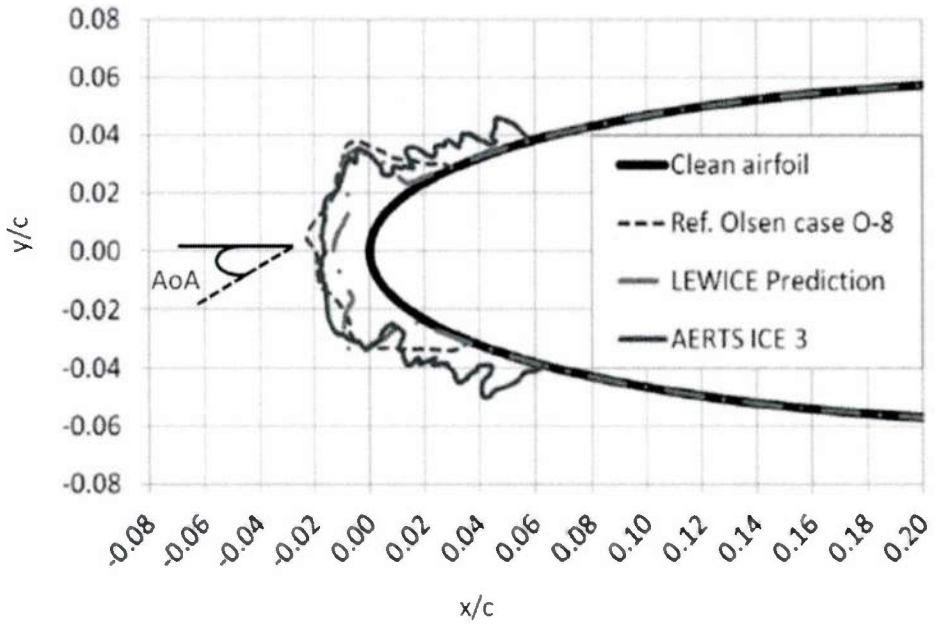

Figure 6: Ice shape used for aerodynamic performance experiments (14)

The comparison of the aerodynamic performance with and without the ice can be seen in Figure 7. At angles of attack (AoA) below 6°, there was a factor of five increase in drag due to the ice shape at the leading edge. At AoAs greater than 6°, there was a dramatic increase in the drag coefficient (C_d).

form the Right before stall at an AoA of 15°, the drag measured with a wake survey (2D) for this specific icing case was nine times higher than the clean airfoil. An increase in drag will increase the required rotorcraft torque and power required to maintain a flying condition. At AoAs below 6°, there was a small decrease in lift coefficient (C_l), and as the AoA increases there was more of a C_l deficit. Right before stall at an AoA of 15°, there was a 35% decrease in C_l. The decrease in lift will also drive up the power required to fly. If the power required increases above the available power, the aircraft will no longer be able to maintain the flying condition and will have to descend. Without the ice, the pitching moment coefficient C_m was relatively constant until stall. With ice accretion in the leading edge, the C_m was very dependent on AoA. This will change the blade dynamics (14).

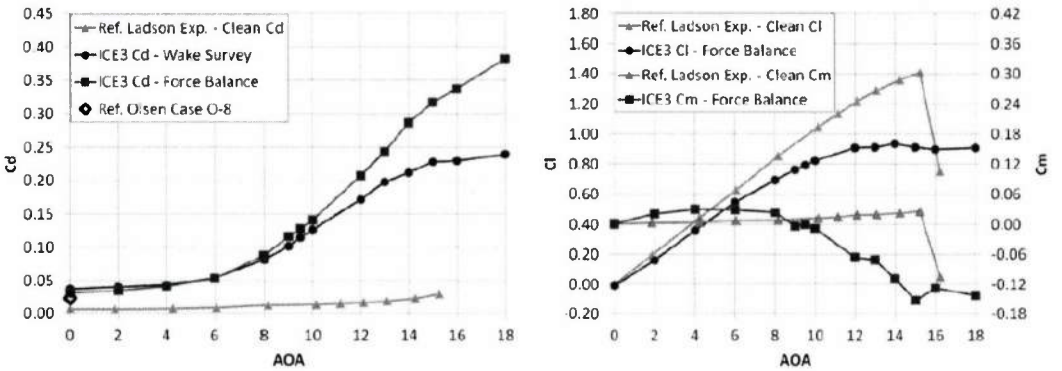

Figure 7: C_d vs AoA and C_l vs AoA for a NACA 0012 with and without ice (14)

If the rotor blades do not have an ice protection system, a large mass of ice can accrete prior to natural shedding due to centrifugal forces. It is very unlikely that the ice will shed uniformly from every blade. The subsequent imbalance will induce very high 1/rev vibration loads through the hub. The vibrations will most certainly be uncomfortable for the pilot and passengers, and in extreme cases cause damage to the aircraft (15).

1.1.4. Ice Protection System

1.1.4.1. Low Ice Adhesion Coatings

Low ice adhesion coatings have wide spread use and are the only passive ice mitigation technique. The lower the ice adhesion strength to the surface, the faster the ice will naturally shed. If an aircraft cannot afford an active ice protection system (IPS) or if the active system fails, a low-adhesion coating would minimize the amount of ice buildup before the ice naturally sheds. This category of materials is sometimes referred to as icephobic. Some icephobic coatings display poor erosion characteristics over time. Rotorcraft cannot afford to compromise erosion protection for a low-adhesion coating on the leading edge of the blades, so any potential coating must be tested before and after erosion to evaluate the coating effectiveness.

A combined effort between the US Army Aviation Applied Technology Directorate, Boeing Rotorcraft, and Pennsylvania State University tested a wide range of potential leading edge materials for ice adhesion strength under the Rotor Durability Army Technology Objective. Testing revealed the icephobic coatings worked relatively well early in life; however, the coatings degraded significantly over time due to erosion, and the adhesion strength increased by more than a factor of five (16).

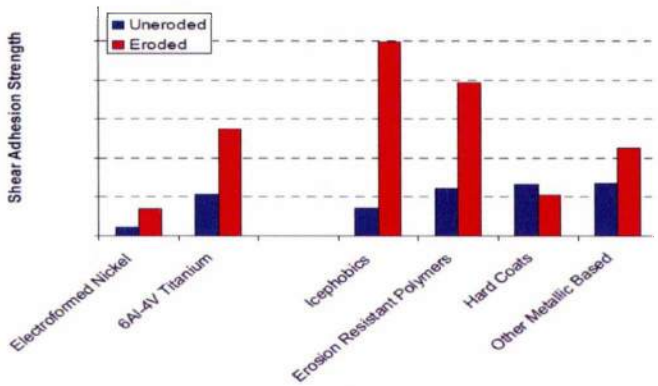

Figure 8: Comparison of adhesion strength for potential leading edge materials (16)

A specific example of an icephobic coating is the silicone coating developed by NuSil, a silicon manufacturer. The NuSil coating R-2180 has significantly lower ice adhesion strength as compared to other commercial coatings. A paper presented by NuSil at the 2012 AHS International forum shows the R-2180 coating had an adhesion strength 27 times lower than titanium and 14 times lower than stainless steel, two typical helicopter blade leading edge materials. However, at the time of this publication, the NuSil coating had not yet been tested for erosion characteristics nor was the surface roughness values of the materials presented (17).

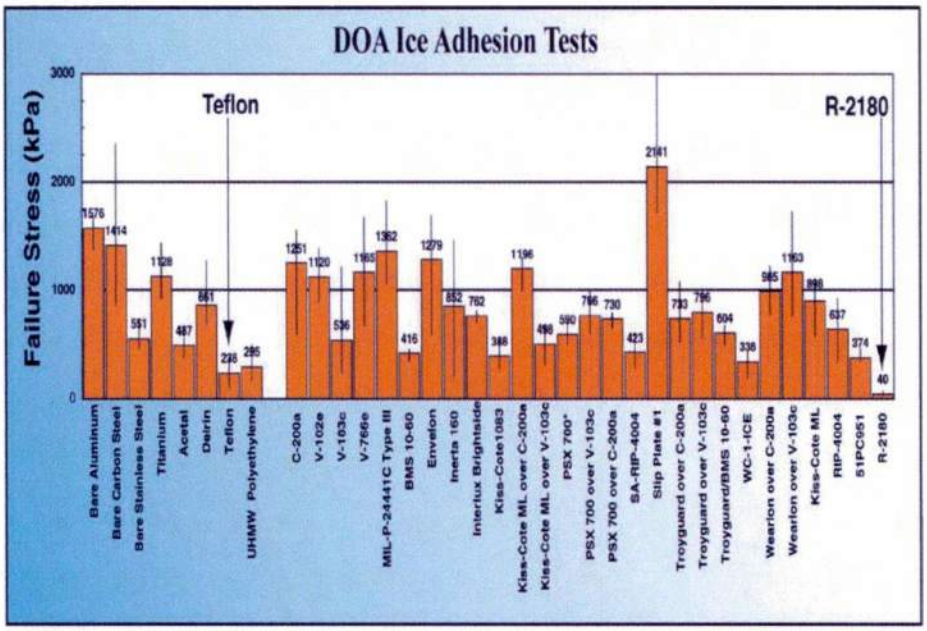

Figure 9: Comparison of adhesion strength for commercial coatings to the NuSil R-2180 coating (17)

1.1.4.2. Fluid Anti-Icing Systems

In the early 1960's, Bell Helicopter developed a fluid anti-icing system for the UH-1 Huey helicopter main rotor and tail rotor. By pumping fluid through a porous leading edge and letting the fluid flow down the span of the blade, the Bell scientists were able to continually and reliably prevent ice accretion. In addition to anti-icing, the fluid IPS could work in a de-icing mode. Ice was allowed to accrete up to a thickness of 0.3 inches before the fluid was pumped out and the ice shed. A mixture of alcohol and glycerin was held in an 11-gallon reservoir. From there, the fluid was pumped to the main

rotor and tail rotor blades using a 43 gal/hr pump at 15 psi. A pneumatic slinger ring was used to move the fluid from the fixed frame of the aircraft to the rotating blades. A schematic of the system can be seen in Figure 10. The system was successfully tested at the Ottawa spray rig at a temperature of -20°C and an LWC of 0.8 g/m^3 (18).

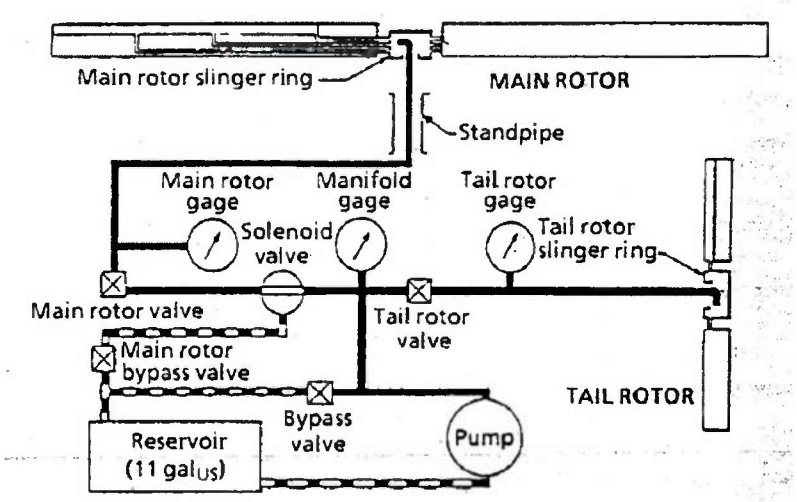

Figure 10: Fluid Anti-icing System Schematic (18)

The benefits of this fluid IPS include a low power requirement, the absence of water runback that can freeze in unprotected areas of the blade, and the ability for the system to both anti-ice and de-ice. The disadvantage of the fluid IPS is the weight and volume required, the short operational time, the need for pneumatic slip rings, and the potential of holes located on the blade to clog. The 11-gallon tank adds significant weight and only protects against ice accretion for 84 minutes. Bell Helicopter recommended that the fluid IPS development continue for production on the UH-1, but funding was never made available (18).

1.1.4.3. Electrothermal

Electrothermal IPSs are the most common IPS and the only type of IPS currently used for rotorcraft (18). They use the Joule heating effect to convert electric energy into thermal energy, in effect melting the ice interface and promoting shedding. A heating element is typically bonded to the back surface of the leading edge skin, which provides protection from erosion. When a voltage is applied to the

heater element, the heat is conducted from the element though the skin, and ultimately to the ice interface. When this technology initially was developed, foil and wires were laid in a grid pattern to evenly distribute the heat. However, current metallic heaters are being replaced by carbon fiber composites, and the next generation elements may introduce carbon nano tubes (CNT) (19). Electrothermal IPSs can run in an anti-icing mode but typically run in a de-icing mode due to power requirements and water run back.

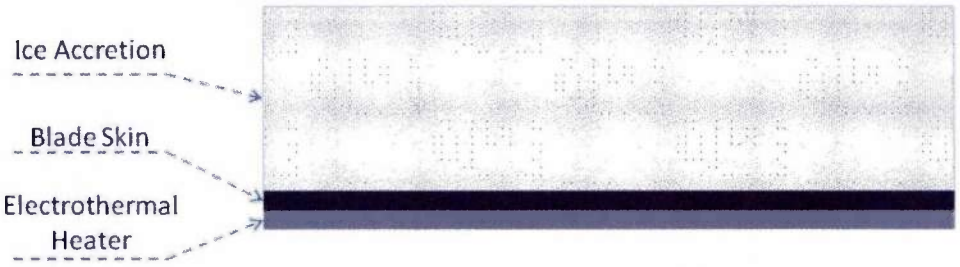

Figure 11: Simplified electrothermal IPS schematic

The disadvantages of electrothermal IPSs are the potential for water runback towards unprotected areas of the blade (trailing edge region), the hefty power requirements, and the overall weight of the system. If the heaters are not cycled properly, water from the melted ice can run and freeze on unprotected areas (18). The run back ice will slowly build a wall and severely degrade aerodynamic performance as mentioned in the previous section. The heaters also require high power, around 25 W/in^2 (20). To minimize the power draw, the heaters are broken up into span-wise or chord-wise elements, and the elements are cycled. To supply the extra power required, a large supplemental auxiliary must be added to the aircraft (18).

In the late 1970's through the early 1980's, Sikorsky developed an IPS for the engine inlet and rotor blades for the UH-60 Black Hawk. The US Army required that the helicopter be able to operate in icing conditions with temperatures as low as -20°C and LWSs of up to 1.0 g/m^3. The first design only protected the outboard section of the blades with four chord wise heater elements, all four blades being powered at the same time. Flight tests in Alaska in 1976 led to the qualification of the engine inlet IPS, but torque increases due to ice accretion on the unprotected inboard section forced a redesign of the rotor

blade IPS. When the heaters were extended to protect the entire length of the blades, the blades could only be powered in pairs to reduce the power required to 25 W/in^2. Six hours of flight-testing in artificial icing conditions behind the US Army's CH-47 Helicopter Icing Spray System (HISS) from 1979 to 1980 and 20 hours of natural icing conditions in Minnesota from 1979 to 1981 confirmed the ability of the eletrothermal IPS to protect the UH-60 Black Hawk (20).

An example of a nonconventional electrothermal IPS is the Goodrich Low Power Electrothermal De-icing (LPED) system. LPED does not continuously send AC or DC electricity to the heating elements for a predetermined amount of time and zone pattern like a conventional system. During the winter of 2003 and 2004, LPED was flight-tested on a fixed wing aircraft. LPED was designed with an anti-icing parting strip at the stagnation point of the airfoil and de-icing zones aft of the parting strip. The parting strip was cycled from the 28 volt electric system native to the airplane to maintain the stagnation area free of ice, and the runback water from the parting strip froze on the de-icing zones. Resistance temperature devices (RTD) monitored the temperature of the parting strip, and the parting strip heater element was limited to 220°F. The de-icing zones were powered by a pulse of energy from a bank of 3500 farad capacitors. The capacitors discharge into the de-icing zones in 1.4 seconds every three minutes. As a result, LEPD was able to effectively protect the aircraft in icing conditions for 20% to 50% less power than a conventional system (21).

The latest conventionally powered electrothermal IPS currently being developed is a carbon nanotube (CNT) IPS. CNTs are fabricated and patched together to make a heater element. The manufacturing process goes as followed: CNTs between 80 μm to 100 μm tall are first grown on silicon wafers. Then, a sheet of guaranteed nonporous Teflon is placed over the CNTs and a steel tool with a small radius knocks down and compresses the CNTs in the plane of the Si-wafer to create a heater element patch. During 2013 testing, the patches were placed next to one another on a sheet of epoxy film and cured to build larger heater elements. Two heaters were bonded to the surface of a wing section and tested in the Cox & Company wind tunnel. The CNT IPS was tested at temperatures from 25°F to -5°F

and used power ranges from 0.6 W/in^2 to 5 W/in^2. The CNT IPS was able to anti-ice and de-ice; however, there were issues with ice bridging to unprotected areas and islands of ice building up (19).

1.1.4.4. Microwave

Microwave IPSs were tested by the US Army Research and Technology Laboratories at Fort Eustis Virginia in the mid 1970's and in Germany by Lambert Feher and Manfred Thumm in 2001 (22) (23). Both tested 2.45 GHz and 22 GHz microwaves to try to melt the ice off the leading edge of aircraft. It was found that pure ice absorbs negligible amounts of 2.45 GHz radiation and anti-icing was not practical due to power concerns; therefore, a system using higher frequencies would be more efficient at heating the ice (23). Performance improved at 22 GHz due to the higher concentration of energy in the ice (22). Glass fiber reinforced composite (GFRP) and carbon fiber reinforced composite (CFRP) are the two primary composite variants used in aerospace structures. For this reason, GFRP and CFRP reactance to microwaves was studied. There is little signal attenuation though GFRP, so it is more effective if the goal of the IPS is to emit the microwaves through the structure so the ice can absorb them. CRFP does attenuate the signal by 30 dB, so it is better as an electrothermal heater (23). Microwave radiation was a concern due to detectability of the vehicle.

1.1.4.5. Pneumatic

Pneumatic IPSs have been designed for rotorcraft blades that have power and weight limitations. The main issue encountered by pneumatic de-icing for helicopter rotor blades is erosion. Prototype pneumatic boots (similar to those used in fixed-wing configurations), developed by Goodrich, were fitted to the leading edge of the main rotor blades of a UH-1 in a chord-wise and span-wise orientation as seen in Figure 12. Bleed air from the turbine engine was used to inflate the boots in 2 seconds. When inflated, the boots create transverse shear stress at the ice interface due to the large displacement, and the accreted ice was delaminated. The prototype pneumatic IPS could de-ice the blades at temperatures down to -20°C

and LWCs as high as 0.8 g/m^3. It was also determined that a minimum ice thickness of 0.3 inches is required for effective and reliable de-icing (18).

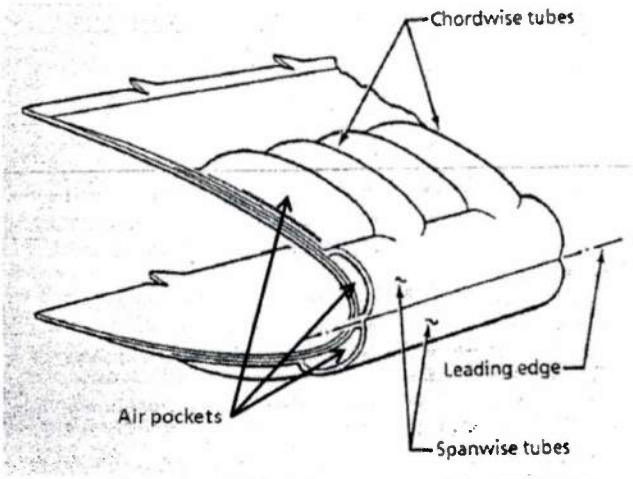

Figure 12: Pneumatic boot arrangement for UH-1 (18)

To combat the adverse effects that rain erosion has on the boots of the pneumatic IPS, Goodrich developed and tested a composite boot. On top of the stretchable fabric used to create the air pockets was a layer of natural rubber followed by a weathering surface. The stiffness of the rubber helped to push out the air after the ice was removed, and the weathering surface was designed for good rain erosion characteristics. While not in use, a vacuum was pulled on the boots to oppose the natural low pressure on the surface of the airfoil that would try to inflate the boots, so the boots maintain the desired aerodynamic shape. The drag increase from the inflated boots was not an issue since the drag due to the unshed ice is higher than the inflated boots. Another consideration was the natural shedding abilities of the elastomeric material. At higher boot thickness, the apparent adhesion strength of the ice decreases. This decrease was due to the creation of shear stress at the ice interface when the elastomer distorts under centrifugal loads (24). The drawbacks of pneumatic de-icing were the need of heavy pneumatic slip rings, and the need for a coating able to protect against both rain and sand erosion.

1.1.4.6. Electrovibratory

In 1978, Bell Helicopter and the US Army studied whether a shaker mounted at the root of a blade could induce vibrations strong enough to de-ice the blade. The shaker frequency matched the resonant frequencies of the blade to maximize deflection. As seen in Figure 13, there were four locations of interest for the shaker. A 0.5 hp motor drove a pair of 1.25 lb eccentric weights to create the vibrations. It was estimated that a flight-worthy vibratory system for a UH-1 would weigh 67 lbs and require 1.3kW of power. The test system was able to de-ice the blades from -5°C to -15°C. The shaker was activated for 2 seconds at up to 35 *g's*. The down side to the vibratory system was the weight of the shaker and the fatigue loads generated (18). Another similar system actively twists the blades with piezoelectric patches alone the blade (25). Rotor blade fatigue and aerodynamic effects related to blade vibration were a concern for the proposed system.

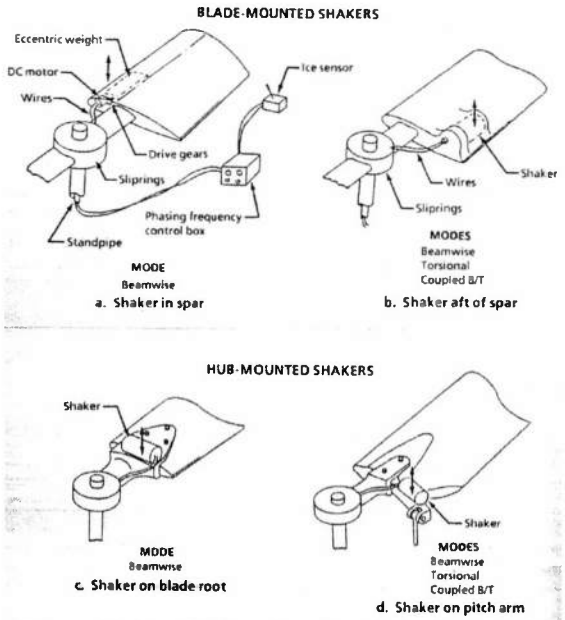

Figure 13: Possible locations for blade shaker (18)

1.1.4.7. Electroimpulsive

The heart of an electroimpulsive de-icing system is a coil of wires made of copper ribbon mounted to the spar or a beam attached to the ribs with a gap of 1 mm between the coil and the wing skin.

See Figure 14 for a coil mounting schematic. A bank of high voltage capacitors store the energy that is discharged into the coils. When the charge on the bank is released, a magnetic field grows and decays rapidly, creating an eddy current in the skin. The magnetic fields repel each other with a force of several hundred pounds at low displacements but very high accelerations. The two or three impulses will crack and delaminate the ice on the surface. The electroimpulsive IPS requires about 1 kW to protect a general aviation airplane and requires 3 kW to protect a medium sized helicopter. The difficulty in applying the electroimpulsive IPS to rotorcraft is that the blades are less compliant than fixed-wing aircraft wings. The leading edge of a rotor blade is solid to support banding loads and the leading edge of a fixed-wing can be hollow and the bending loads are carried more toward the middle of the blade. Removing leading edge material to make room for the coils and drilling holes for the wires, degrades the stiffness and fatigue capabilities of the blade (18).

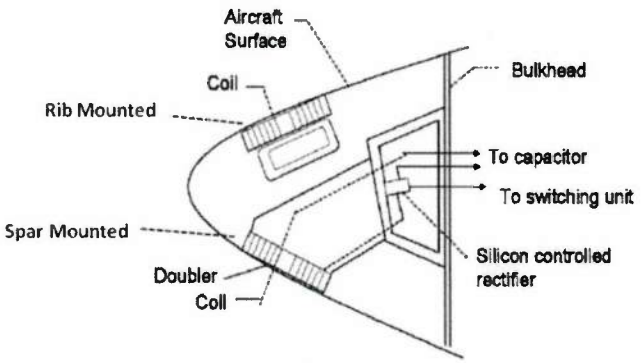

Figure 14: Coil mounting schematic (18)

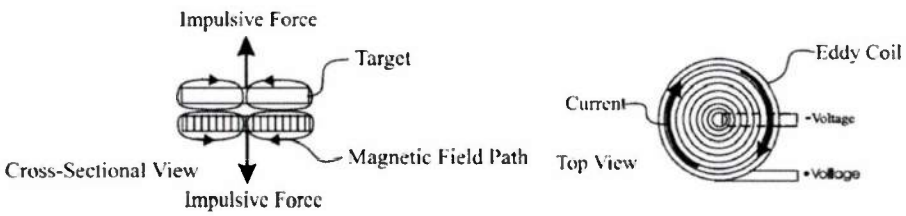

Figure 15: Magnetic force (left) eddy current (right) (26)

1.1.4.8. Piezoelectric Ultrasonic

A material that exhibits the piezoelectric effect will build a charge when strained. This direct effect is used to build sensors and energy harvesters. To build an actuator, the reverse piezoelectric effect is used. When an electric potential is applied across a piezoelectric material, the material will strain. One of the most popular piezoelectric materials is lead zirconium titanate (PZT). PZT-4 is a popular material to use as a de-icing actuator due to its larger stiffness and block force capability compared to other PZT materials (27)(28)(29). Early experiments and modeling of piezoelectric de-icing of leading edge skins drove shear actuators in the sonic range (1-1500 Hz) around the first few resonances of the structure. De-icing was achieved at temperatures of 5, 15, and 20 °F. The system did not delaminate the ice instantaneously, instead taking up to 251 seconds before the ice fully delaminated and shed from the airfoil at 5 °F (30). The long driving time and melting of the ice interface lends credit to the belief that the delamination was mainly caused by heating and not mechanical failure of the ice interface (31). The key to instantaneously delaminating the ice is to drive the actuators in the ultrasonic range around the natural frequency of the actuator. The first finite element models and experiments of an ultrasonic piezoelectric de-icing were performed by Palacios et al. on square steel plates with free-free boundary conditions with patches of freezer ice in 2011 (28). The models matched the impedance of the experiments and predicted that PZT shear disks driven around the first radial mode of the actuator (28.5 kHz) would produce interfacial transverse shear stresses that were greater than the ice adhesion strength. Experiments showed clear instantaneous cracking and delamination of ice patches for an input power of 50W (28).

To evaluate the ultrasonic de-icing system on a more representative aerostructures and impact of icing conditions, a NACA 0012 wing section with a 22 inch span and of 28 inch chord was modeled and tested in an icing wind tunnel. The finite element models were able to roughly predict the regions of ice that would delaminate. The experiment was run at -15°C, 1.5 g/m^3 LWC, 20 μm MVD, 67 m/s airspeed, and 3 degrees AoA. The de-icing system was able to delaminate 1 mm thick ice layers from the airfoil leading edge with an input power of 200W (70% less power than a comparable electrothermal de-icing

system) (29). During Palacios' tests, PZT actuator debonding and fracture was noted when the system was overpowered to promote ice delamination at colder ice regimes. The next improvement and step toward a robust ultrasonic de-icing system for rotorcraft blades came from Overmeyer et al. in 2011 (27). A driver program was developed by Overmeyer and it added a DC bias to the voltage sent to the actuators to drive the actuators in compression only. Since the tensile strength of PZT is higher in compression than extension, higher voltages can be applied to the actuator before it fails due to internal stresses created in the material. Finally, an ultrasonic de-icing system was designed and constructed around an NACA 0015 airfoil with a 12 inch span and 16 inch chord and spun at the end of a 4.5 foot rotor blade at the Pennsylvania State University Adverse Environment Rotor Test Stand. The de-icing system was able to remove ice over a wide range of icing conditions for a maximum input power of 185 W (27).

1.2. Erosion Overview

1.2.1. Helicopter Blade Sand Erosion Background

During take-off and landing, the down wash from the rotor blows sand, dirt, and debris into the air. The hard particulate impacts the leading edge of the blades and material can be removed. This process is called sand erosion. Erosion is a major concern for the military as a significant portion of the helicopter fleet operates in sandy environments in the Middle East, see Figure 16. Replacing helicopter blades is an expensive process costing approximately $500,000 per helicopter. In 2003, the US Army reported the cost of replacement rotor blades for the AH-64 Apache, CH-47 Chinook, and UH-60 Blackhawk was $189 million for that year. A large contributor to the blade damage was sand erosion (32).

Figure 16: CH-60 landing in the Ninawa province of Iraq (32)

During the life-time of the blades, the blade curvature is changing constantly as material is removed by subsequent hard particle impacts. The off design contour degrades the aerodynamic performance of the blades. Calvert at al. performed computational fluid dynamics (CFD) on a modified AH-64 Apache tail rotor section to study the aerodynamic degradation due to erosion (33). The base airfoil shape was an NACA 60-414. The CFD solver used was the unstructured Navier-Stokes FUN2D developed by NASA Langley Research Center. The non-dimensional, by chord length, outlines for the baseline and damaged airfoil sections can be seen in Figure 17. The most severely degraded section was the top surface from 5% to 35% of the airfoil chord and on the bottom surface between 8% and 22% of the airfoil chord. Figure 18 shows a plot of sectional lift and drag coefficients as a function of AoA for a blade section near mid span. The maximum sectional lift coefficient, $C_{l\,max}$, of the eroded section was reduced by 16%, and stall occurs 1 degree earlier, but drag of the eroded section did not increase until after stall. The linear decrease in sectional lift coefficient seen in the linear range of Figure 18 and the apparent addition of material in Figure 17 is due to a geometry error and not erosion (33). Without this error, the difference in C_l prior to stall between the damaged and baseline case would be negligible, and the change in C_{lmax} would also be less.

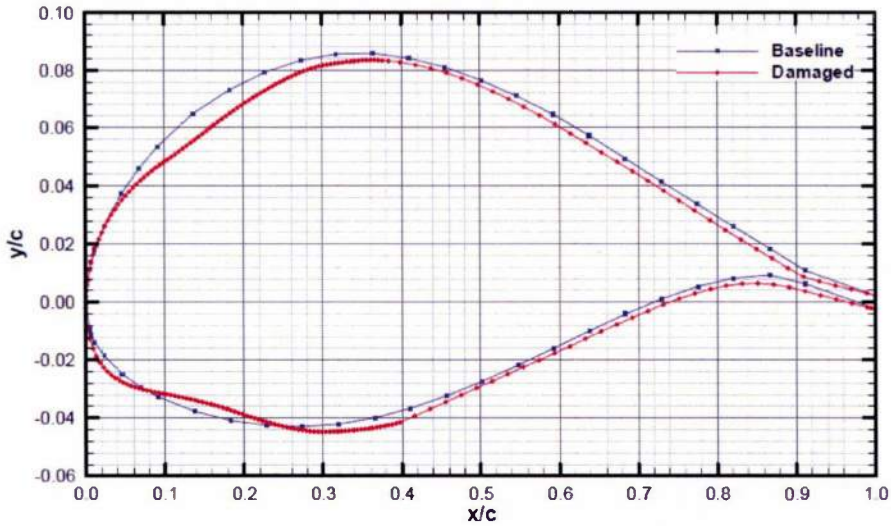

Figure 17: Comparison of baseline contour to eroded contour (33)

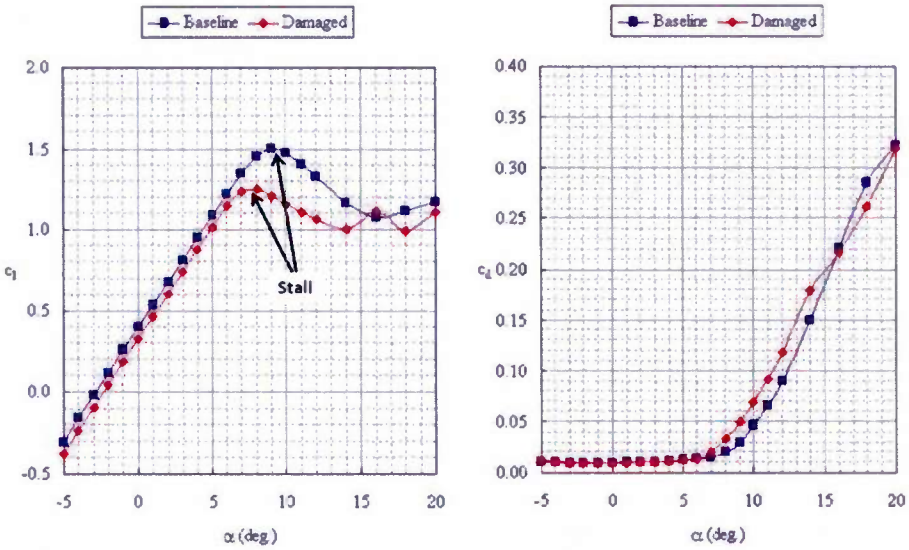

Figure 18: Degradation in lift and drag coefficients due to erosion (Mach 0.5) (33)

1.2.2. Erosion Mechanisms

The rate at which material is removed by sand, dirt, debris, or water is defined as the material erosion rate. Erosion rate is expressed by the ratio of the mass of the material removed to the mass of impinging material (34). There are three significant factors that contribute to how a material will erode:

particle impinging characteristics, particle properties, and surface material properties. The impinging characteristics are controlled by the particle speed, impinging angle, and particle concentration. The impinging particle properties of interest are geometry, density, and size. The material properties of the target material affecting erosion are: Young's modulus, Poisson ratio, hardness, toughness, hardening behavior and microstructure. Studies have shown that the particulate impact angle has a significant affect on the rate of erosion. As seen in Figure 19, ductile materials (metals) have a maximum erosion rate around 20° impingement angle, and brittle materials (ceramics) have a maximum erosion rate at 90° impingement angle (35). The two primary erosion modes (brittle and ductile) will be reviewed in the next section.

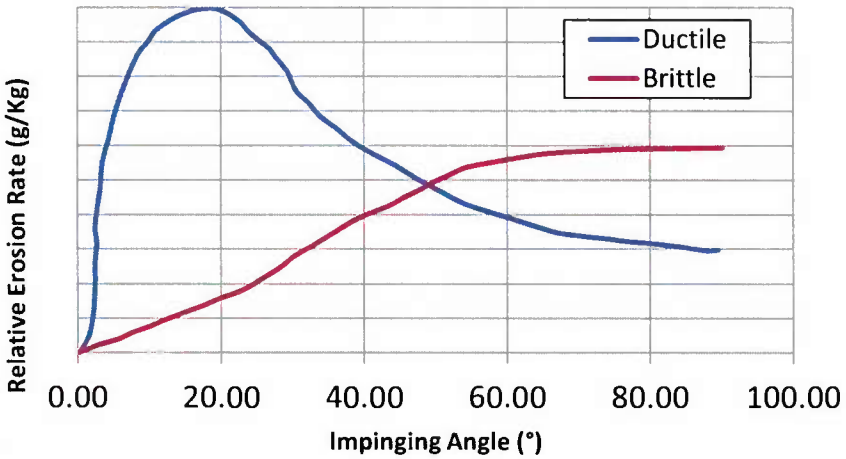

Figure 19: Relative erosion rates for the brittle and ductile modes (34)

1.2.2.1. Brittle Erosion

During the brittle erosion process, material is removed by intersecting cracks caused by the impacting particle. When the particle hits the surface of the target material, both radial and lateral cracks are formed, as seen in Figure 20. However, the coalescence of lateral cracks are primarily responsible for removing material. In Figure 20 (b), h is the depth of the crack, C is the lateral distance of the crack, and a is the distance from the center of the impacting particle the crack starts (35).

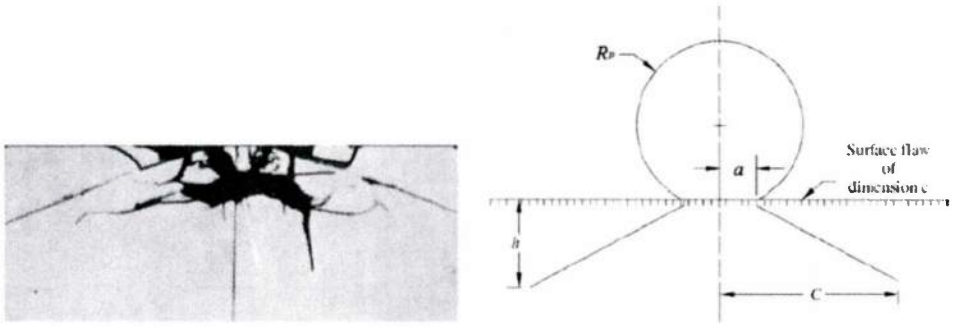

(a) Crater shape (b) Crack propagation

Figure 20: Crack geometries associated with brittle erosion (35)

The maximum load a particle can impart on to the target material and the critical load for crack propagation in the target material are needed to determine the critical impact speed of a particle that would result in erosion. The maximum impact load from a particle, is calculated from Hertzian theory for determining the pressure distribution between a particle and the target material. Hertzian theory only accounts for perpendicular particle impacts. As seen in (1, the maximum load an impacting particle can impart to the target is strongly driven by the speed and size of the particle. The next most important factors are the material properties of the particle and target seen in (1 and (2 (35).

$$F_{max} = \left[\left(\frac{125\pi^3}{48}\right)^{\frac{1}{5}}\left(\frac{E_t}{k}\right)^{\frac{2}{5}}\rho_P^{\frac{3}{5}}R_P^2\right]\omega_P^{\frac{6}{5}} \quad (1)$$

$$k = \frac{9}{16}\left[\left(1-\nu_t^2\right)+\left(1-\nu_p^2\right)\frac{E_t}{E_p}\right] \quad (2)$$

F_{max} – maximum impact load from particle

k –constant

E_t – target Young's Modulus

E_p – particle Young's Modulus

v_t – target Poisson's ratio

v_p – particle Poisson's ratio

ρ_p – particle density

R_p – particle radius

ω_p – particle velocity

Next, the critical crack growth load F_c is calculated from Auerbach's law. F_c is calculated using (3 with φ being an experimentally determined dimensionless material constant. When (1 and (3 are equated, an expression for the critical impact particle velocity can by determined, see (4. Below this velocity, no cracks will be created upon the particle impacting the target material and erosion will not occur (35).

$$F_C = K_{C,t}^2 \frac{k}{E_t} \varphi R_p \tag{3}$$

$$\omega_{pC} = \left(\frac{48}{125}\pi^3\right)^{\frac{1}{6}} \left(\frac{k}{E_t}\right)^{\frac{7}{6}} \frac{K_{C,t}^{\frac{7}{6}}}{\rho_p^{\frac{1}{2}}} R_p^{\frac{5}{6}} \varphi_p^{\frac{5}{6}} \tag{4}$$

F_c – critical crack growth load

$K_{C,t}$ – target toughness

ω_{pC} – critical crack growth particle velocity

φ - experimentally determined dimensionless material constant

The depth and size of the crack is calculated from Roesler's equation, (5, and Evan's relation, (6. Finally, the volume of material that is removed can be estimated to be the volume of a cylinder of material $V = \pi C^2 h$. After substituting for crack length and depth the estimated volume of material removed is calculated by (7 from the Evan's model (35).

$$C^{\frac{3}{2}} = \frac{F_c}{\beta_R K_{C,t}} \tag{5}$$

$$\left(\frac{h}{R_p}\right)^2 \propto \omega_p \sqrt{\frac{\rho_p}{H_t}} \tag{6}$$

$$V \propto \omega_p^{\frac{19}{6}} R_p^{\frac{11}{3}} \rho_p^{\frac{19}{12}} K_{C,t}^{\frac{-4}{3}} H_t^{\frac{-1}{4}} \tag{7}$$

C – lateral crack distance

β_R – empirical dimensionless constant

h – crack depth

H_t – target hardness

V – volume of removed material

1.2.2.2. Ductile Erosion

The second mode of erosion is ductile erosion. As previously stated, ductile erosion occurs at lower angles of particle impact for metallic materials. When the particle hits the target material, the particle scoops out material leaving a small crater and a rim of the displaced material, see Figure 21. Material is removed due to the combined effects of material plastic deformation and the cutting wear from

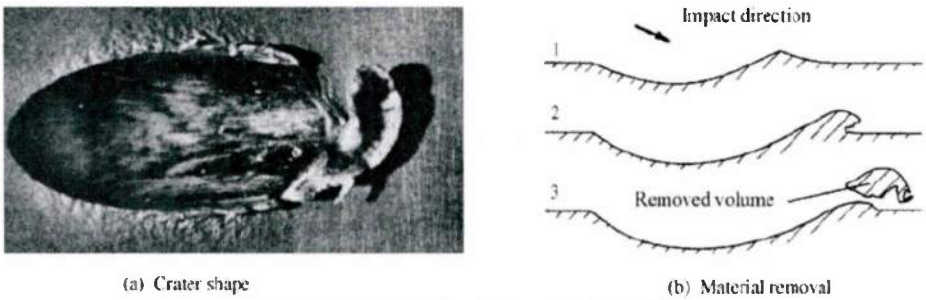

Figure 21: Ductile erosion process (35)

the particle. The first particle scoops out material from the target surface leaving a divot and spur. A subsequent impacting particle will remove the spur (35). The volume of material removed due to plastic deformation (V_D) is derived from Hertzian theory, see (8 and (9.

$$V_D = \frac{\frac{1}{2}M_p(\omega_p \sin\alpha - \omega_{p,el})^2}{\Omega} \tag{8}$$

$$\omega_{p,el} = \frac{\pi^2}{2\sqrt{10}}\sigma_{y,t}^{\frac{5}{2}}\left(\frac{1}{\rho_p}\right)^{\frac{1}{2}}\left(\frac{1-\nu_t^2}{E_t}+\frac{1-\nu_p^2}{E_p}\right)^2 \tag{9}$$

V_D – volume of material removed from plastic deformation

Ω - energy needed to remove the unit volume material from the body due to plastic deformation

ω_p – particle velocity

$\omega_{p,el}$ - maximum particle velocity at which the impact is purely elastic

M_p – particle mass

$\sigma_{y,t}$ – target yield stress

α – impact angle

The amount of material removed due to cutting wear of the particle depends on the component of the velocity parallel to the surface of the target. If the particle leaves the target surface after the impact with a velocity component parallel to the target surface, the volume of material removed can be calculated using (10 and (11, where μ is the energy needed to remove the unit volume due to cutting wear (35).

$$V_C = \frac{2M_p c(\omega_p \sin\alpha - \omega_{p,el})^2}{\sqrt{\omega_p \sin\alpha}}\left(\omega_p \cos\alpha - \frac{(\omega_p \sin\alpha - \omega_{p,el})^2}{\sqrt{\omega_p \sin\alpha}}\mu\right) \tag{10}$$

$$c = \left(\frac{0.288}{\sigma_{y,t}}\right)\left(\frac{\rho_p}{\sigma_{y,t}}\right)^{\frac{1}{4}} \tag{11}$$

If the particle has zero parallel velocity after the impact, the volume of the material removed can be calculated using (**12** and (**13** (35).

$$V_C = \frac{\frac{1}{2}M_p\left[\omega_p^2(\cos\alpha)^2 - k_1(\omega_p \sin\alpha - \omega_{p,el})^{\frac{3}{2}}\right]}{\mu} \tag{12}$$

$$k_1 = 0.082\sigma_{y,t}\left(\frac{\sigma_{y,t}}{\rho_p}\right)^{\frac{1}{4}}\left(\frac{1-\nu_t^2}{E_t} + \frac{1-\nu_p^2}{E_p}\right)^2 \tag{13}$$

Unlike the brittle erosion process, the theories used to determine the volume of material removed due to the ductile erosion process takes into account the angle of impact.

1.2.3. Erosion Resistant Materials

The protective leading edge erosion cap for helicopter blades is currently made from Ti-6Al-4V, stainless steel, and electroformed nickel (16). The US Army is working with Sikorsky Aircraft to design a

novel bi-material leading edge erosion cap. Tungsten carbide cobalt (WC-Co) was allied to the front of the leading edge to protect against direct impingement, and niobium was applied aft of the WC-Co to improve the base alloy erosion resistance, see Figure 22. The WC-Co was applied using a thermal spay process. During the thermal spray process, fuel and air are injected into a combustion chamber where they are continuously ignited. The coating material, in a powder form, is fed into the hot gas stream where it melts and is accelerated before impacting the substrate surface. The niobium was applied with a cold spray process. In the cold spray process, the coating powder material is injected into a stream of heated gas (nitrogen or helium) and is accelerated to supersonic speeds through a converging-diverging nozzle. When the powder impacts the target, the particles plastically deform and adhere to the target surface without melting. The bi-material erosion coating system has been scaled up to cover full UH-60 Blackhawk main rotor blades with a thermal management system so the blade is not damaged during the thermal coating process (36).

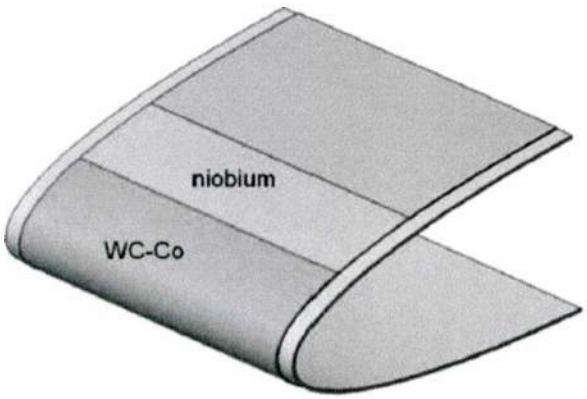

Figure 22: Novel bi-material erosion resistant system (36)

The current coating used on rotorcraft including the UH-60, is a sprayable polyurethane multilayer composite from Hontek that protects against rain and sand erosion (37). No matter how good an erosion coating is, the coating will eventually get damaged. Many systems like the bi-material above cannot be field repaired, and removing the blades and refurbishing then is costly. A big benefit to the Hontek system is the ease of in-the-field repairs. A batch can be prepared and sprayed on the blades

without removing the blades from the helicopter. This repair process decreases helicopter down time and reduces repair cost (37).

1.3. Objective

The objective of this research was to develop a novel helicopter leading edge cap to work in ice and sand erosion environments. A system formed by an ultrasonic ice protection system and an erosion resistant coating was explored. The ice adhesion strength of the proposed coatings were evaluated. The capability of the new erosion resistant coating to be used with ice protection systems was experimentally explored with the implementation of an ultrasonic de-icing prototype over a range of icing regimes. The de-icing performance of the coating/ultrasonic de-icing prototype was compared to that provided by electro-thermal de-icing.

To achieve these objectives, the goals of the present work are to:

- Evaluate the feasibility of leading edge cap structural tailoring via stress concentration discontinuities for ultrasonic de-icing performance.
- Through experimentation, determine what factors affect impact ice adhesion strength to metallic structures.
- Evaluate the ice adhesion strength of erosion resistant materials over a range of surface roughness values and ambient temperatures.
- Compare ultrasonic and electro-thermal de-icing system performance with a novel erosion coating.

1.4. Thesis overview

1.4.1. Chapter 2: Feasibility Study of Tailored Stress Concentrators

Previous research has shown that periodically removing material from the leading edge of a ultrasonic de-icing system to create stress concentrations can locally increase ice interfacial transverse

shear stress. The current research evaluates the effectiveness of location-tailored additive stress concentrations in increasing average interfacial transverse shear stress and decreasing the power required to de-ice.

1.4.2. Chapter 3: Evaluation of Ice Adhesion Strength on Erosion Resistant Materials

To properly model mechanical de-icing systems, the ice adhesion strength of the surface must be known. Chapter 3 discuses a variety of environmental and surface characteristics tested to determine what properties most effect ice adhesion strength. In addition, new titanium nitride based erosion resistant coatings were developed for helicopter leading edges and tested for ice adhesion strength and compared to typical uncoated metallic erosion resistant materials.

1.4.3. Chapter 4: Ultrasonic and Electrothermal Rotor Ice Testing of an Erosion Resistant Coating

Ultrasonic and electrothermal ice protection systems were tested and compared with a novel erosion resistant leading edge coating. The power required to de-ice at two different icing condition was determined for both systems.

1.4.4. Chapter 5: Conclusions and Recommendations

The final chapter summarizes the conclusions drawn from this research and makes recommendations for future research areas to increase the effectiveness and robustness of ultrasonic de-icing systems with erosion resistant leading edge coating.

2. Feasibility Study of Tailored Stress Concentrators

2.1. Motivation & Objective

To increase the performance of ultrasonic piezoelectric de-icing systems for rotorcraft, researchers have proposed to tailor the leading edge cap by implementing geometric discontinuities, and thus creating stress concentrations. "Tailored" in this text means the location of the discontinuities are placed strategically in regions of low interfacial transverse shear stress. In previous work done by Zhu,

the discontinuities were created by removing material periodically (not tailored) from the inside of the leading edge erosion cap, called Tailored Wave Guides (TWGs) (see Figure 23) (38).

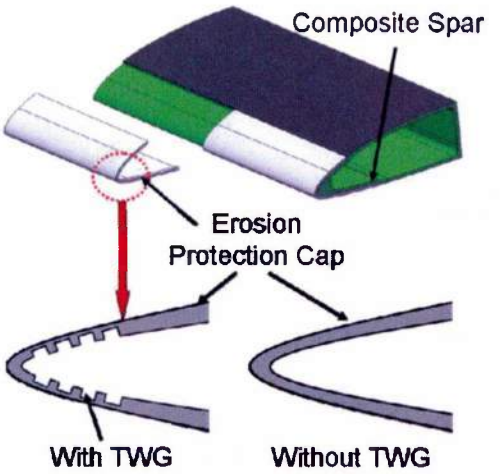

Figure 23: TWG Leading Edge (38)

Zhu's model showed an increase in ice interfacial transverse shear stress of 300% at one point on a flat square plate. Also experimental results showed a 75% reduction in power to de-ice a square bench top aluminum plate (38). The results Zhu acquired were intriguing but come with some concerns. First, removing material raises concerns about structural integrity and erosion resistance. More importantly is the low fidelity of the finite element model used in her analysis. Zhu only used one linear element though the thickness of the actuator and two linear elements though the thickness of the plate and ice. This is not a high enough grid resolution to converge. Also, her frequency step size was too big. Zhu used a frequency step size of 500 Hz and the step sized used for this research was 50 Hz a factor of 10 greater resolution. Another issue is how the stress was calculated. The largest error made, unknown at the time, was in the calculation of the stress and impedance. The system is dynamic, so both the real and imaginary parts of the output must be resolved into magnitude and phase. Zhu ignored the complex response and compared the real stress value at phase 0 in the harmonic motion. Comparing the stress at only one location and one time does not give a clear picture of overall effectiveness. Average magnitude of the interfacial shear stress over the whole surface is the most representative metric. Damping is also a very

difficult phenomenon to capture properly in finite element analysis. Since the Zhu did not publish any information on what damping properties were used, it is assumed that no damping was used and the stress values published are over estimated. It is also unclear how Zhu collected the experimental data. When dynamic electric systems are driven, some of the power is reflected back to the amplifier due to the mismatch in impedance between the amplifier and load. The power used for work is the difference in the forward and reverse power at the amplifier. Zhu was not explicit on which power was recorded (38).

This chapter covers new research in the field of tailored structures for ultrasonic de-icing performance. The new stress concentrators, Tailored Stress Concentrators (TSCs), add material to the inside of the leading edge in regions of inherently low transverse shear stress to increase the stress where ice would not normally de-bond at a nominal input power to the ultrasonic actuators (Figure 24). The goal of this research is to decrease the power required to de-ice a structure.

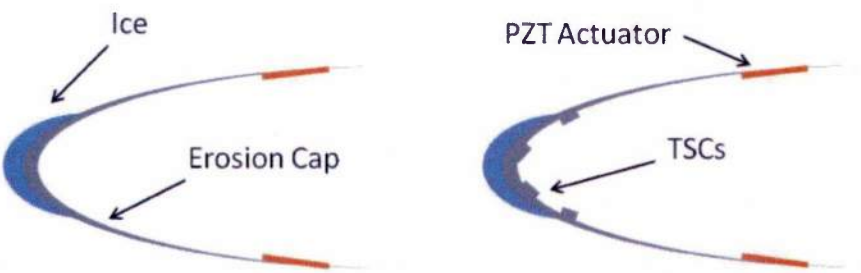

Figure 24: TSCs Leading Edge

2.2. Physical System

Before experimental rotor testing of the TSCs was performed, bench top experiments were performed to validate finite element models and prove that the TSC concept is a viable system for amplifying ultrasonic transverse shear stress at the ice interface. The actuators used for the bench top testing were piezoelectric disks made from PZT-4 (see Figure 25). The disks were 3.0 inches in diameter and 0.05 inches thick. The PZT was poled though the thickness of the disk. A biased AC potential was applied to the top and bottom surface of the disk. The motion of the actuator is dependent on the frequency of the applied electrical load. For this research, the first radial mode was driven, and the

frequency of the first radial mode of a free 3.0 inch diameter PZT-4 disk was 28.3 kHz. Due to the addition of the DC offset to the driving electricity, the actuator will only compress, instead of expanding and compressing which increases durability.

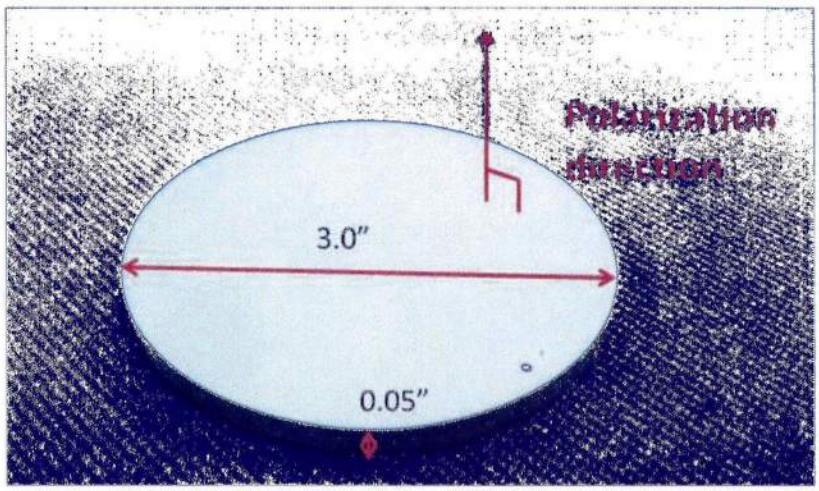

Figure 25: 3.0 inch diameter PZT-4 actuating disk

The actuator was fabricated using a composite manufacturing technique with a three-cure process. The first cure cycle sandwiched the actuator and bottom electrode between two layers of FM-73 film adhesive. The top layer of FM-73 acts as an insulator between the two electrodes, but leaves an opening in the middle of the actuator for the top electrode to make contact. Cure two adds the top electrode and one more layer of FM-73 to create an actuator packet. The last cure bonds the packet to the host structure, as seen in Figure 26.

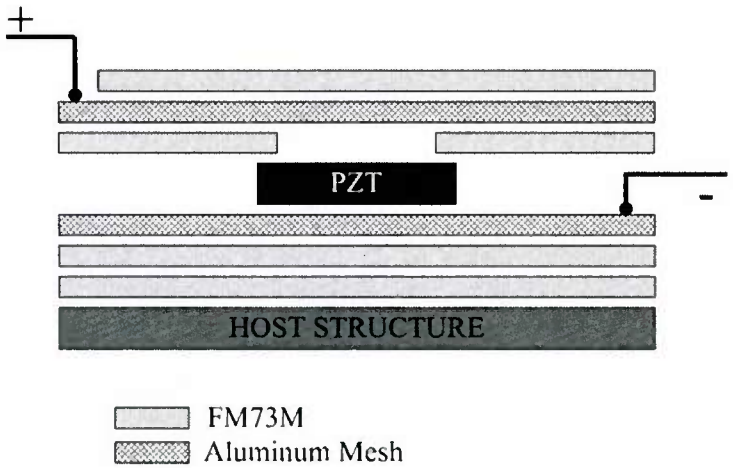

Figure 26: Layup design for actuator bonding (39)

The cure cycle starts with a ten minute ramp up from average room temperature (roughly 73°F) to 135°F, and then holding at 135°F for 20 minutes. This first hold allows the FM-73 to flow into the aluminum mesh electrode. A second 20-minute ramp increases the temperature to 250°F and then holds for 60 minutes. This longer hold cures the FM-73 resin (see Figure 27).

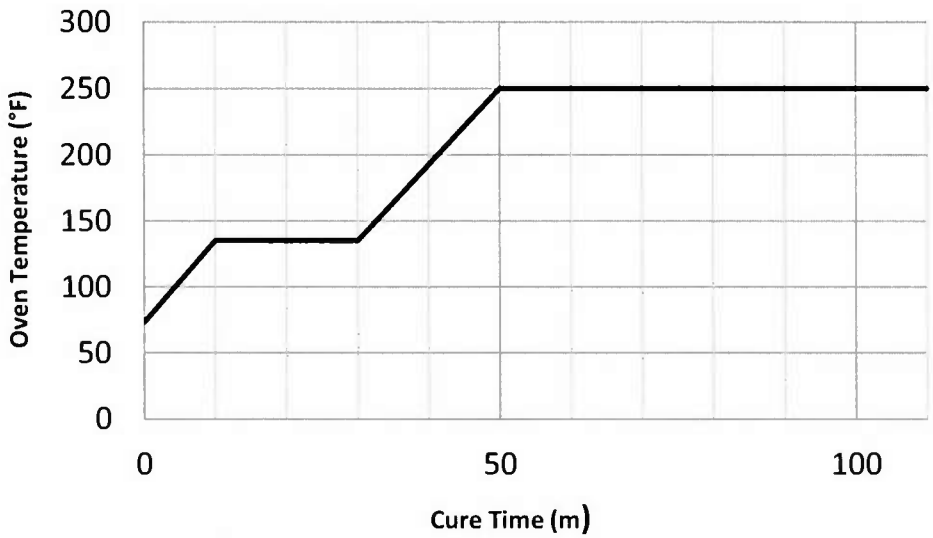

Figure 27: Curing cycle for actuator composite manufacturing

The final product is a 13 inch diameter aluminum plate with the actuator disk cured to the middle of the plate (see Figure 28). The differentiation between the ground and positive sides of the actuator is imperative to driving the actuator in compression only and not extension only.

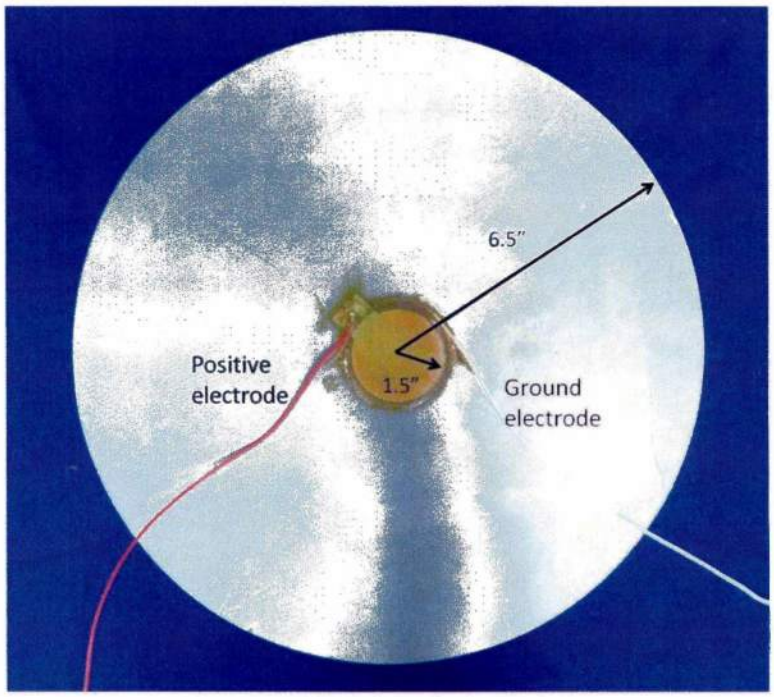

Figure 28: Final product after 3 cure cycles

When the actuator was bonded to the plate, the resonant frequency of the system changed compared to the resonance of the free disk. A driving system designed by Overmeyer (which will be discussed in more detail later in this section) determined the resonant frequency by analyzing the electro-mechanical impedance of the composite system (39). The magnitude of the impedance was measured in ohms and can be thought of as the electro-mechanical resistance of the system. A system resonance occurs at a minimum in the impedance magnitude. An example of an impedance curve can be seen in Figure 29. The details of the data presented in Figure 29 will be presented in a later section.

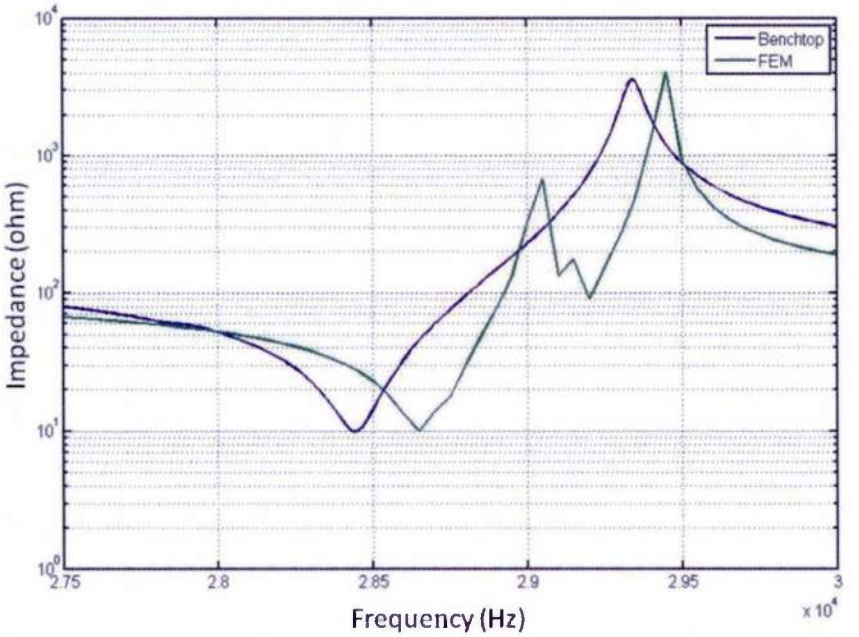

Figure 29: Typical impedance curve for a 3.0 inch diameter actuator on a 13.0 inch diameter aluminum plate

2.3. Finite Element Analysis (FEA)

A commercial finite element software, Abaqus, was used to determine the effectiveness of TSCs on simplified structures. Due to the mesh density required to capture the proper stress distribution in the ultrasonic range, axisymmetric models were used to minimize the computational resources required for analysis. The system the FEA modeled was comprised of a 3.0 inch diameter 0.05 inch thick PZT-4 disk bonded to a 13.0 inch diameter 0.04 inch thick Al-6061 plate with a 0.02 inch thick bondline. The Al-6061 TSCs were modeled as perfectly bonded to the plate. The thickness of the TSCs was 0.04 inches and the width was 0.04 inches. The perfectly bonded ice covered the entire bottom surface and was 0.04 inches thick. See Figure 30 for model layout and dimensions (note TSC locations are generic). Previous work has shown that two quadratic elements though the thickness with a width of 2mm is sufficient to model a plate with an actuator (39). To accurately capture the affects of the TSCs on the ice interface transverse shear stress, each part (actuator, bondline, plate, TSCs, and ice) had ten quadratic elements

though the thickness and the element length is 0.5mm. To expedite the calculations, the analysis was run in parallel over eight processors.

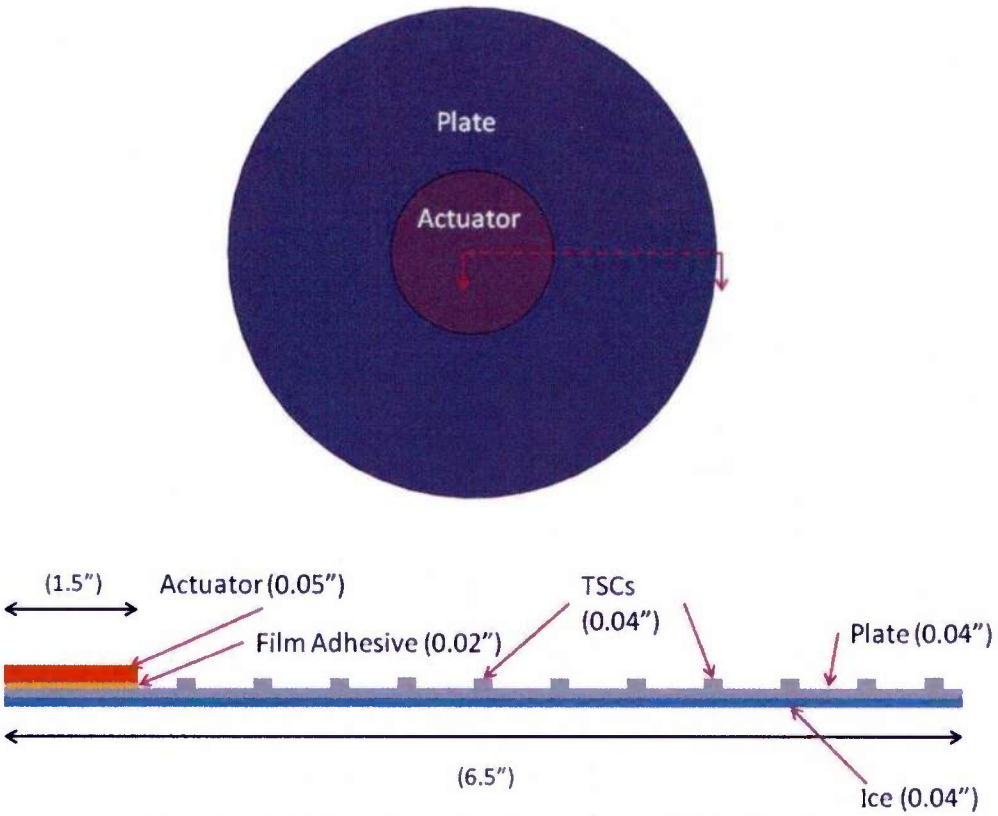

Figure 30: Finite element model schematic for prototype analysis

The material used for the piezoelectric actuator was lead zirconate titanate based PZT-4. PZT-4 is used for high-power actuators because it has a high resistance to depolarization and low dielectric losses under high electric potential. The film adhesive FM-73 was used to bond the actuator to the plate. One major assumption in the finite element model is that the ice was treated as both isotropic and homogenous. This assumption will be discussed in more detail later in this chapter. The material properties for all of the components can be found in Table 1.

Table 1: Material Properties

	Density (kg/m^3)	Young's Modulus (GPa)	Poisson's Ratio	Beta Damping
Al-6061	2700	69	0.33	1.06E-08
FM-73	1100	25	0.4	1.00E-07
Ice	1000	9.5	0.28	1.06E-08

PZT-4

Density (kg/m^3)	Beta Damping
7600	1.12E-08

Dielectric

1.31E-08	0	0
0	1.15E-08	0
0	0	1.31E-08

Elastic (Pa)

1.39E+11	7.43E+10	7.78E+10	0	0	0
7.43E+10	1.15E+11	7.43E+10	0	0	0
7.78E+10	7.43E+10	1.39E+11	0	0	0
0	0	0	2.46E+10	0	0
0	0	0	0	3.06E+10	0
0	0	0	0	0	2.56E+10

Piezoelectric (C/N)

0	0	0	0	0	4.96E-10
-1.23E-10	2.89E-10	-1.23E-10	0	0	0
0	0	0	0	4.96E-10	0

In practice, ultrasonic systems were run at a specific resonance to maximize the input power. To find the resonance of a system, the model was analyzed in steady state at frequencies around the first radial resonant frequency of the actuator. The electrical charge across the actuator and frequency from each frequency step was output from the FEA to determine system impedance (Equation 14, Equation 15).

$$Z = \frac{V}{I} = \frac{V}{2\pi f q} \qquad \text{Equation } \mathbf{14}$$

$$q = q_{mag} e^{iq_{phase}} \qquad \text{Equation } \mathbf{15}$$

Z - complex impedance

I - current

V –voltage

f – driving frequency

q – complex charge

Two FEA studies were performed and are presented. First, a proof-of-concept analysis was studied to determine the proper location for the discontinuities. Second, a finite element model of a bench top experiment was analyzed for model validation and to evaluate the effectiveness of the TSCs under real conditions.

2.3.1. Proof-of-concept Analysis

Four FEA models were used in the proof-of-concept analysis, all similar to the configuration shown in Figure 30. Model A was a plate with no discontinuities, used for determining the regions of low transverse shear stress and was the baseline for comparison. The B model was the best case scenario with eleven properly spaced discontinuities in regions of naturally low stress (i.e. TSCs). The C model had the proper number of discontinuities that were evenly spaced; this accounts for potential manufacturing variation. The D case was the worst-case scenario, in which twelve discontinuities were placed in regions of high shear stress. The four different proof-of-concept finite element models can be seen in Figure 31. The only load on the system is a voltage potential across the actuator and there were no geometric boundary conditions applied to the models (i.e. free-free system).

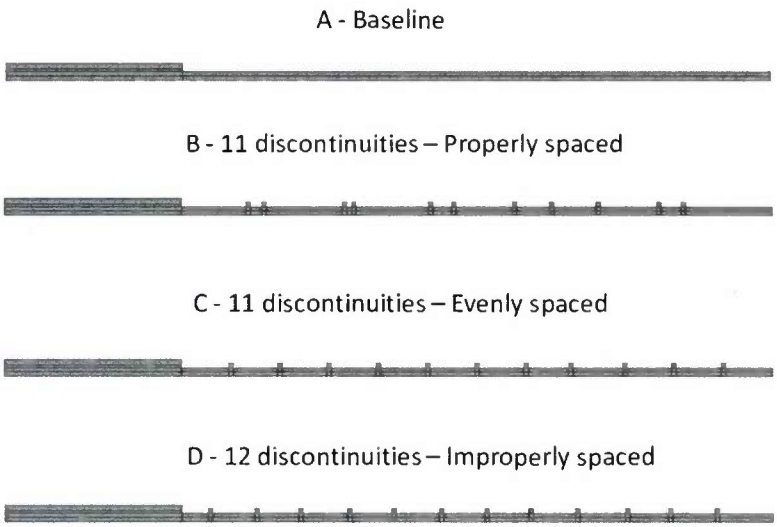

Figure 31: Proof-of-concept models

As expected, the impedance minimums occurred a few kHz below the first resonant frequency of the actuator (28.3 kHz) (see Figure 32). For the impedance minimums and associated frequencies for each model, see Table 2.

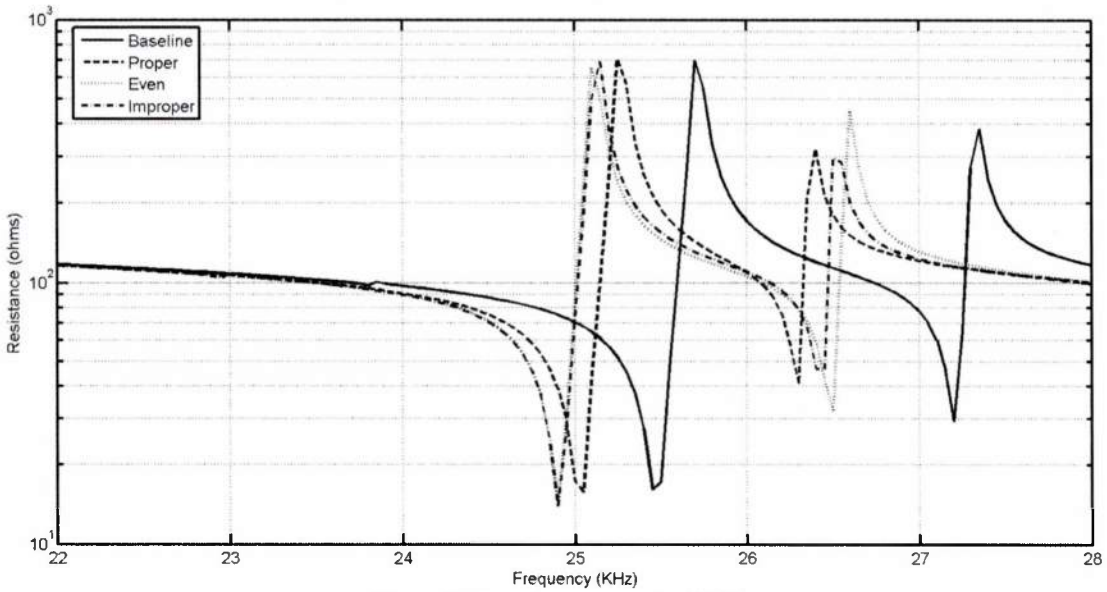

Figure 32: Impedance curves for FEM

Model	Impedance Min (ohm)	Frequency (kHz)
A - Baseline	16.12	25.45
B - Proper Placement	15.76	25.05
C - Evenly Spaced	14.29	24.9
D - Improper Placement	13.86	24.9

Table 2: Impedance minimums & associated frequencies for FEMs

For the following analysis, 100 watts of power was applied to the actuator, and the magnitude of the ice interfacial transverse shear stress was examined. For model B when the discontinuities were properly tailored, the TSCs have two effects. As intended, the stress in regions of naturally low stress increased, due to the stress concentration caused by the geometric discontinuity of the TSCs. In addition, the stress of each local maximum increased (Figure 33). These two effects give an overall ice interfacial shear stress increase of 20% for TSCs above the baseline (Figure 36).

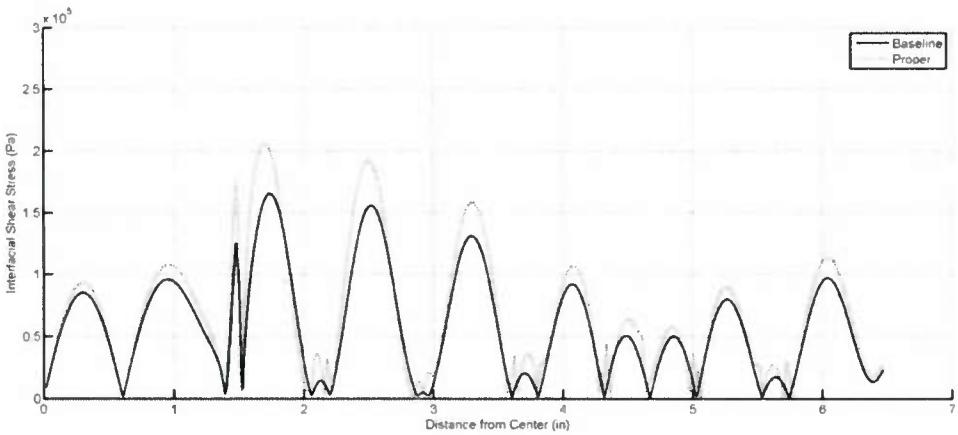

Figure 33: Stress comparison for model B - properly spaced discontinuities

In the case where the proper numbers of discontinuities are evenly distributed (model C), similar effects are seen (Figure 34). However, stress concentrations did not necessarily fall in the regions with naturally low stress. Some fell on local stress maximums and others fell between local stress minimums and maximums. The evenly spaced TSC case had an overall interfacial shear stress increase of 19% above the baseline (Figure 36).

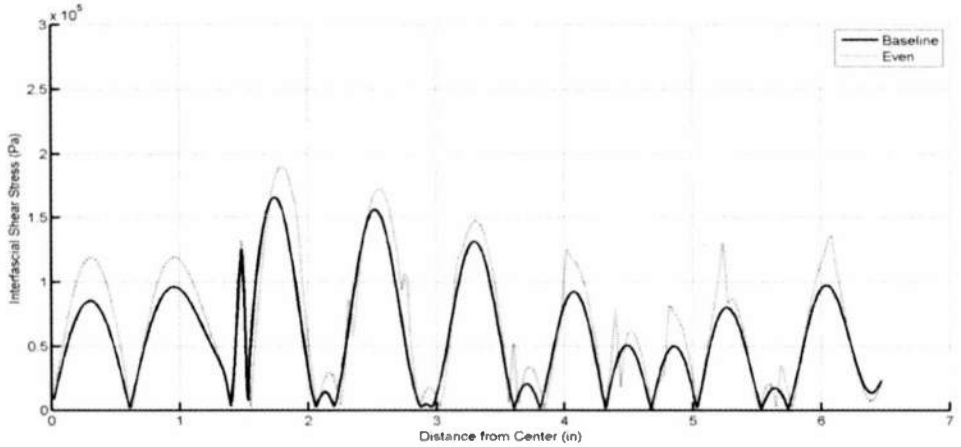

Figure 34: Stress comparison for model C- evenly spaced discontinuities

For the D model where twelve discontinuities were placed at the local maximum, the two effects of stress concentrations and increasing of the local maximum collapse to a single effect. The TSCs created sharp local maximums in regions that already had high shear stress (Figure 35). The benefit of the discontinuities was decreased for this case. The average interfacial shear stress increased by only 8% (Figure 36).

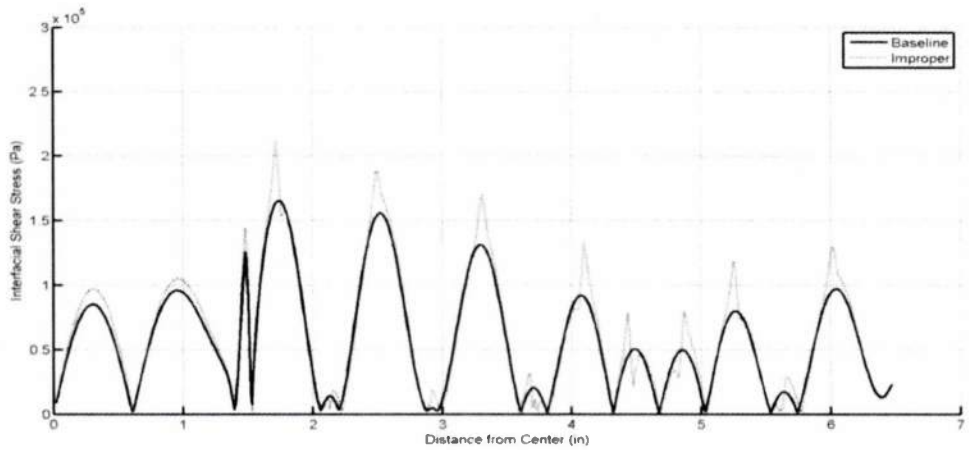

Figure 35: Stress comparison for model D - improperly spaced discontinuities

A summary of the average shear stress of the four finite element models is shown in Figure 36. It can be seen from this study that if geometric discontinuities are properly added to regions with low interfacial shear stress, the TSCs could increase average ice interfacial shear stress by up to 20%. The

proposed system is still reliable even if the manufacturing process of the TSCs is poor. Only 1% of average shear stress is lost due to discontinuity misplacements. If the discontinuities are placed in the completely wrong place (case three) there was some increase in shear stress; however, the average stress increase was less than 10%.

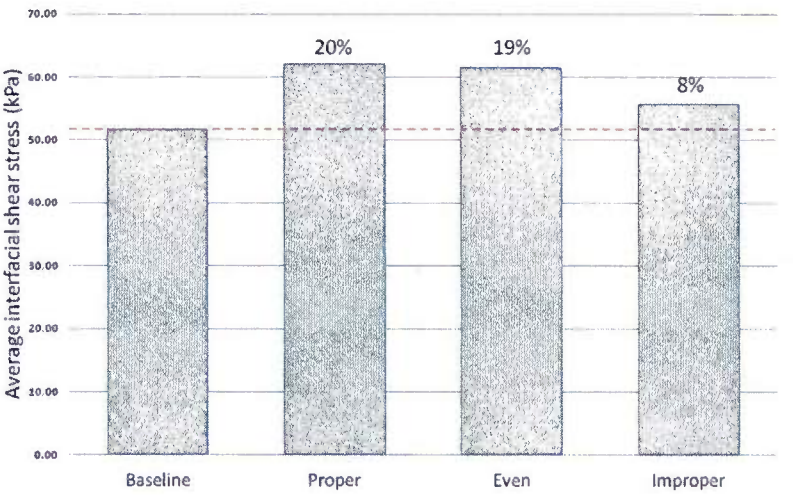

Figure 36: Summary of average interfacial shear stress

2.3.2. Bench Top Analysis

A finite element analysis was run in tandem with bench top experiments to validate the FEA. The system used for this study was simplified from the proof-of-concept model because of complications with freezing water over a large area uniformly. It was extremely difficult to freeze water uniformly over an almost one square foot area without the water running off the edge of the test plate. Water can freeze at different rates, which also creates a variety of ice thicknesses, which can result in the internal stresses cracking the ice before a test can be performed. To avoid these issues, a much smaller annulus of ice was used for bench top testing and FEA. As seen in Figure 37, a one-inch ring of ice was frozen between a radius of 3.5 and 4.5 inches. First, a model without TSCs was analyzed to determine the best locations for applying the TSCs. This model became the baseline and was therefore used for comparison. From the baseline model, one could determine that there were two shear stress minimums, so two TSCs are required.

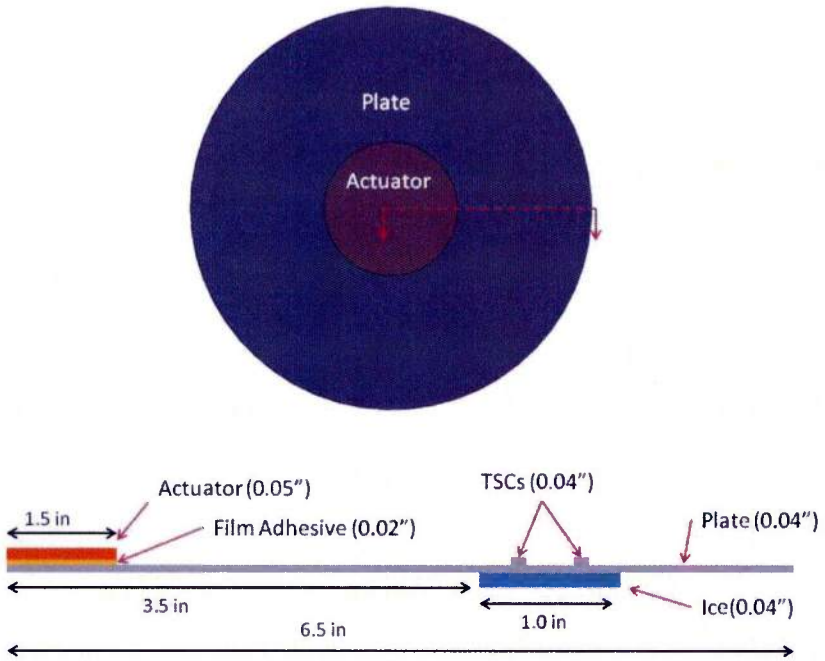

Figure 37: Schematic of bench top system

As seen in Figure 38, the TSCs created a stress concentration, increasing the stress in the normally low stress region; however, the TSCs also decreased the stress over a large part of the center of the ice. This caused a net loss of 9% average shear stress (Figure 39).

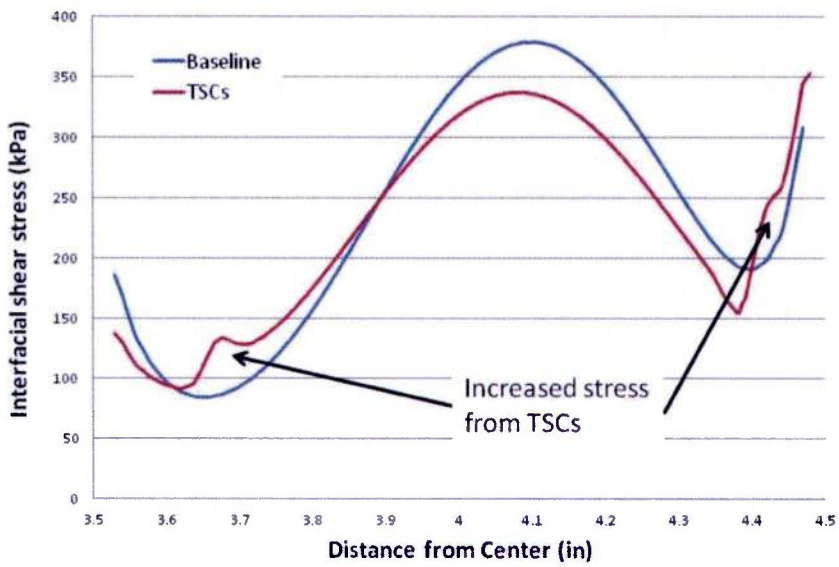

Figure 38: Bench top interfacial shear stress

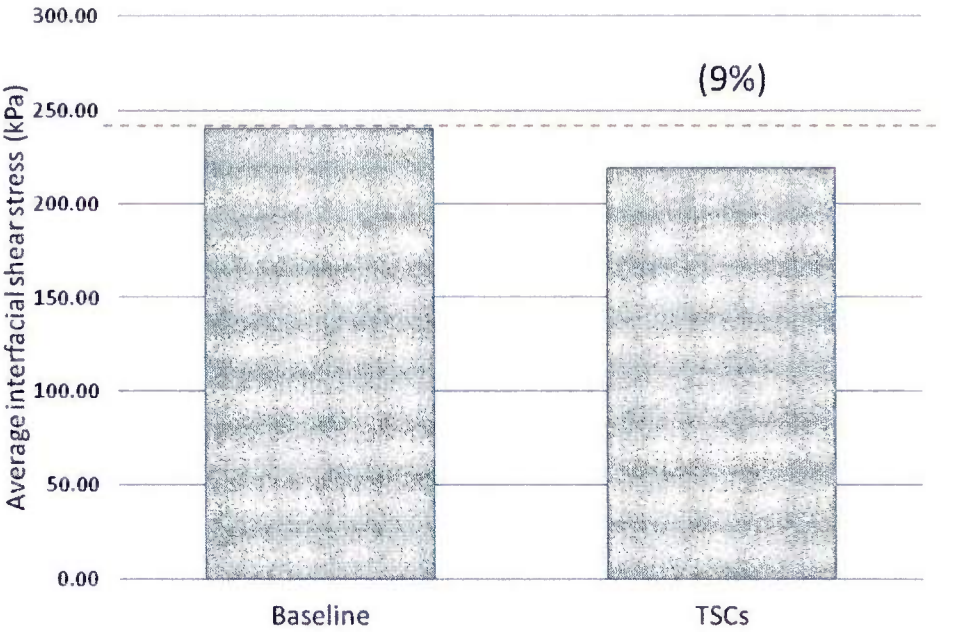

Figure 39: Average interfacial shear stress for bench top FEM

This loss in performance in the bench top system as compared to performance benefit of the TSCs in the proof-of-concept system highlights the system's dependence on TSCs. Just because the TSCs were beneficial for the proof-of-concept models does not guaranty TSCs will be beneficial for all systems. From this analysis, the expectation for the experiment was that TSCs would have little effect or slightly increase the power required to de-ice.

2.4. Bench Top Experiments

Even though the finite element analysis concluded that TSCs should not increase de-icing performance, a bench top test was conducted to verify the results. The tests were performed over a range of powers to determine the relationship between load power and percent area de-iced. Just as in the FEM, a one-inch ring of ice was frozen three and a half inches from center; however, the ring was broken up into smaller patches since controlling the freezing of the complete annulus of water is difficult. A photograph of the segmented annulus is shown in Figure 40. To represent a free boundary condition, the plate was placed on a block of foam with a twelve-inch diameter hole cut out of it. The first series of tests

were run without the TSCs, to obtain baseline experimental results. Then the TSCs were bonded to the plate, and the tests were repeated, and the results were compared.

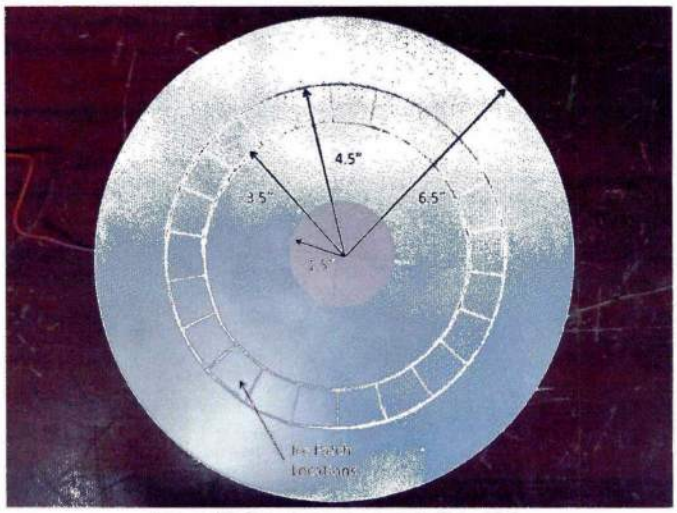

Figure 40:Bench top test plate (ice side)

The TSCs were placed as specified from the FEM and were bonded with the same FM-73 film adhesive and cure cycle as the actuator. The TSCs were bonded to the same plate used for the baseline to keep the system as consistent as possible.

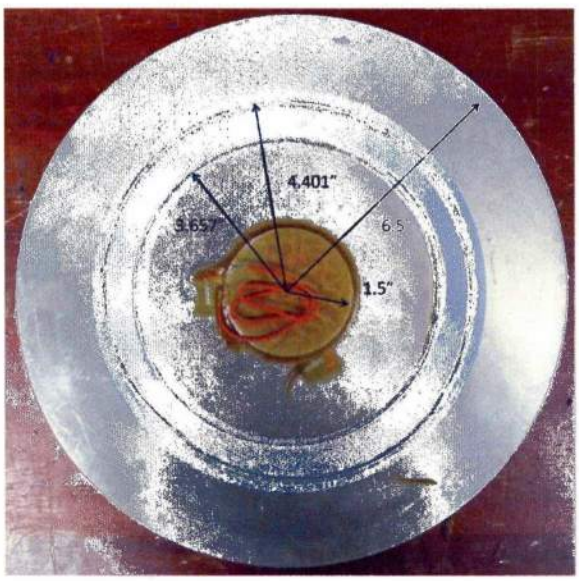

Figure 41: Bench top test plate (actuator side with TSCs)

2.4.1. Driving System

The actuator driving system used in these experiments, developed by Overmeyer, used a LabVIEW virtual instrument to interface with relays, an impedance analyzer, and driving system (see Figure 42) (39). The relays protect the analyzer and computer from high voltage when driving the PZT actuators. Before the program ran, the user input a frequency bandwidth around the resonant frequency for the impedance analyzer to analyze, the run duration, and amplifier gain. Since the resonance frequency of the disc was 28.3 kHz, the bandwidth used for these tests was 27.5 kHz to 30.0 kHz. The run time was set for 3.5 seconds, and the gain was varied for each test. When the relay closes the electrical path between the actuator and the impedance analyzer, and opens the electrical path between the driver and the actuator, the impedance analyzer sweeps over the given bandwidth and determines the impedance of the system. The computer then determines the frequency with minimum impedance, the resonant frequency. The frequency was sent to the signal generator, gain was set on the amplifier, and the resistance for the impedance matching network was selected. Next, the relays switched and the amplifier was turned on. While the actuator is driving, the forward and reverse power from the amplifier is monitored. When the test was completed, the load power was calculated from the difference of forward and reverse power. The average load power was calculated and plotted against percent de-ice.

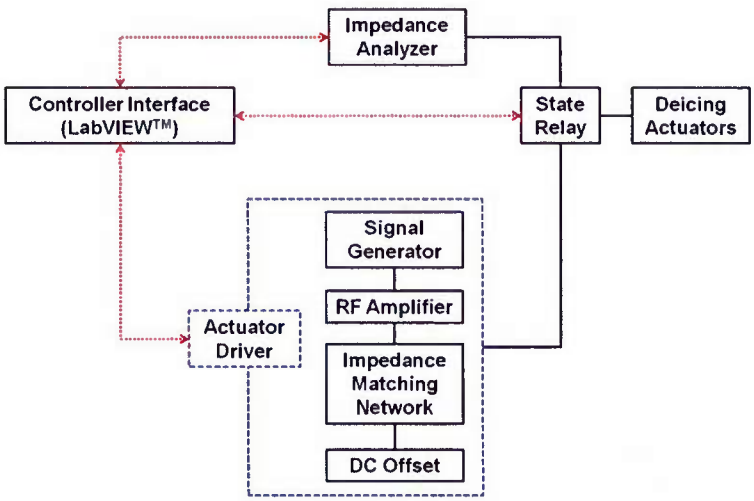

Figure 42: Schematic of actuator driving system (39)

2.4.2. TSC Bench Top Results

The results from the bench top experiments match the conclusion from the FEA. With the high scatter in the data, no difference can be seen between the system with and without the TSCs (see Figure 43). This system of TSCs was very system dependent and not versatile enough for practical applications. The one obstacle for this system was the TSCs are mode-dependent. Given the wide envelope of icing conditions and the fact the ice shape is time dependent, the range of possible ice shapes is almost infinite. At best, the TSCs could be optimized for very thin layers of ice, typical for a wide range of early ice accretion conditions. However, this may not include every condition because of the density differences in the two icing regimes. Another issue would be the complex vibration shapes of a realistic structure. Having a high enough fidelity ice model to properly predict the stress patterns is very difficult on axisymmetric models, much less a full 3D structure.

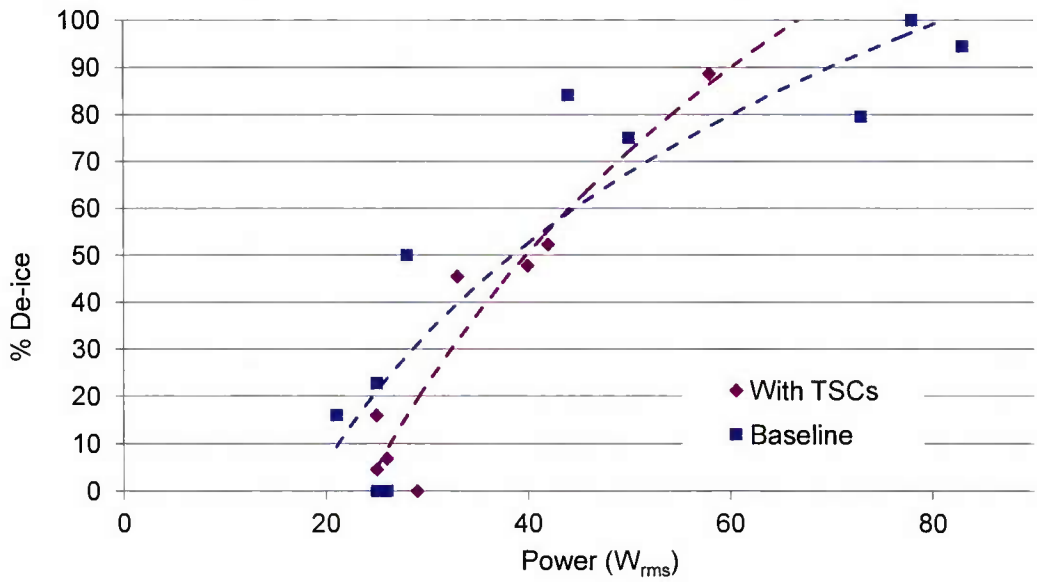

Figure 43:Bench top results

2.5. Model Validation

Model validation is an important step for any analysis technique. Since the ice has the largest unknown variables, the FEMs are validated with and without the ice. The two characteristics correlated between model and experimental results are impedance and out-of-plane velocity. It would be ideal to test and compare interfacial shear stress, but the available techniques would require modifications to the system that would change the results. The size of interfacial transverse shear sensors are on the same order of magnitude at the TSCs. The transverse shear sensor would have to be modeled, and 3D models would be needed because the addition of the sensor would break down the assumption of axisymetricness. The impedance measurement provides information on the electro-mechanical resistance of the system and is primarily an in-plane effect since the actuator was vibrating in-plane at its first radial mode. When there was no ice on the plate, the FEM and bench top models have very similar impedance curves (see Figure 44). When comparing minimum impedances, there was only a 0.4% error in the impedance and a 0.7% error in the frequency.

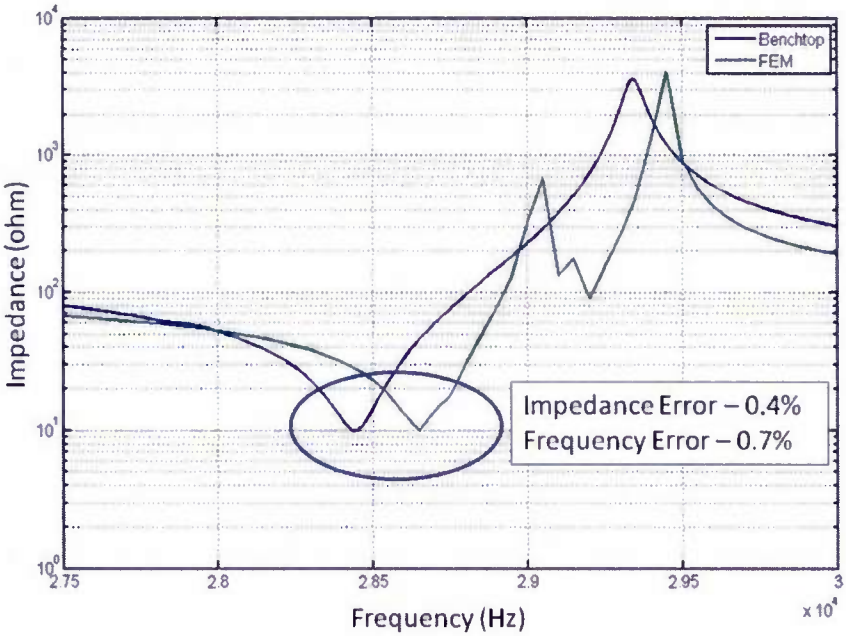

Figure 44: Impedance validation without ice

A laser vibrometer was utilized to determine the out-of-plane velocities created by the ultrasonic mode (see Figure 45). The laser was attached to a motorized linear traverse to scan over the surface of the plate. A linear variable differential transformer (LVDT) is used to determine the position of the laser and allows for autonomous continual scanning of the structure. The laser position was accurate to 0.01 inches and the system could collect data at a rate of approximately 1.5 points per minute. At each point, the laser collected data for 5 seconds. A similar setup and procedure was used by Overmeyer to validate his models (39).

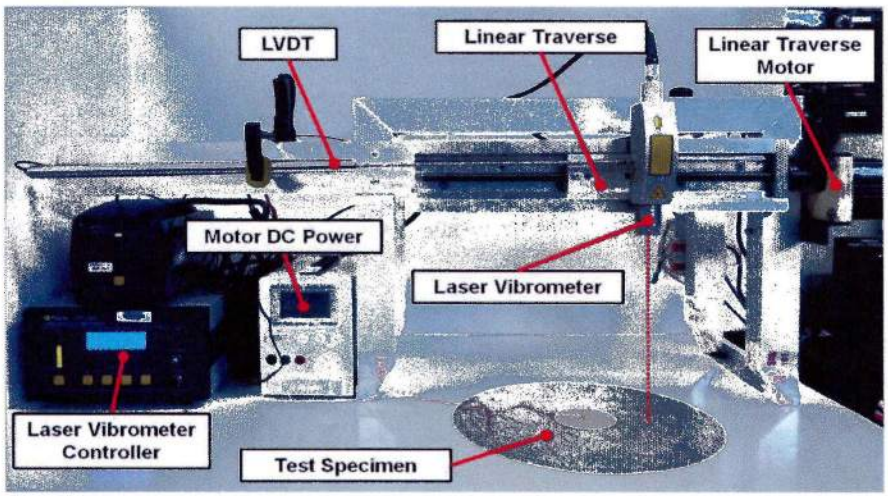

Figure 45: Laser vibrometer setup (39)

The magnitude of the signal is determined then normalized to input voltage. The first three inches from the edge of the plate were scanned with a step size for the laser of 0.05 inches and compared to the FEM. Again, the model matches experimental results, presenting discrepancies of less than 15%. After completing the impedance and out-of-plane velocity comparisons, it can be concluded that the FEM is valid for the plate and actuator system modeling without ice accretion.

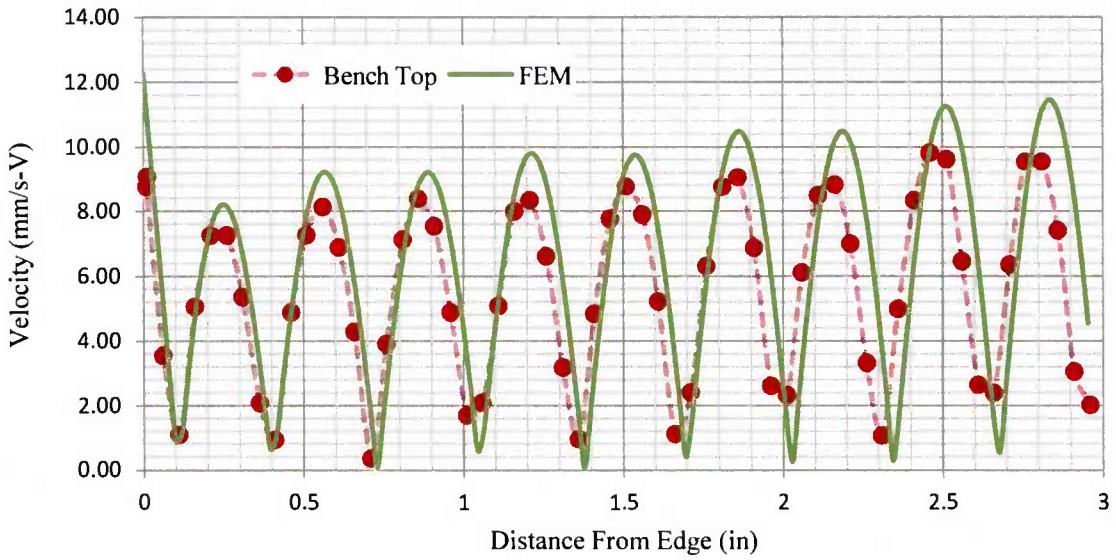

Figure 46: Normalized out of plane velocity magnitude

Next, the FEM predictions were compared with the experimental results obtained with freezer ice accretion. As seen in Figure 47, the impedance curve for the bench top plate with ice was now more complicated as an impedance minimum corresponding to an ultrasonic mode of the structure is harder to identify. There are multiple local minimums and maximums that were not seen in the FEM. Changing the basic material properties of the ice cannot reproduce the complex shape of the actual impedance curve, suggesting inhomogeneous ice properties. The FEA predicts the impedance 34% lower than the experiment and the resonant frequency 1% higher.

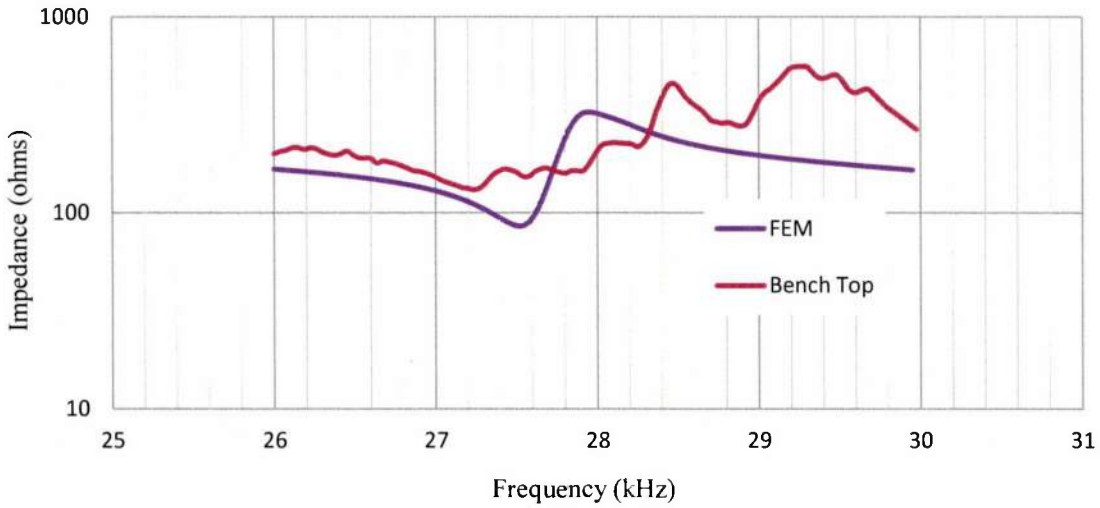

Figure 47: Impedance validation with ice

Finally, the out-of-plane velocity was compared over the ice region. Since the shape of the velocity profile was more important than the absolute magnitude, the velocities are normalized to the maximum value (see Figure 48). The FEA was able to capture the drop in velocity from the inside edge of the ice region to the edge of the plate as well as the general shape of the velocity in regions where there is no ice. However over the ice region, the most important region, the FEA could not predict the proper number of velocity nodes. The FEA predicted two velocity nodes and the experiment has one node. If the FEA was not predicting the proper velocity shape, it is not predicting the interfacial shear stress correctly. This was a major problem because the location of the TSCs for the experiment were based on the stress fields of the FEA. Since the FEA could not predict the correct velocity minimums, the calculated stress minimums are likely incorrect. Therefore the location of the TSCs were incorrect.

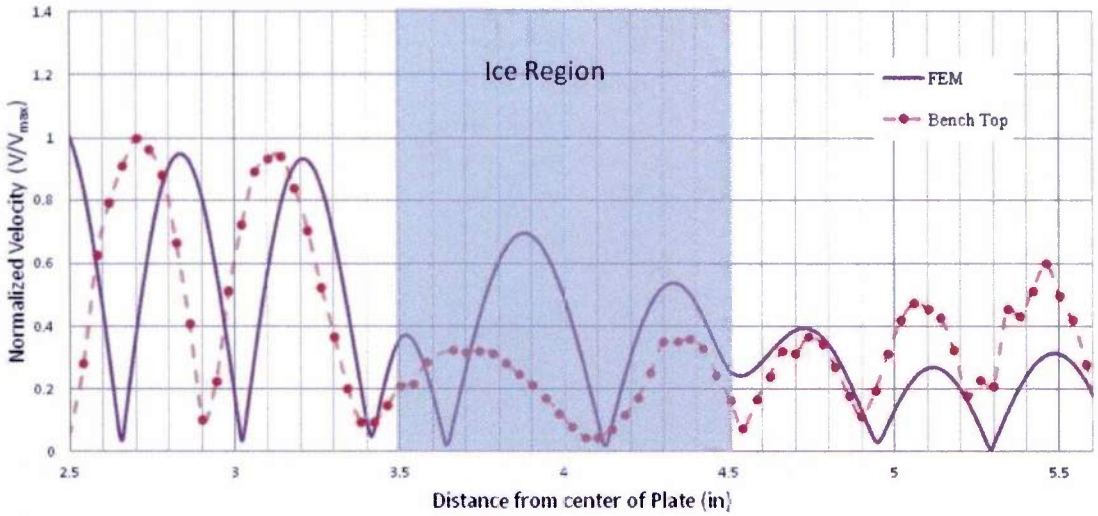

Figure 48: Normalized out of plane velocity with ice

A basic axisymmeteric homogeneous, isotropic model for the iced system does not have a high enough fidelity to match the complexity of real ice. Using bulk material quantities may be sufficient for basic static modeling; however, the assumptions of axisymmeteric, homogeneous, and isotropic material properties may break down at ultrasonic frequencies as inhomogeneous ice is accreted. Since the FEA could not predict the proper location for the TSCs, it was not possible to build an ultrasonic de-icing system with TSCs using the current modeling techniques. It has also been seen that TSCs did not always increase the average ice interfacial transverse shear stress. The TSCs increased the average shear stress by 20% for the proof-of-concept models but decreased the shear stress by 9% for the bench top model.

3. Ice Adhesion Strength of Erosion Resistant Material

3.1. Motivation and Objectives

Recently new erosion resistant coatings for helicopter leading edges have been developed, such as binary and ternary nitride-based systems and WC-Co systems (36)(40). The erosion resistant coatings must mitigating ice buildup to be an effective helicopter leading edge material. The ice adhesion strength of a material is the most important characteristic that limits the amount of accreted ice before natural ice

shedding. The lower the adhesion strength, the less ice will accrete. Also, mechanical de-icing systems that rely on creating stresses greater than the ice adhesion strength require less power if the leading edge has a lower adhesion coating. This chapter will cover experimental research on the ice adhesion strength of erosion resistant coatings. Titanium nitride and titanium aluminum nitride material systems, were evaluated and compared to current metallic leading edge erosion cap materials.

3.2. Testing Facility Overview

The Adverse Environment Rotor Test Stand (AERTS) at the Pennsylvania State University is powered by a 120 HP motor that can spin rotor blades up to ten feet in diameter at an RPM of 1000 (see Figure 49). Four slip rings carry 48 signal channels and 24 power channels from the rotating frame of the rotor to the fixed frame of the control room. A ballistic wall surrounds the rotor to protect from shed ice projectiles. The hover stand is enclosed in a 20 ft x 20 ft 20 ft walk-in freezer capable of maintaining temperatures from 0°C to -25°C.

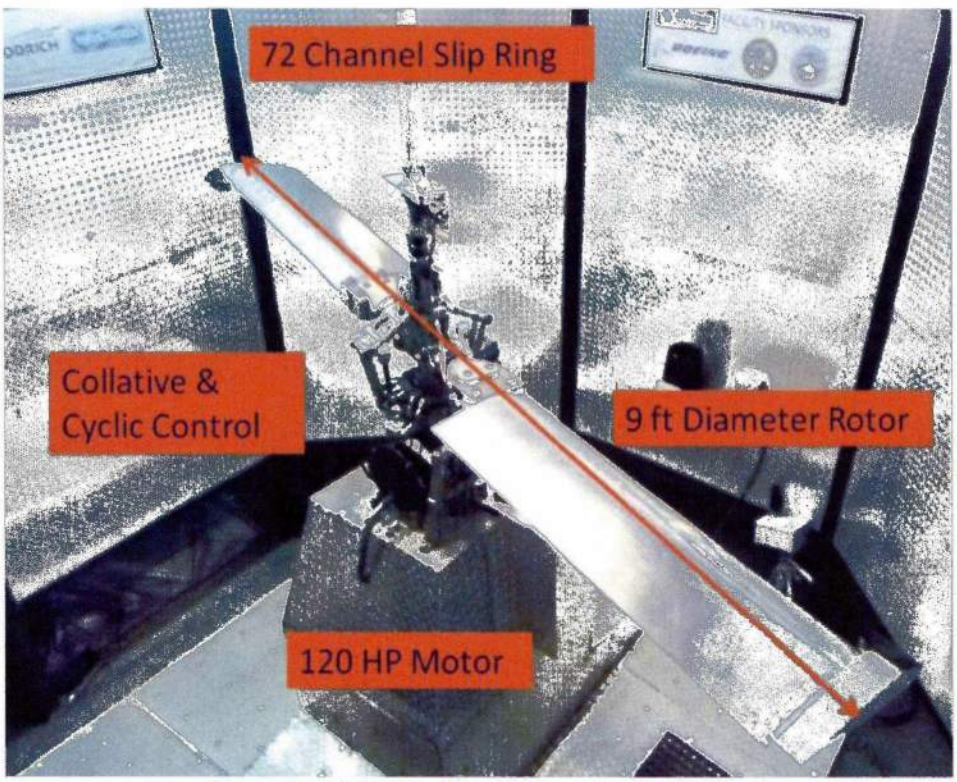

Figure 49: AERTS facility with ice adhesion blades

The facility can produce representative icing conditions as outlined in the Federal Aviation Regulation Part 25 and Part 29 Appendix C (13). The AERTS facility uses NASA standard icing nozzels seated in the ceiling to control the water droplet median volumetric diameter (MVD), and liquid water content (LWC) of the icing cloud (9).

3.3. Ice Adhesion Measurement

Some ice shedding techniques accrete the ice in an icing wind tunnel, and then the accreted ice is transported to an ice removal rig. During the transportation of the accreted ice, potential mechanical and thermal stresses could be introduced, polluting the ice adhesion strength results, and explaining the large spread in ice adhesion data to date (16)(41). In addition, a mechanical force ice removing system might introduce unwanted moments on the accreted ice for different ice shapes, providing fictitiously low results. Examples of other ice shedding systems are vibrating beams (42), centrifuges (43), and pull tester (44). In this research, ice adhesion strength is measured without interacting with the accreted ice. Ice forms on the tip of a rotor blade and sheds naturally under centrifugal loads. The ice adhesion strength is quantified from the measured shedding load and the ice adhesion area. Details of the system are given below.

The blades used for these experiments were specially designed for determining ice adhesion strength. The test fixture at the tip of the beams was designed similar to the test fixture used by the National Research Laboratory in Ottawa (45). The tips of the blades house a beam that bends under centrifugal loading. A full Wheatstone Bridge senses the bending strain and filters out axial loads and temperature changes. As the test coupon, attached to the tip of the beam accretes ice, the centrifugal force on the beam increases due to the additional ice load, and the beam bends in the span wise direction. The strain gauges measure the additional deflection of the beam given the ice accretion (16). A photograph of the rotor tip beams and the assembled system is shown in Figure 50.

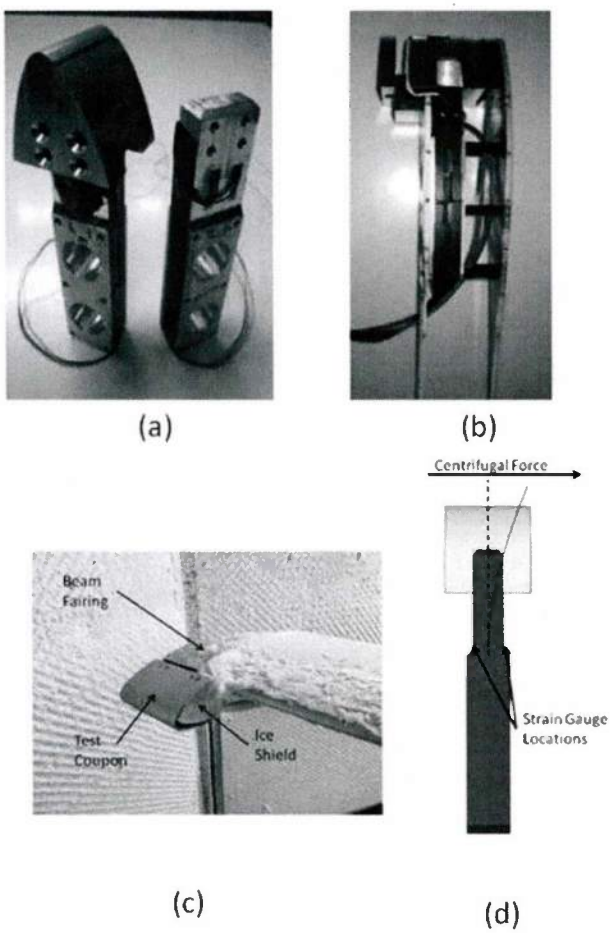

Figure 50: (a) Adhesion beam with exposed strain gauges, (b) Adhesion beam tip assembly, (c) Adhesion beam with blade assembly, and (d) Adhesion beam with exaggerated bending center line

As the beam bends outward along the span direction, the voltage read across the strain gauges decreases. When the ice has accreted a large enough mass such that the centrifugal load surpasses the ice adhesion strength of the test material, the ice de-bonds and sheds off. The event is captured by a sharp increase in voltage from the strain gauges as the beam retracts. An example of the beam relaxation upon ice shedding is shown in Figure 51.

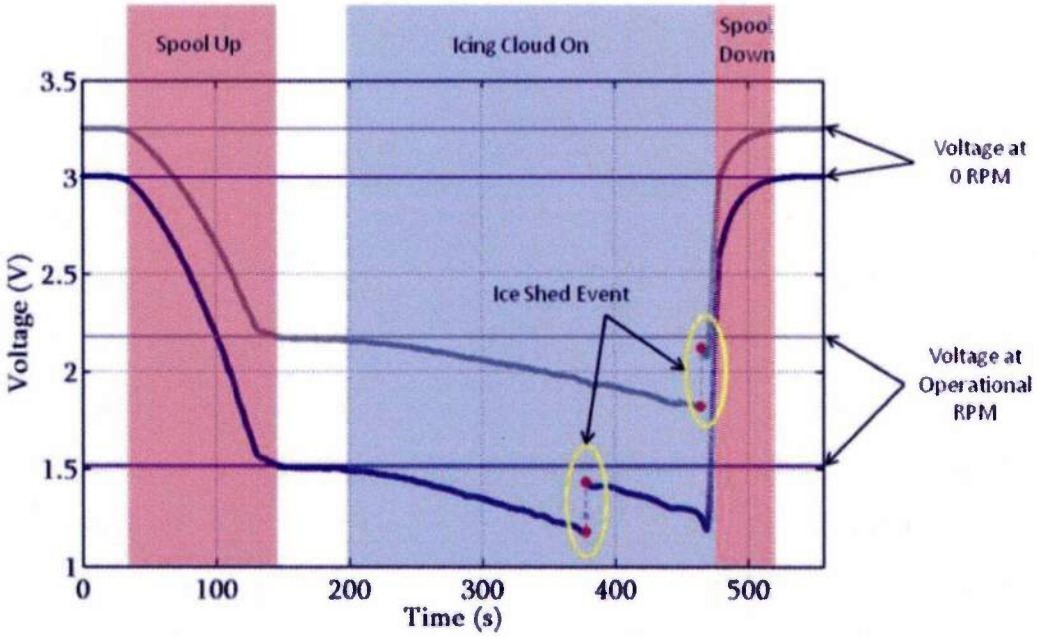

Figure 51: Example of voltages read from strain gauges during test

The sensors are calibrated during each test by knowing the tip mass (M_{tip}), the blade length (R), the voltage read by the strain gauges at zero RPM (V_0), and the voltage read by the gauges at the desired operational RPM (V_{RPM}). The ice load is extrapolated using the voltages read by the strain gauges at a shedding event. The calibration and ice load calculation is depicted by Figure 52 and summarized by Equation 16 (16). Once the ice sheds, the ice shed-area is determined from measuring the area by using graph paper, as depicted in Figure 53. The ice adhesion strength is determined as the ratio of the ice load prior to shedding over the shed area (Equation 17).

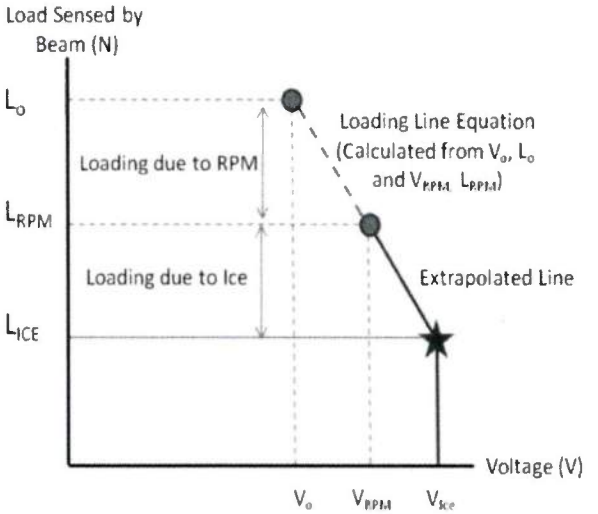

Figure 52: Ice load calibration

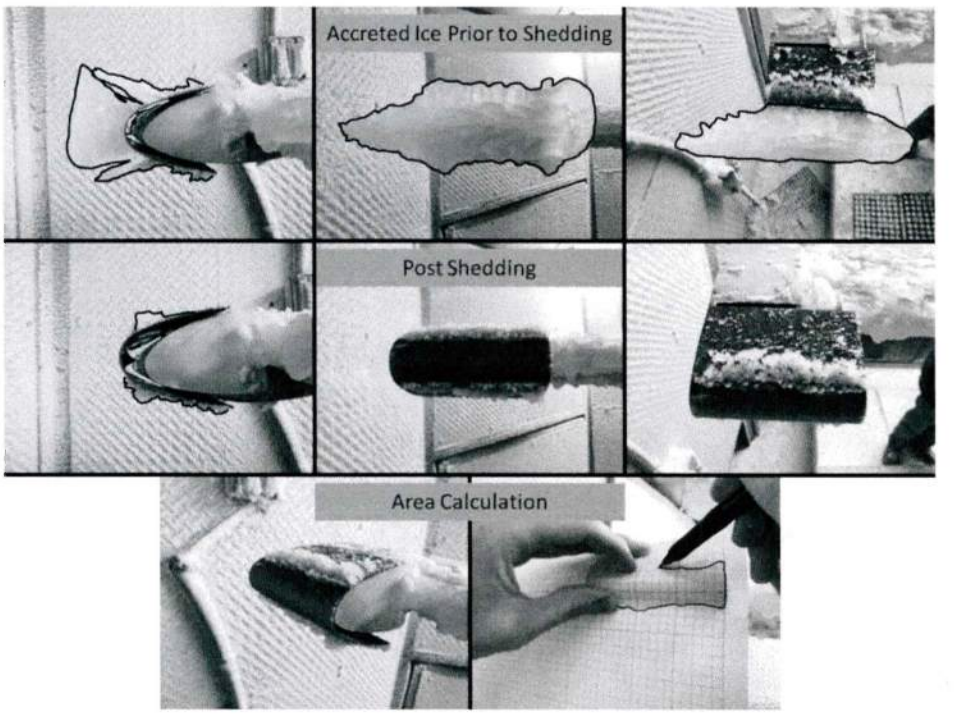

Figure 53: Pre and post ice shed photos and area measuring technique

$$Calibration\ Slope = \frac{M_{tip} R \left(RPM * \frac{\pi}{30}\right)^2}{V_{RPM} - V_0} \qquad \textbf{Equation 16}$$

$$Adhesion\ Strength = \frac{(V_{shed} - V_{final}) * Slope}{area} \qquad \text{Equation 17}$$

As mentioned, the benefits of this ice adhesion strength measurement procedure is the hands-off approach. There is no operator interaction with accreted ice that could introduce outside influence into the ice adhesion strength results. Previous research done by Brouwers et al. (16) used the same bending beam concept; however, the heaters used to mitigate ice bridging polluted the data by leaking heat to the specimen and reducing the overall ice adhesion strength.

3.4. Environmental and Material Surface Effects

Tests were conducted to determine which icing and materials properties have the strongest impact on ice adhesion strength. The parametric testing was performed on stainless steel 430. The parameters studied were:

- Liquid Water Content (LWC) of the icing cloud
- Median Volumetric Diameter (MVD) of the water droplets
- Ambient Temperature
- Material Surface Roughness
- Material Grain Orientation

An outline of the test matrix used during this research is shown in Table 3. The range of values chosen for the environmental conditions cover the majority of the icing envelope and the specimen surface roughness values cover most of the erosion range observed on helicopters (16). During testing, the rotor RPM was maintained at 400 (tip speed of 192 ft/s (58.7 m/s)). The speed of the rotor is limited to 400 RPM due to the torque required to test high drag ice shapes that occurred on coatings with high surface roughness at low temperatures. The 0° grain direction refers to the cases when the grain orientation runs parallel to the span of the blade.

Table 3: Test matrix for environment and material surface ice adhesion influence determination

	Temperature Variation			MVD Variation			LWC Variation		
Temp (°C)	-5	-10	-15	-10	-10	-10	-10	-10	-10
MVD (μm)	30	30	30	20	30	40	30	30	30
LWC (g/m^3)	2	2	2	2	2	2	0.5	2	5
RPM	450	450	450	450	450	450	450	450	450

	Surface Roughness/Grain Direction Variation					
Temp (°C)	-10	-10	-10	-10	-10	-10
MVD (μm)	30	30	30	30	30	30
LWC (g/m^3)	2	2	2	2	2	2
RPM	400	400	400	400	400	400
Grain Orientation (°)	0	90	0	90	0	90
Ra (μin)	24	24	45	45	105	105

3.4.1. Environmental and Material Surface Adhesion Results

As seen in Figure 54, at a temperature of -10° C, variations in the LWC of the cloud have no effect on ice adhesion strength inside the range of LWCs that spans the icing envelope (13). It was proposed to run adhesion experiments at very high LWCs to decrease the duration of the tests. Performing experiments at high LWC values was not practical for obtaining actual physical values since the adhesion strength decreases significantly as the cloud density exceeds the parameters described in the icing envelope (13). At 5 g/m^3 the adhesion strength is 2.8 times lower than at 0.5 g/m^3. Testing at high LWC conditions might reduce testing time, as practiced in (16), if the objective is to compare materials with the understanding that the adhesion values will be underestimated.

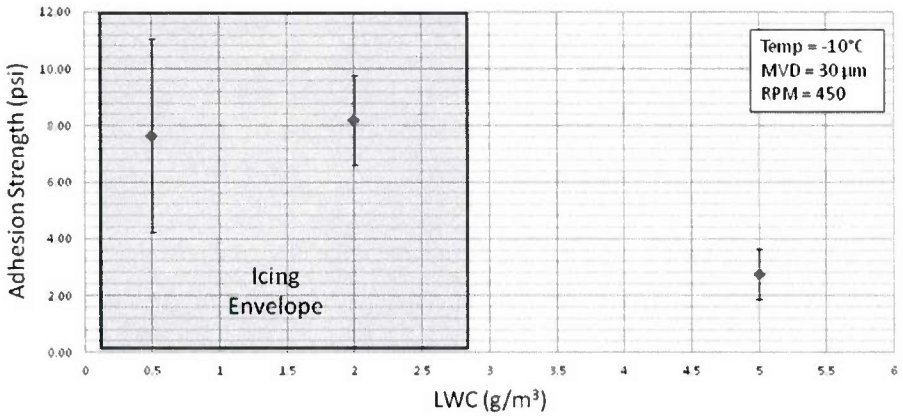

Figure 54: Ice adhesion strength with LWC variation

At higher LWCs, the rate at which the super-cooled water droplets impact the surface increases. This allows more heat to be transferred from the droplets to the test sample since the droplet temperature is near the freezing point, and the test sample is well below this value. In Figure 55, it can be observed that there is a greater temperature rise and higher maximum temperature measured on the surface of the stainless steel coupon for the 5.0 g/m^3 LWC case. The temperature rise at 5 g/m^3 LWC was 2.6 times higher than the 0.5 g/m^3 case. Increasing the surface temperature to close to or slightly above freezing in some cases will decrease the adhesion strength. This sharp increase in surface temperature has also been observed in the NASA Glenn Icing Research Tunnel (44).

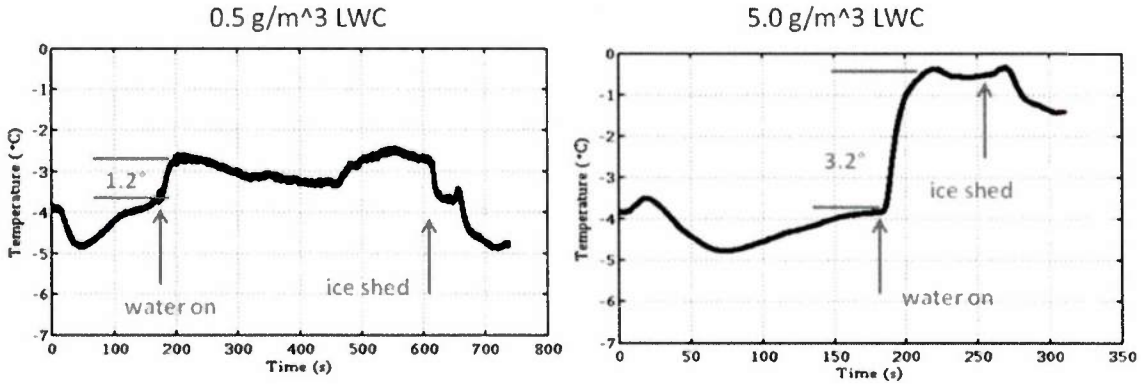

Figure 55: Test specimen surface temperature for (left) 0.5 g/m^3 LWC and (right) 5 g/m^3 LWC

The trend between ice adhesion strength and water droplet MVD was quantified to be negatively correlated and linear (see Figure 56). Ice adhesion strength decreased with MVD at a rate of -0.47 psi per μm. Over the testing domain, the change in adhesion strength was 9.5 psi. From 20 μm to 40 μm MVD the ice adhesion strength decreased 65%.

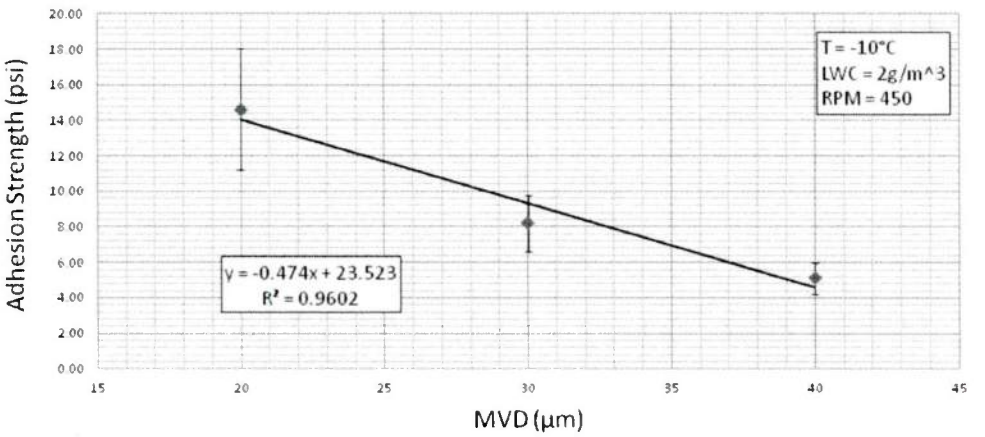

Figure 56: Ice adhesion strength with MVD variation

The last environmental condition tested was temperature. Results related to temperature variation are shown in Figure 57. As the atmospheric temperature decreased, the ice adhesion strength increased at a rate of -2.08 psi per degree. Over the domain, the change in adhesion strength is 21 psi. From -8°C to -16°C, ice adhesion strength increased 670%.

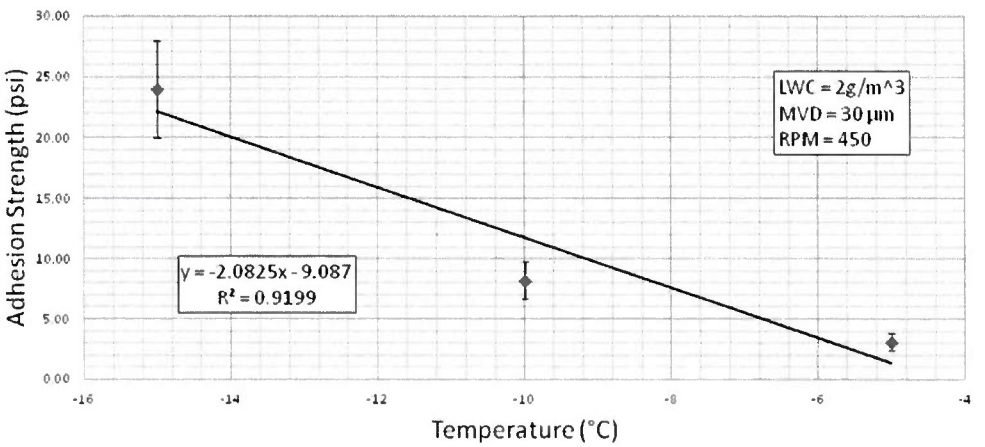

Figure 57: Ice adhesion strength with temperature variation

The two material properties tested were surface roughness and grain direction. The trend between surface roughness and adhesion strength is linear and positive, as seen in Figure 58. The rate of change in ice adhesion strength with surface roughness for the 0° grain direction material was measured to be 0.89 psi per *μin Ra* and 1.01 psi per *μin Ra* for 90° grain direction material. Over the 0° grain direction testing domain, the change in adhesion strength was 71.8 psi, and over the 90° grain orientation testing domain, the change in adhesion strength was 81.2 psi. The average change in ice adhesion strength from 24 μin Ra to 105 μin Ra was 250%. Even thought the 90° grain direction data set had slightly higher ice adhesion strength, the values were within the standard deviation of the test. The average difference in adhesion strength between the 0° and 90° grain direction is 8.8 psi or 15%.

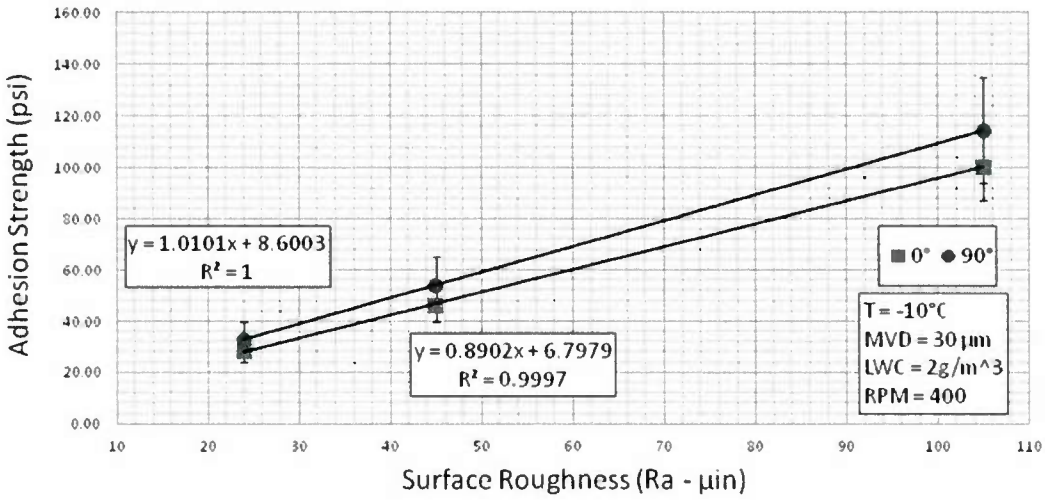

Figure 58: Ice adhesion strength with surface roughness and grain orientation

Two parameters affected ice adhesion strength more severely than other tested parameters, as summarized in Table 4. Ambient temperature was determined to be the most important parameter affecting ice adhesion, with a 670% change in ice adhesion strength for a temperature change from -8°C to -16°C. The next most important property measured was material surface roughness, with a 250%

change in ice adhesion strength from 24 μin *Ra* to 105 μin *Ra*. Surface roughness and temperature were the parameters varied during testing of uncoated metallic and erosion-resistant coatings.

Table 4: Summary of % change over testing range

Properties	% Change Over Range
LWC	7
MVD	65
Temperature	670
Surface Roughness	250
Grain Direction	15

3.5. Erosion Resistant Material Ice Adhesion Testing

A variety of erosion-resistant materials and coating systems were evaluated for impact ice adhesion strength over a range of temperatures and surface roughness values. Three materials currently used for erosion caps in rotor blades (stainless steel 430, titanium grade 2, and inconel 625) were compared to two next generation erosion coating systems (titanium nitride, titanium aluminum nitride). The titanium nitride and titanium aluminum nitride erosion resistant coatings were deposited on Ti-grade 2 substrates by cathodic arc physical vapor deposition (CA-PVD) process. During the cathodic arc coating process, a voltage is applied to the cathode while a grounded trigger contacts the cathode to initiate the arc. This arc movement is constrained to the target face using magnets. The physicality of the motioning arc is a successive sequence of ignition and extinction of discrete sites referred to as cathode spots. These cathode spots vary in size from about 1-10 microns, have a high current density (10^6-10^8 A-cm^{-2}), and their lifetime is about 10 nanoseconds to 1 microsecond. The accumulation of these cathode spots creates a dense plasma of the cathode material. The high pressure of the cathode spot ejects ionized and molten material from the cathode surface into the chamber, thus forming the plasma. Plasma generation is proportional to the supplied current by the power supply: a higher current will result in more cathode spots. This plasma is ionized with energetic ions that promote the adhesion and formation of dense coatings on the substrate.

Prior to deposition, the substrate surfaces were abrasively blasted using alumina grit under various conditions to remove the oxide layer (improved adhesion) and obtain the desired substrate surface roughness (20, 50, and 100 μinch R_a). The substrates were then degreased with acetone, cleaned with methanol, and placed in the deposition chamber. The chamber was evacuated to a base pressure of 2×10^{-6} mTorr. The samples were then ion etched in a 1.2×10^{-2} mTorr argon atmosphere at a -1000V bias. A metallic Ti bond layer was deposited as a compliant interface between the substrate and the TiN and TiAlN coatings. The substrate temperature of each deposition was kept below 350°C. For the nitride-based coatings, nitrogen gas was introduced into the chamber in order to react with the metallic vapor to form the TiN and TiAlN coatings. Primary deposition parameters used to deposit the monolithic TiN and TiAlN coatings were: 12 mTorr N_2 pressure, -50V substrate bias, and 65 A and 60 A evaporator current for Ti and TiAl cathodes, respectively. The materials tested were:

- Stainless steel 430
- Inconel 625
- Titanium grade 2
- Titanium aluminum nitride (TiAlN)
- Titanium nitride (TiN)

After determining the most influential parameters for impact ice adhesion strength, the selected test matrix for testing of erosion resistant coatings is summarized in Table 5.

Table 5: Test matrix for erosion resistant material testing

Roughness (Ra-μin)	20			50			100		
MVD (μm)	25			25			25		
RPM	400			400			400		
LWC (g/m^3)	2			2			2		
Temp °C	-8	-12	-16	-8	-12	-16	-8	-12	-16

Grit blasting was used to alter the surface roughness of the uncoated metallic samples and the titanium grade 2 substrates for the coatings. The surface roughness was measured using an optical profilometer, see Figure 59 for sample images of the three TiAlN coatings. By varying the material and speed of the abrasive particles, it was easy to accurately alter the surface roughness of the uncoated metallic materials and titanium substrates. Once the nitride coatings were deposited on the titanium grade 2 substrate, the surface roughness of the coated samples increased. The TiAlN coating increased the surface roughness by up to 60% and the TiN coating increased the surface roughness by up to 28%.

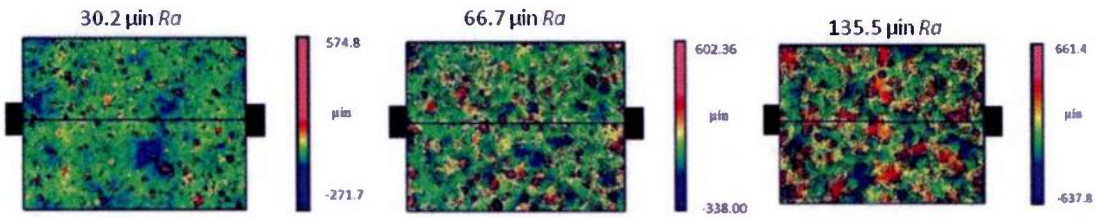

Figure 59: Optical profilometer imagery of TiAlN coated titanium grade 2

The four primary surface roughness measurements for each specimen tested can be seen in Table 6. *Ra* is the average of the absolute values, *RMS* is the root mean square, *PV* is the peak to valley height, and *Rz* is the average distance between the highest peak and lowest valley on the surface of a given material.

Table 6: Surface roughness values for test coupons

	Ra, µin	RMS, µin	PV, µin	Rz, µin
SS430	24.0 ± 2.2	31.0 ± 3.4	421.4 ± 77.7	325.9 ± 37.5
	45.1 ± 2.6	59.3 ± 4.3	749.4 ± 51.7	557.2 ± 25.6
	105.3 ± 3.6	135.2 ± 4.7	1192.5 ± 127.3	1042.8 ± 26.4
IN624	19.8 ± 1.4	25.3 ± 1.8	409.7 ± 110.4	279.9 ± 13.6
	45.0 ± 2.7	57.2 ± 3.3	597.9 ± 75.8	493.8 ± 8.7
	90.7 ± 4.2	116.0 ± 6.5	975.8 ± 118.2	875.7 ± 103.8

Ti	26.4	±	0.9	33.4	±	1.0	393.7	±	42.4	310.4	±	8.4
	41.8	±	1.5	54.5	±	2.2	667.0	±	76.6	529.2	±	28.2
	86.1	±	6.0	110.7	±	8.6	1075.8	±	190.7	890.5	±	120.7
TiN	35.4	±	7.8	57.2	±	16.0	1026.7	±	75.1	886.9	±	102.6
	109.9	±	10.6	142.2	±	15.1	1318.5	±	134.6	1202.3	±	136.9
TiAlN	30.2	±	3.4	46.2	±	8.8	839.9	±	317.8	732.1	±	289.9
	66.7	±	5.2	91.4	±	9.1	1144.4	±	218.7	1055.4	±	218.4
	135.5	±	7.9	178.6	±	14.8	1714.9	±	251.5	1585.4	±	247.6

3.5.1. Empirical Temperature Extrapolation

Due to the fact that ice adhesion strength varies linearly with temperature from -8 to -16°C, adhesion strength can be extrapolated from one data point if the temperature dependence of adhesion strength is known for a given material. First, the sample with the lowest roughness was tested over a range of temperatures, and a linear curve was fitted to obtain the ice adhesion strength temperature trend. Next, the other surface roughness values were tested at the warmest of the ice testing conditions. The adhesion strength was extrapolated from the warm cases by multiplying the curve fit by the ratio of high surface roughness adhesion strength to lower surface roughness adhesion strength (AS).

$$Predicted\ AS(50\mu in, Temp) = (Linear\ Trendline\ Equ.)\frac{AS(50\mu in, -8°C)}{AS(20\mu in, -8°C)} \quad \textbf{Equation 18}$$

The benefit of extrapolating the ice adhesion strength is the minimization of the test matrix, since the method provides a first-order approximation for conditions that are difficult to test, i.e. colder temperatures and higher surface roughness values. This extrapolation method was validated while testing

the uncoated uncoated metallic materials and then implemented to reduce the test matrix size for the erosion coated coupons.

3.5.2. Ice Adhesion Results for Uncoated Metallic Materials

The ice adhesion strength values for uncoated stainless steel 430 can be seen in Figure 60. As expected, the adhesion strength increased as the temperature decreased and surface roughness increased. Stainless steel 430 had a strong dependence to surface roughness. At -8°C, the adhesion strength of the 105 µin *Ra* sample was 2.2 times greater than that of the 24 µin *Ra* sample. The adhesion strength of the 24µin *Ra* sample at -16°C was 1.7 times higher than at -8°C. The adhesion strength ranged from 21.1 to 86.6 psi over the testing envelope. The average adhesion strength over the entire test matrix is 50.4 psi with an average adhesion standard deviation of 6.0 psi (12%) and an average temperature standard deviation of 1°C (13%) at -8 °C, 1.25°C (10%) at -12°C, and 1.5°C (9%) at -16 °C. The extrapolation method was able to predict most of the points and had a maximum error of 19%.

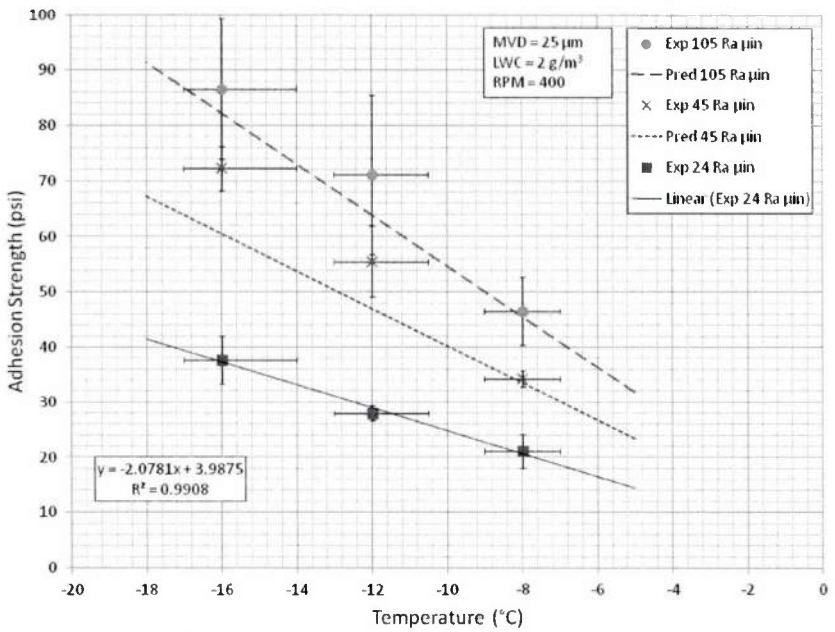

Figure 60: Ice adhesion strength of stainless steel 430 over a range of temperatures and surfaces roughness

As seen in Figure 61, Inconel 625 was slightly less dependent on surface roughness as compared to stainless steel. The ice adhesion strength increased by a factor of 1.4 from the lowest to the highest surface roughness sample at -8°C. The adhesion strength of the 19.8 µin *Ra* sample at -16°C was 2.4 times higher than at -8°C. The adhesion strength ranged from 23.1 to 71.7 psi over the testing envelope. The average adhesion strength over the entire test matrix is 45.0 psi with an average adhesion standard deviation of 7.9 psi (18%) and an average temperature standard deviation of 1°C (13%) at -8°C, 1.25°C (10%) at -12°C, and 1.5°C (9%) at -16°C. The extrapolation could predict the ice adhesion strength for most of the data set. However, the extrapolation had more error at the colder temperatures with higher surface roughness. The experimental results were over predicted by a maximum of 16%.

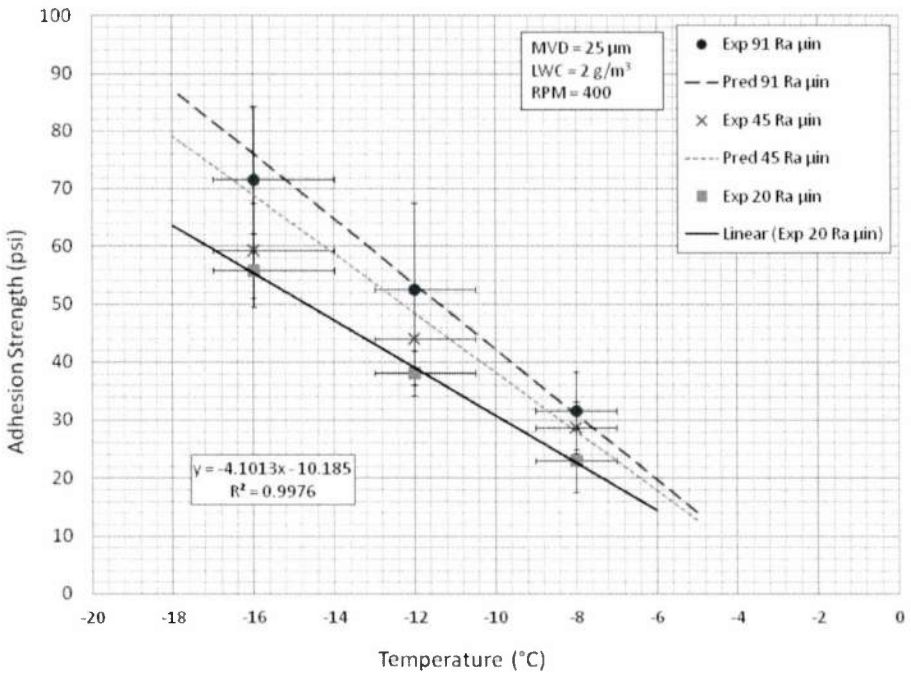

Figure 61: Ice adhesion strength of Inconel 625 over a range of temperatures and surfaces roughness

As seen in Figure 62, Grade 2 Titanium had similar dependance on surface roughness as Inconel 625. The ice adhesion strength increased by a factor of 1.4 from the lowest to the highest surface

roughness sample at -8°C. The adhesion strength of the 26.4 µin *Ra* sample at -16°C was 2.3 times higher than at -8°C. The adhesion strength ranged from 20.1 to 53.6 psi over the testing envelope. The average adhesion strength over the entire test matrix was 36.9 psi with an average adhesion standard deviation of 5.3 psi (14%) and an average temperature standard deviation of 1°C (13%) at -8°C, 1.25°C (10%) at -12°C, and 1.5°C (9%) at -16°C. The extrapolation matched the experimental data well except at the coldest and roughest points. The extrapolation had a maximum error of 23%.

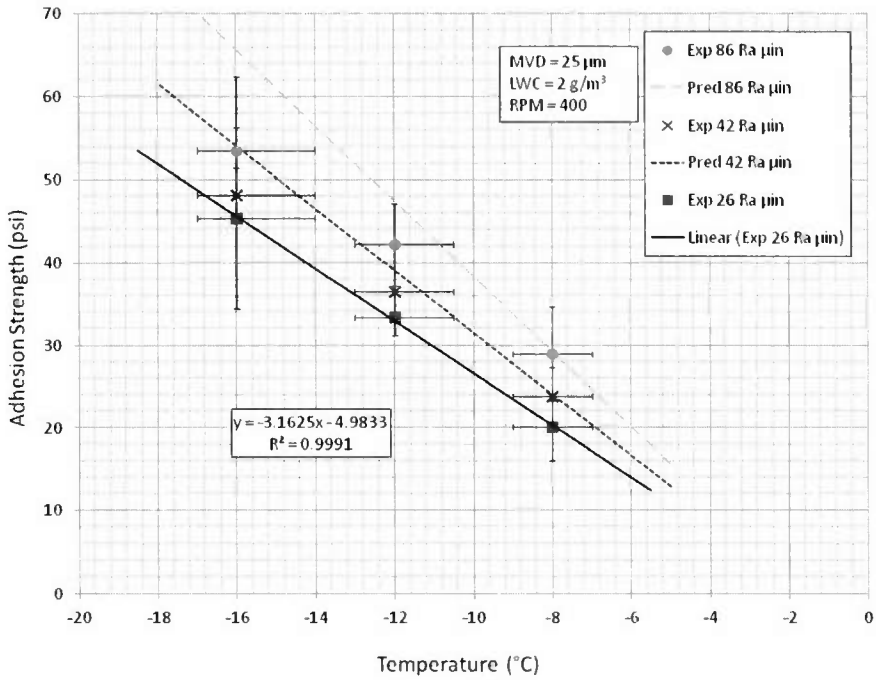

Figure 62: Ice adhesion strength of titanium grade 2 over a range of temperatures and surfaces roughness

3.5.3. Sources of Experimental Uncertainty

Obtaining standard deviations of up to 20% may seem high for most scientific studies; however, this is an acceptable limit for icing adhesion testing. Brouwers et al. (16) had an average deviation of 23%, Hassan et al. (42) had an average deviation of 40%, and an 18% deviation was observed by Laforte et al. (41). The AERTS facility uses the same NASA standard icing nozzles that aerosolize water into a

bell curve of particle sizes around the desired MVD, as used in the NASA Glenn Icing Research Tunnel. Tsao and Kreeger, explain the deviation in MVD and LWC can be as high as ±12% for each parameter (46). Compounding the two effects can quickly lead to large standard deviations during ice testing. A second issue arises with the time response of the MVD feedback control system. The system may take up to 20 seconds to stabilize the water pressure needed to generate a desired particle size. The wide range of particles created during this stabilization period has a larger effect on ice adhesion testing as compared to icing studies such as ice shape correlation. The first few seconds of icing develops the interface between the ice and the substrate that is the most important feature during ice adhesion testing. Spraying high variability particle sizes during the development of the icing cloud can cause large standard deviations given that ice adhesion strength can change up to 50% as a consequence of changing MVD. A discrepancy in ice adhesion strength of 20% is considered acceptable for ice adhesion testing due to the difficulty in generating an icing cloud with no variation in the water droplet particle size.

3.5.4. Ice Adhesion Results for Nitride-Based Coatings

Since the extrapolation method has been demonstrated to predict ice adhesion strength for varying temperatures within the standard deviations of the icing tests on metallic materials, the procedure was implemented to reduce the test matrix size used for the evaluation of ice adhesion strength of TiN and TiAlN coated samples. At the lowest surface roughness value for TiN, the adhesion strength increased by a factor of 2.9 from -8°C to -16°C as seen in Figure 63. At -8°C, the adhesion strength increased by a factor of 1.6 from the 35 µin *Ra* sample to the 110 µin *Ra* sample. The average ice adhesion strength of TiN over all of the testing conditions was 61.3 psi with an average standard deviation on 5.9 psi (10%). The significantly higher ice adhesion strength is attributed to a rougher TiN coated with a high peak-to-valley (PV) value almost 2.5 times higher than the equivalent uncoated Ti grade 2 alloy. The higher surface roughness is due to the un-optimized coating process. During the cathodic arc deposition process, molten material (termed a macroparticle) can be ejected at shallow angles from the cathode surface. The ejection of macroparticles (usually 1-10 microns in size) is the main disadvantage of cathodic arc deposition process. Low melting temperature cathodes generally experience an increased number of

large-sized macroparticles. There are multiple variables that can reduce macroparticle concentration within the coating. The use of magnets on the target assembly steers the arc on the cathode and in effect minimizes the time a cathode spot resides on a certain area. Steering the arc with the use of magnets assists in the dissipation of heat on the cathode surface but also decreases the evaporation rate of the cathode. Another cathode cooling mechanism is through a chilled water loop located behind the target. The cooled cathode will have less molten material on its surface and therefore a reduced number of liquid globules will result. The use of a background gas also deters macroparticle generation because it elevates the chamber pressure, effectively increasing the melting point of the cathode. The most effective macroparticle reduction comes in the form of a physical filter (filtered cathodic arc). These filters commonly come in different geometries but most all have some sort of bent tube. Macroparticle filters are efficient but they significantly reduce the deposition rate. If the other suggested macroparticle deterrents are utilized, minimal macroparticles could be incorporated in the coating to reduce the overall surface roughness.

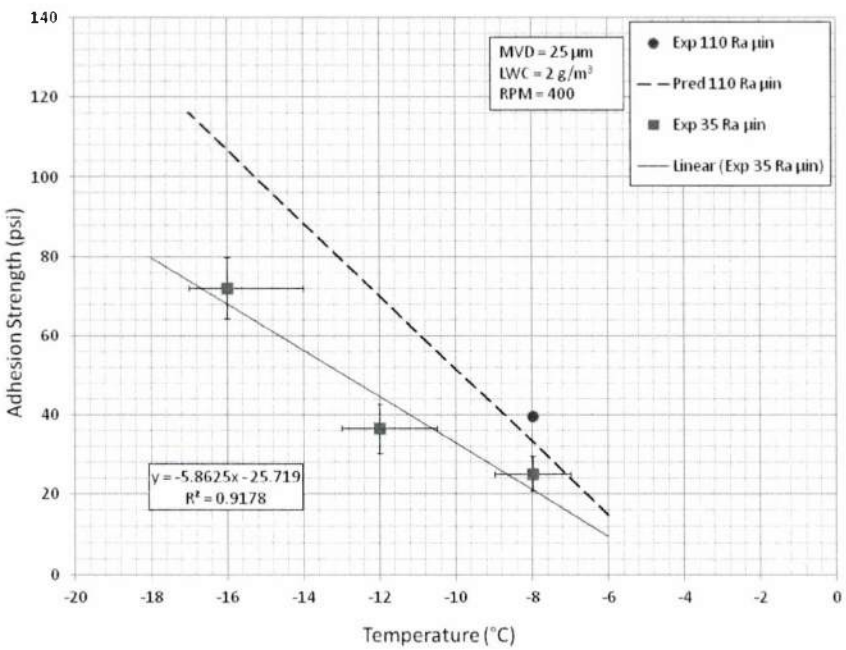

Figure 63: Ice adhesion strength of TiN over a range of temperatures and surfaces roughness

Over the temperature range of -8°C to -16°C, the adhesion strength of ice to TiAlN increased by a factor of 2.0 for the 30.2 µin *Ra* sample (Figure 64). The adhesion strength was so high that there was not enough power on the hover stand to shed the ice off samples with a surface roughness greater than 30 µin *Ra*. After 20 minutes of ice accumulation, the maximum motor power limit of the stand was reached. At that point, the ice that had accumulated provided an estimate of the lower threshold for ice adhesion strength for the 66.7 µin *Ra* sample. Note the arrow in Figure 64 signifying the actual adhesion strength would be higher than the data shown, since the 66.7 µin *Ra* could not be shed naturally. Comparing the adhesion strength of the 30.2 µin *Ra* sample to the lower estimation for the 66.7 µin *Ra* sample at -8°C, there was an increase by a factor of 1.8 making the adhesion strength of TiAlN very dependent on surface roughness. A conservative average ice adhesion strength for TiAlN over the tested conditions was 75.1 psi with a standard deviation of 9.3 psi (8%).

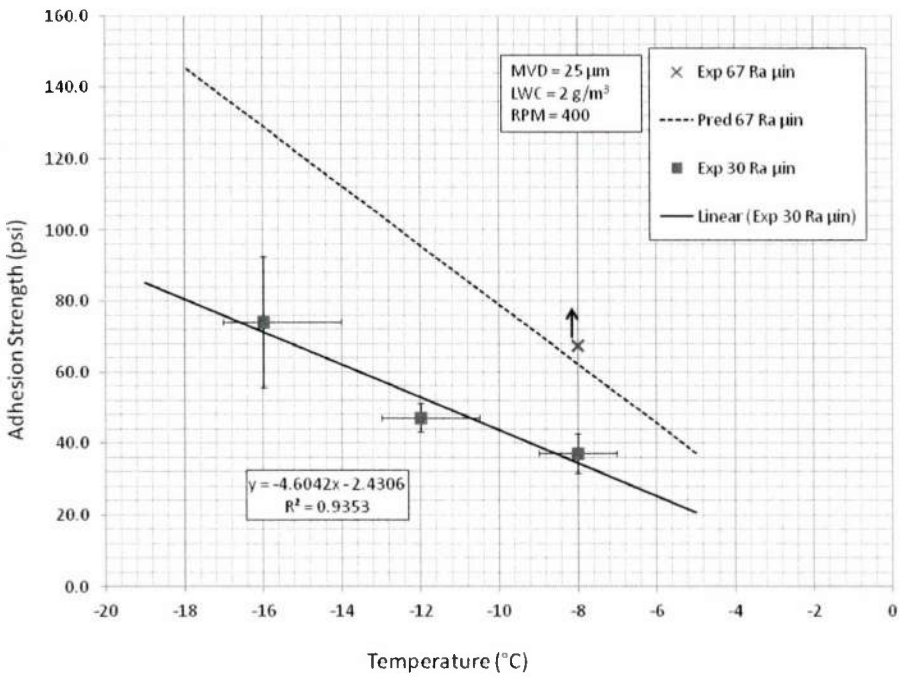

Figure 64: Ice adhesion strength of TiAlN over a range of temperatures and surfaces roughness

3.6. Ice Adhesion Strength Comparison

Since the samples have slight variations in surface roughness with respect to the desired roughness values, the materials were compared by eliminating the effect of temperature from the data and plotted in terms of an adjusted adhesion strength (AAS) values as a function of surface roughness. To develop the adjusted adhesion strength, each adhesion strength value in the test matrix is divided by the ambient temperature for that test (see Equation 19). The three adjusted values for each surface are averaged to calculate one adjusted adhesion strength value for each surface roughness value (see Equation 20). The effect of temperature was eliminated due to the fact that ice adhesion strength varies linearly with temperature for the range tested. The data was reduced by dividing adhesion strength by the ambient temperature and averaged to produce one temperature-adjusted adhesion strength value for each surface roughness.

$$x_i = \frac{Adhesion\ Stength}{Temperature} \qquad \textbf{Equation 19}$$

$$AAS = \frac{\sum_i^3 x}{3} \qquad \textbf{Equation 20}$$

The temperature-adjusted adhesion strength for all of the materials is shown in Figure 65. Once again, the arrow signifies the estimated lower limit of adhesion strength for the TiAlN sample. TiAlN had the strongest dependence on surface roughness followed by TiN and stainless steel 430, then Inconel 625 and titanium grade 2. Stainless steel 430 had an average temperature-adjusted adhesion strength of 4.2 psi/°C, Inconel 625 had an average of 3.7 psi/°C, Titanium had an average of 3.1 psi/°C, TiN had an average of 4.7 psi/°C, and TiAlN had the highest average with 6.3 psi/°C without being able to properly test the high surface roughness range. As discussed earlier, the manufacturing technique for the coatings has not been optimized the *PV* roughness while maintaining *Ra*. Until the *PV* values of the coatings are

brought down to similar values as the substrate, it is an unfair comparison. A summary of temperature adjusted adhesion strength values can be found in

Table 7.

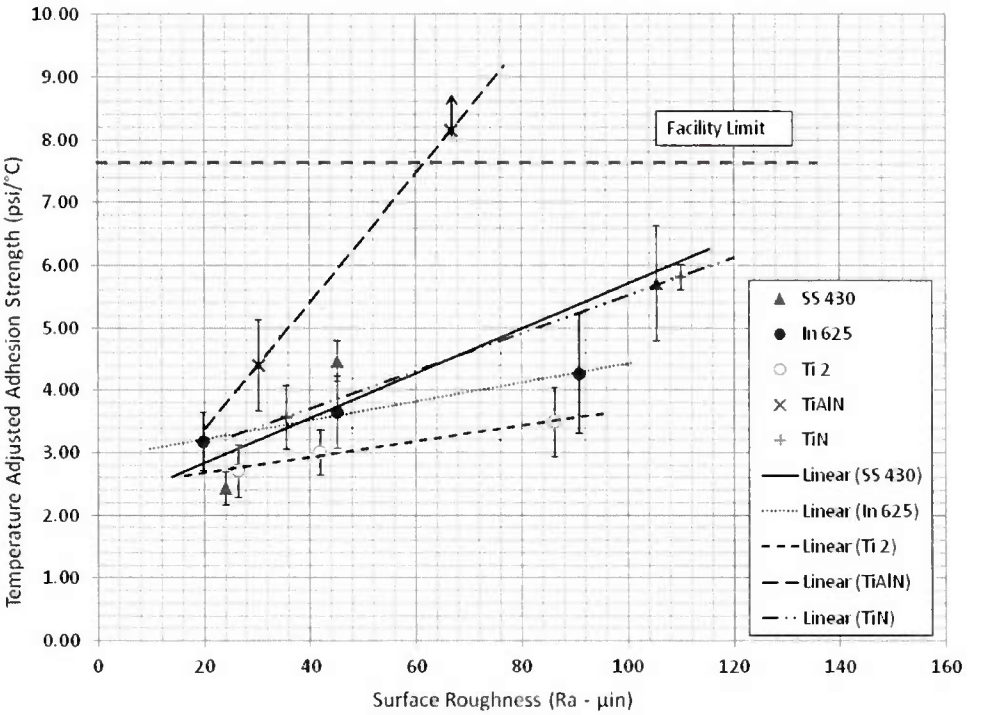

Figure 65: Comparison of temperature adjusted ice adhesion strength

Table 7: Summary of average temperature adjusted adhesion strength values

	psi/°C
Stainless Steel 430	4.2
Inconel 625	3.7
Titanium Grade 2	3.1
TiN	4.7
TiAlN	6.3

In this research, the ice adhesion strength of impact ice to erosion-resistant materials was experimentally measured and compared to that of metallic materials commonly used in helicopter rotor blade leading edges. In addition, the effects of environmental and material surface properties to ice adhesion strength were determined. The high adhesion strength of the nitride coating systems makes these systems impractical to use with mechanical de-icing systems. However, these nitride coating systems are only prototypes. With improved manufacturing techniques to minimize surface disparities, the ice adhesion strength of the nitride coatings can be reduced.

4. Comparison of Electrothermal to Ultrasonic Deicing Systems

4.1. Introduction

The effects of the leading edge coating on an IPS must be understood. The final stage of this research applied a TiAlN erosion resistant coating to the leading edge of two modern de-icing systems. A graphite composite electrothermal IPS is tested and compared to an ultrasonic de-icing system both of which were coated with a TiAlN erosin resistant coating on the leading edge. The de-icing systems were tested on a scaled rotor (Figure 66) and evaluated under two different icing conditions. The two IPSs were compared on power required to de-ice, effectiveness, and reliability.

4.2. Ice Protection System Design & Construction

The TiAlN erosion resistant coating was tested for de-icing performance with electrothermal and ultrasonic ice protection systems (IPS). As seen in Figure 66, the IPSs covered the leading edge of a 30.48 cm (12.0 inch) span test section with a 40.64 cm (16 inch) chord. The protected section was attached to the end of a 77.5 cm (30.5 inch) span carrier blade. The total rotor radius was 140.5 cm (55.5 inch). The blades were spun at 500 RPM which developed a speed of 65.8 m/s (216 ft/s) at the middle of the test

section. The ultrasonic IPS was based on a design from Overmeyer (47) and the electrothermal graphite heater IPS was designed with the help of United Technology Corporation (UTC) Aerospace Systems.

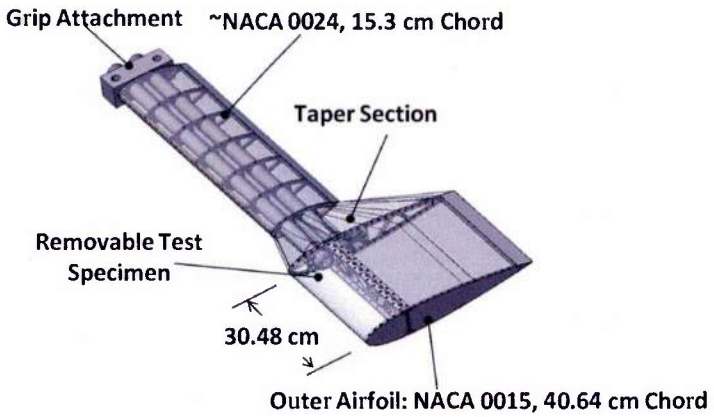

Figure 66: Schematic of de-icing testing rotor blade (47)

4.2.1. Ultrasonic IPS

In 2012, Overmeyer designed and tested a rotorcraft ultrasonic de-icing system in the Adverse Environment Rotor Test Stand. Prior to testing, Overmeyer programmed a custom driving system for the actuators and developed an optimal construction methodology for bonding the actuators into the leading edge. (47). The ultrasonic vibrations were created from a set of circular piezoelectric actuators driven around the first radial resonance mode. The material used for the actuators was lead zirconium titanate type four (PZT-4). The size of the actuators was limited by the curvature of the leading edge and the availability of PZT-4 actuators sizes offered by manufacturers. The larger the diameter, the less contact area the actuator had with the host structure due to the leading edge curvature. A 1.5 inch diameter disk with a 0.05 inch thickness resulted in a balance between actuator diameter and leading edge curvature.

Previous research by Overmeyer developed an optimized bondline. The criteria for the bondline were: the bondline must eliminate actuator failure due to direct solder joints and delamination of the actuator from the host structure. The bondline must adhere the actuator to the host structure, fill any gaps that exist, and conduct electricity to the actuator while insulating the two sides of the actuator from each other as well as the host structure. A parametric study by Overmeyer revealed the ideal bondline that maximizes the transfer of the transverse shear stress from the actuator to the host structure and meeting

the bondline criteria was a combination of FM-73 film adhesive a structural epoxy resin designed for the aerospace industry produced by Cytec Industries ® (47) and an aluminum mesh (47). The FM-73 bonded the actuator to the host structure and served as an electrical insulator. The aluminum mesh carried the electric current and increased the bondline shear modulus of FM-73 from 0.84 GPa to 8.9 GPa, close to the ideal bondline shear modulus. Experimental validation of the optimized bondline showed an increase in the out-of-plane velocity of up to 76% compared to using MasterBond® EP21 as the adhesive (47).

Eight actuators were cured to the leading edge cap using a three cure manufacturing process (see Figure 67). The gap between the top of the actuator and the top electrode is an artifact of the schematic. In reality, the aluminum mesh compressed down to the actuator. The first cure, bonded the bottom aluminum mesh electrode to the actuator and insolated the top of the actuator from the bottom, so the top electrode did not short to the bottom electrode. The second cure adhered the top electrode to the actuator creating a self contained actuator packet electrically insulated from the environment except at the wire terminals. The final cure bonded the actuator packet to the leading edge.

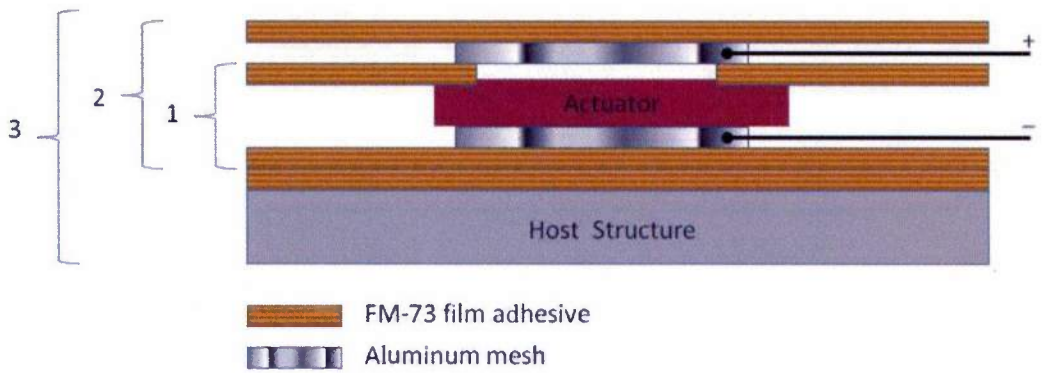

Figure 67: Curing layup for piezoelectric IPS

One packet was cured to the top of the leading edge, and one was cured to the bottom, as shown in Figure 68. Each actuator packet had four evenly spaced actuators (Figure 69). The four actuators near the tip and the four actuators near the root of the blade were wired in parallel to create two de-icing zones. The tip zone was powered first to remove the ice on the tip. When the inboard zone was powered and the inboard ice is shed, the ice at the tip did not block the inboard ice.

Figure 68: Leading edge cap after the installation of one actuator packet

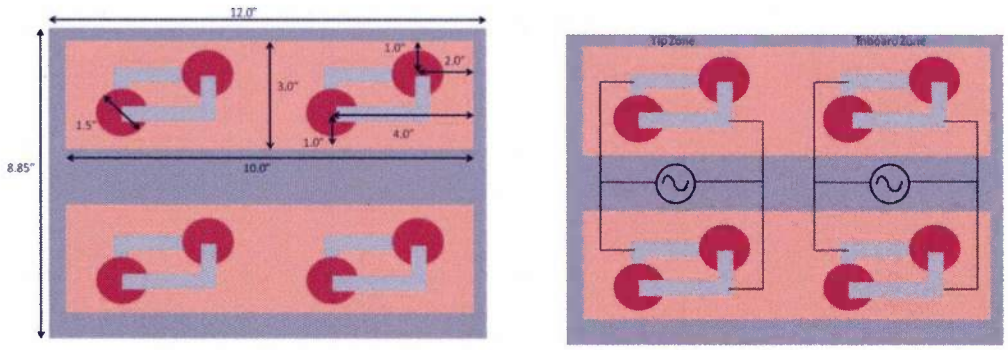

(a) **(b)**

Figure 69: Actuator layout and wiring diagram

4.2.2. Electrothermal IPS

The heating elements for the electrothermal IPS were designed and manufactured with the help of UTC Aerospace Systems. Four heater zones with two elements each made up the heating blanket, as shown in Figure 70. Each element was 10.75 inches long and 0.84 inches wide. Two elements were wired in series to create one heater zone with a resistance of 4.65 ohms.

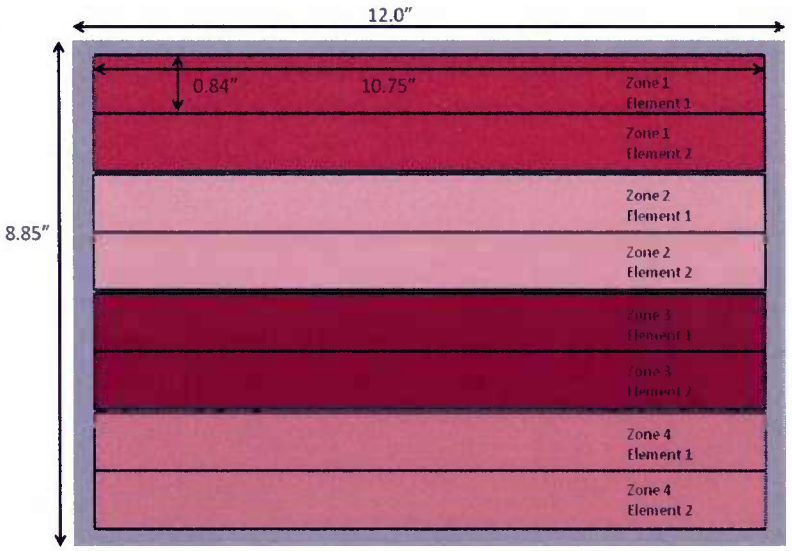

Figure 70: Schematic of electrothermal heater elements that comprise the heater blanket

The heater elements used a carbon composite core, as an electrode, wrapped in a layer of insulating glass composite. A thermistor was cured to the middle of each element to monitor the heater temperature, see Figure 71. The maximum operating temperature of the resin in the composites was 200 °F, so the failsafe limit on the controller was set to 170 °F. After manufacturing, a Forward Looking Infrared (FLIR) camera was used to check for defects such as locations that did not bond properly, see Figure 72. If an element was not bonded correctly, a cold spot would appear in the delaminated region, and if a element had a poor electrical connection and only a fraction of the current was flowing through the heater, the whole heater element would be colder than the rest.

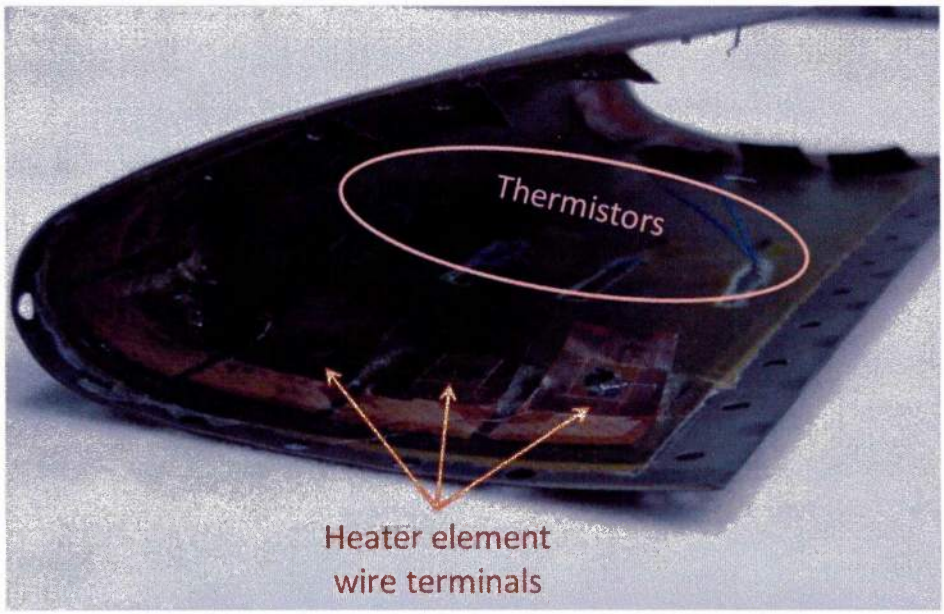

Figure 71: Electrothermal heater elements with thermistors

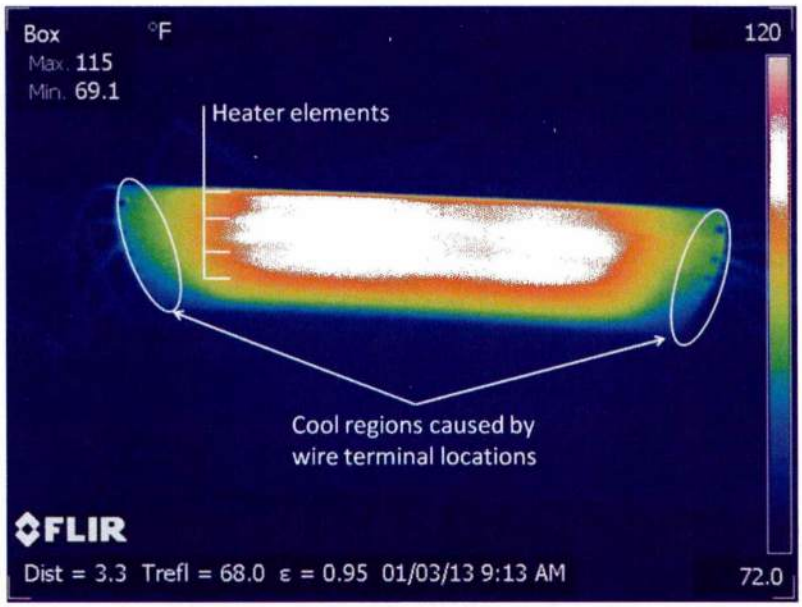

Figure 72: Quality check with FLIR system

4.3. Testing Procedure and Controller Operations

4.3.1. AERTS Facility

The Adverse Environment Rotor Test Stand (AERTS) at the Pennsylvania State University is powered by a 120 HP motor that can spin rotor blades up to ten feet in diameter at an RPM of 1000, see Figure 49. Four slip rings can carry 48 signal channels and 24 power channels from the rotating frame of the rotor to the fixed frame of the control room. A ballistic wall surrounds the rotor to protect from shed ice projectiles. The hover stand is enclosed in a 20' x 20' x 20' walk-in freezer capable of maintaining temperatures from 0°C to -25°C. A series of nozzles in the ceiling vaporize water to create an artificial icing cloud. The difference in the air and water pressure sent to the nozzles controls the MVD.

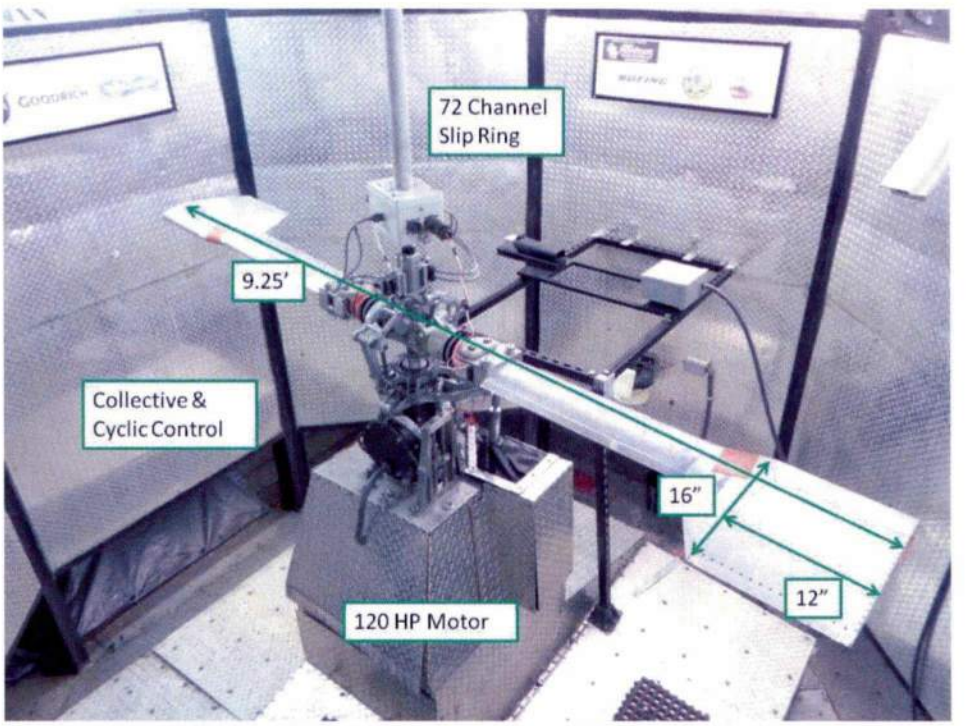

Figure 73: AERTS photograph with de-icing blades

4.3.2. Ultrasonic Driving

There are three main components to the ultrasonic IPS designed by Overmeyer: the controller interface, impedance analyzer, and an actuator driving system, see Figure 74 (47). Upon starting the controller, the state relay connected the de-icing actuators to the impedance analyzer, and the impedance analyzer measured the impedance of each de-icing zone over a bandwidth. The bandwidth was set by the operator and was typically around the first radial resonance of the actuators. A 1.5 inch diameter actuator has a radial resonance of 57 kHz. The bandwidth for a 1.5 inch actuator was set from 40kHz to 70kHz. At low impedances, more power can be achieved for a given voltage input, so the controller selected the frequency with the lowest impedance to drive around. During the driving step, the frequency sent to the actuators was swept from 250Hz below the resonant frequency to 250Hz above the resonant frequency to capture any resolution error from the impedance analyser. The state relay then switched the driving system so high voltages sent to the actuators do not reach the impedance analyzer. The internal impedance matching network of the amplifier was adjusted to match the impedance of the de-icing system. The closer the impedance match between the amplifier and the de-icing system, the less power that was reflected back to the amplifier. Driving the actuators in compression only increased the amount of voltage that can be applied before the actuator fails. To achieve compression only driving, a DC offset was applied to the output voltage of the amplifier.

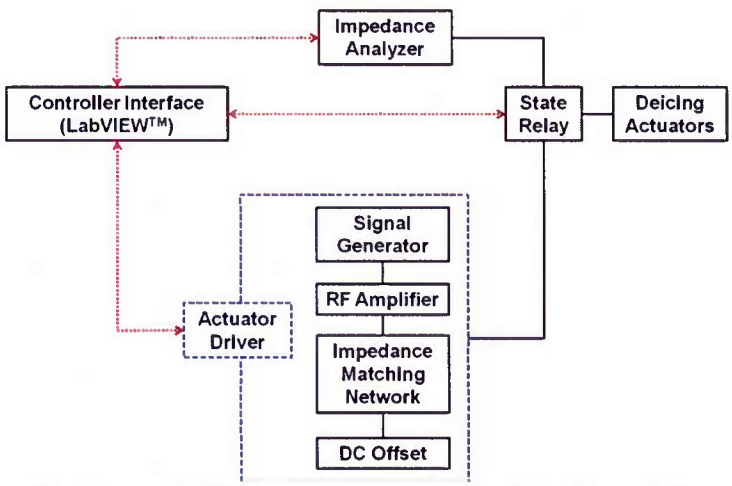

Figure 74: Ultrasonic IPS controller and required hardware (47)

The ultrasonic controller found two impedance minimums for the ultrasonic de-icing system one around 60kHz and the other around 65kHz. During testing, each zone, tip and root, was driven at both frequencies. Since the de-icing system is a dynamic electromechanical system, not all the power sent by the amplifier to the actuators is used; some power was reflected back to the amplifier. The power used by the actuators to do work is the difference between the forward and reverse power called the load power. As seen in Figure 75, the power used by the actuators was constantly changing over time. As a result, both the average power and maximum power will be presented in the results section.

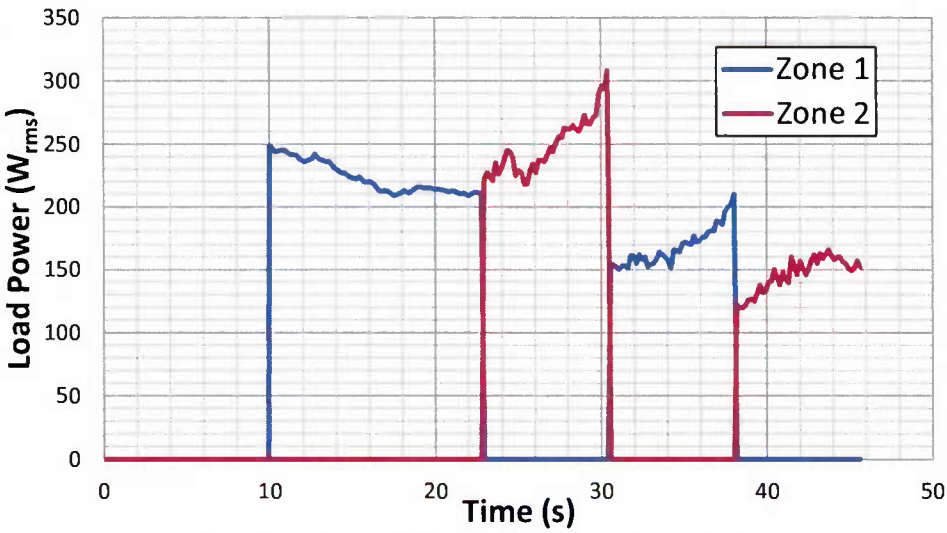

Figure 75: Typical load power used by actuators

4.3.3. Electrothermal Driving

The electrothermal heaters were powered by a 110 volt 20 amp power supply. A variac regulated the voltage down to achieve the desired power. To limit the power required, the heater zones were powered individually in a sequence starting from the aft heaters and moving forward. The zone order was: 1-4-2-3. Each zone was powered for four seconds with no down time between zones. As seen in Figure 76, the heating elements took approximately one second to respond to a 44V applied voltage, and after the voltage was removed, the heaters continued to increase temperature for another 5 seconds. The black line in Figure 76 signifies what heater zone was powered. For the sample test shown in Figure 76, the average

temperature increased by 23°C with an average maximum temperature of 19°C. As signified by the blue line, the ice in the case shown was removed after 17 seconds of heater on time after the last zone reached a temperature on 10°C. For colder test cases, the heaters were cycled multiple times until the ice was removed.

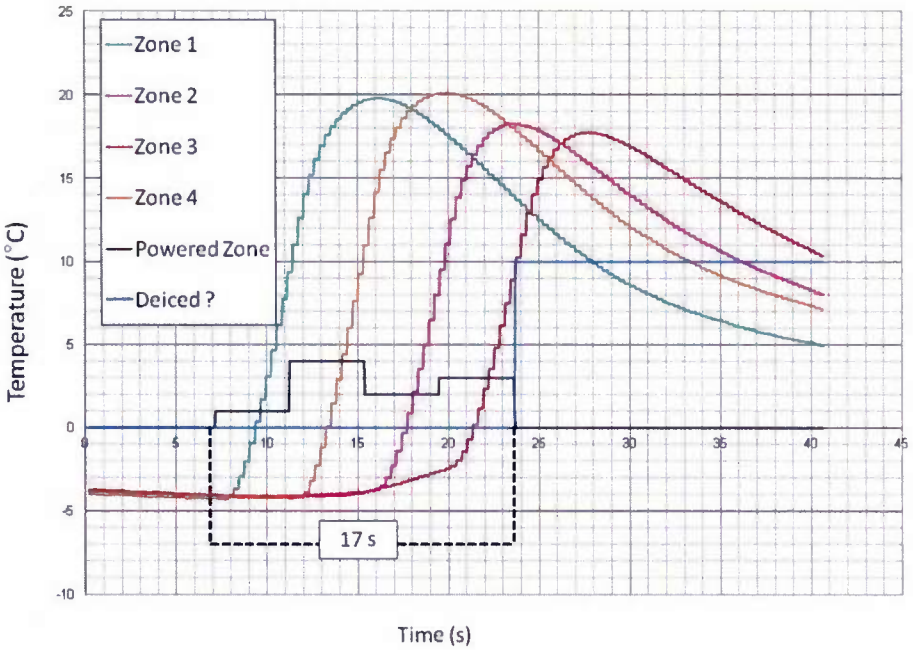

Figure 76: Sample heater temperatures (416W_{rms} & -5°C ambient temperature)

4.4. Results

As discussed in the previous chapter, the most important environmental condition for ice adhesion strength is ambient temperature followed by MVD and LWC. From this knowledge, two icing conditions were chosen to compare electrothermal de-icing to ultrasonic de-icing. Temperature and MVD were changed while holding LWC constant. As seen in Figure 77, both icing conditions fall within the continuous icing envelope. Case A was the colder test condition at -15°C with a MVD of 15μm and LWC of 0.4 g/m^3. Case B had a temperature of -8°C with a MVD of 25μm and LWC of 0.4 g/m^3. Case B was

tested first since the potential for system failure due to over power was higher for the colder condition case A.

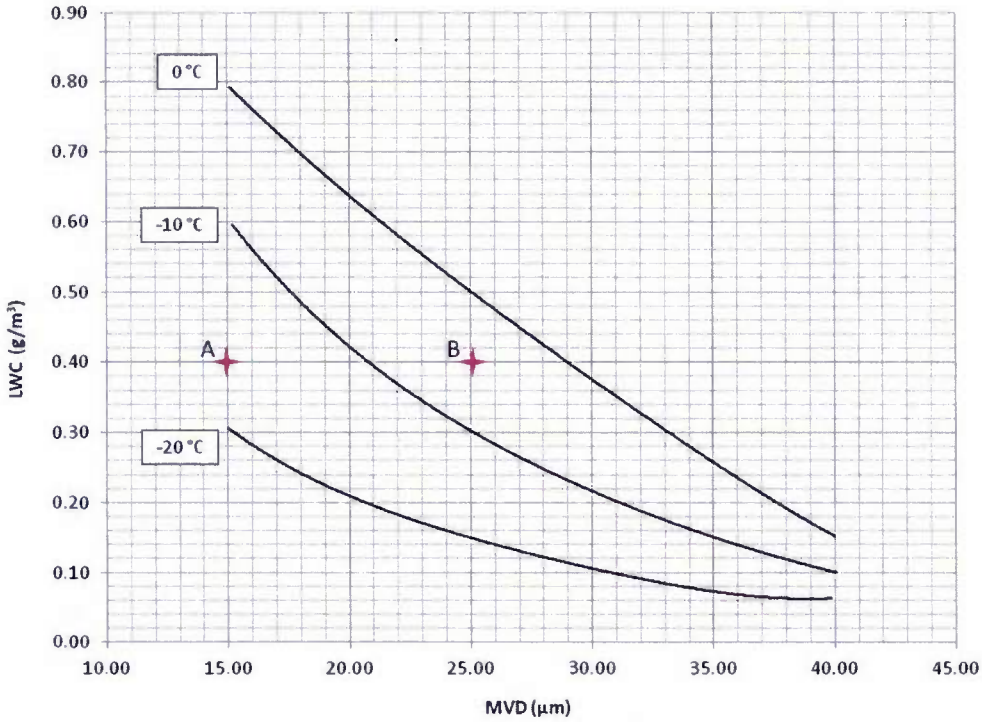

	Temperature (°C)	MVD (µm)	LWC (g/m^3)	RPM	Tip Speed (m/s)	Ice Thickness (in)
A	-15	15	0.4	500	65.8	0.32 ± 0.03
B	-8	25	0.4	500	65.8	0.32 ± 0.03

Figure 77: Icing conditions for de-icing comparison

As seen in Figure 78, the ice shape for case A and B are very similar. Judging by the color and shape of the ice, case A was in the rime regime and case B was in the mixed glaze-rime regime. The bridged ice form the unprotected area to the protected area had to be removed, to the ice over the IPS could release properly. After the ice was accreted but before the IPS was turned on, the ice over the unprotected areas was be separated from the ice over the protected region. Two cuts were made though the ice approximately one inch from both ends, because the heaters do not protect that area. Both de-icing

systems were tested under these two icing conditions, and the maximum and average root mean square (rms) power required to de-ice were compared.

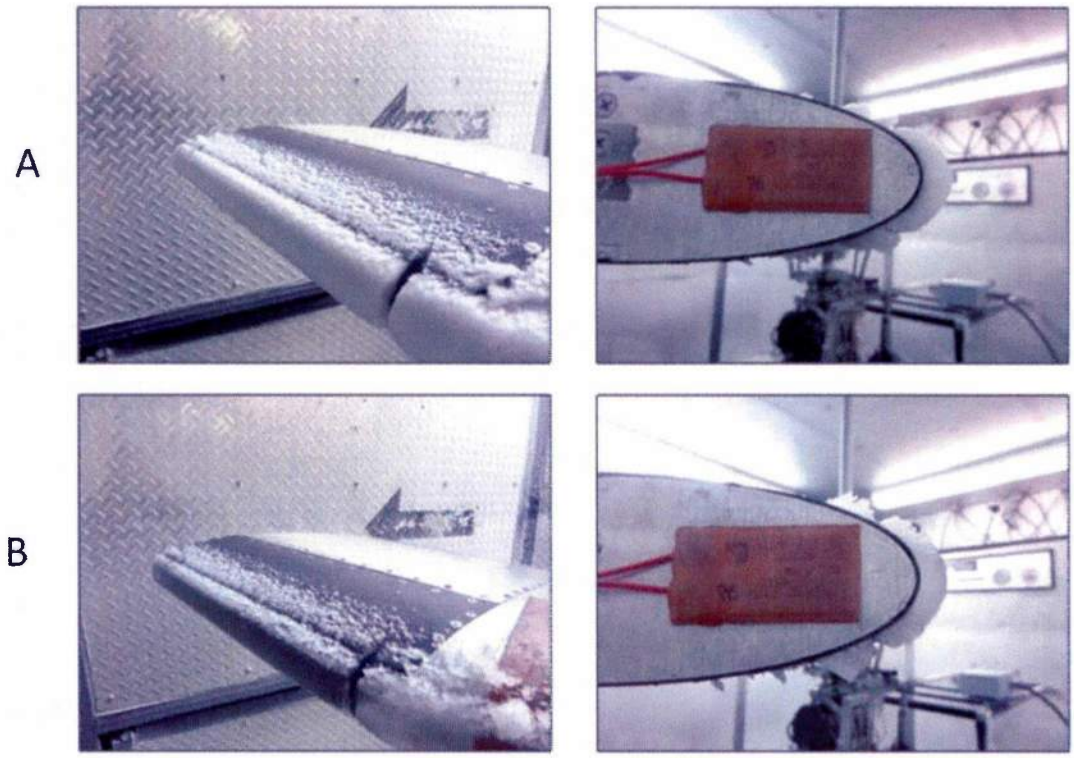

Figure 78: Side and angled view of ice geometry for case A & B

Since the potential benefit of the ultrasonic de-icing system is reduced power required as compared to conventional electrothermal de-icing, the electrothermal IPS was operated at both a traditional, relatively high, power level and a power level similar to that required power for ultrasonic system to de-ice. For the ultrasonic IPS to be beneficial, the ultrasonic IPS must outperform the electrothermal IPS at both power levels. The ultrasonic IPS was tested first to set the benchmark for the power required to de-ice the test paddle. As seen in Figure 79, the average rms power the ultrasonic IPS required to de-ice case B was 243 W_{rms}. Since ice adhesion strength increases as temperature decreases, the ultrasonic IPS required 289 W_{rms} of power to de-ice case A. The increase in required power from case B to case A was 20%.

For comparison, the electrothermal IPS was operated at similar powers as the ultrasonic IPS, 294 W_{rms} for case A and 249 W_{rms} for case B. Lastly, the electrothermal IPS was tested at a traditional power density of 25 W/in^2 (20). The power to each heater zone was 416 W. The ultrasonic IPS compared to the high power electrothermal IPS required 36% less power. However, the electrothermal IPS performed similarly to the ultrasonic IPS at equivalent power settings for both cases A and B.

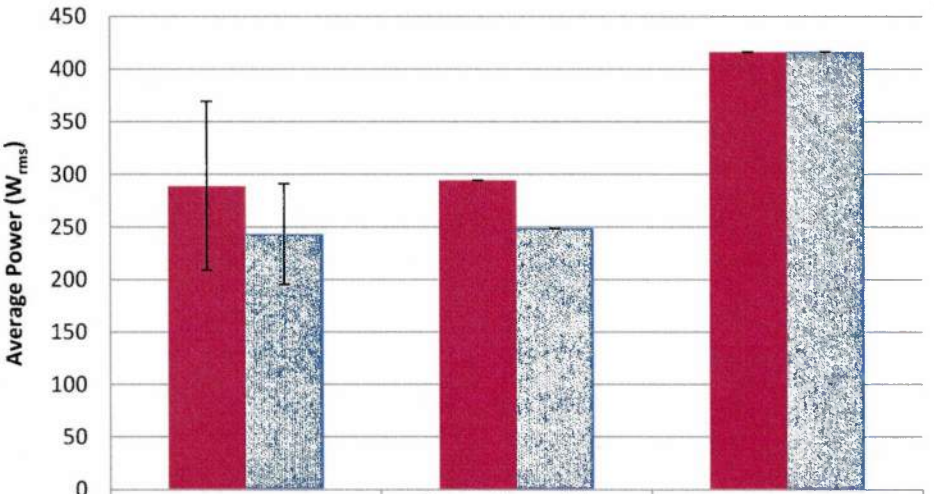

	Ultrasound	Electrothermal (low power)	Electrothermal (high power)
Case A	289	294	416
Case B	243	249	416

Figure 79: Average root mean square power to de-ice

As seen in Figure 80, the ultrasonic IPS and both the low and high power electrothermal IPSs were effective in de-icing the majority of the ice. For the warmer case, case B, the ultrasonic IPS removed the entire main ice body up to the inboard cut but did not remove all of the aft feather ice. At the colder temperature, case A, the main ice failed both adhesively and cohesively leaving behind some ice on the surface of the paddle as well as feather ice. At the low power setting, the electrothermal IPS cleanly removed the main ice at both temperatures but did not remove the large feathers at the colder temperature. At the high power setting, the electrothermal IPS removed all of the ice from the protected areas. Both IPSs required more power to de-ice at colder temperature, but the reason is different for each IPS. The

ultrasonic IPS required more power at colder temperatures because the ice adhesion strength increases as temperature decreases, and as a mechanical de-icing system, the ultrasonic IPS was dependant on ice adhesion strength. Since the electrothermal IPS must increase the temperature of the leading edge from the start temperature to well over 0°C, the colder leading edge starting temperature at colder atmospheric temperatures caused the power required to the electrothermal IPS to increase.

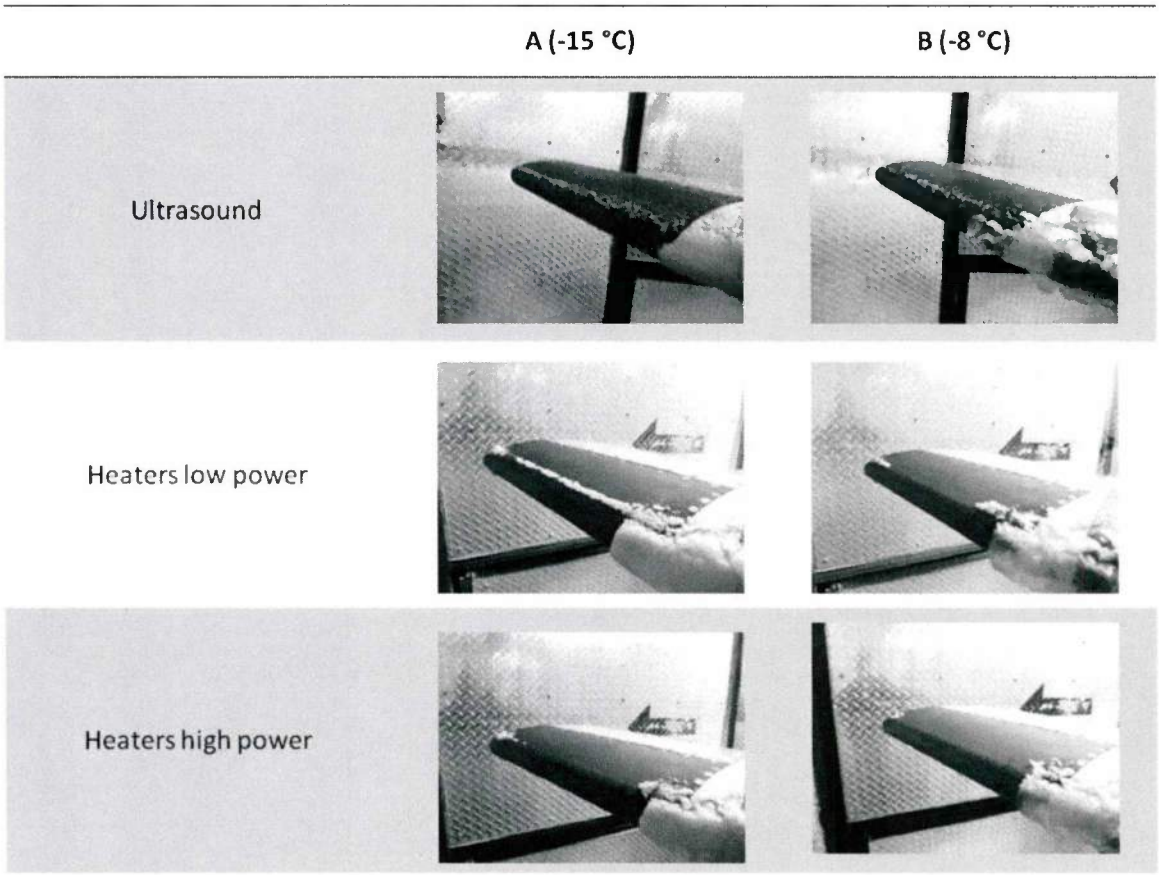

Figure 80: Post test pictures

The peak power is also of interest for the ultrasonic IPS because the amplifier did not supply a constant power to the actuators. The highest stresses were created at the peak power, and that is when the actuators were most likely to fail. As seen in Figure 81, the peak power used by the ultrasonic actuators for case A was 494 W_{rms} and was 70% higher than the average ultrasonic power, 68% higher than the low power electrothermal, and 19% higher than the high power electrothermal. The peak power used by the actuators for case B was 312 W_{rms} and was 28% higher than the average ultrasonic power, 25% higher

than the higher power electrothermal, and 25% lower than the high power electrothermal. If the ice was most affected at the peak power, then the power reduction from using an ultrasonic IPS over an electrothermal IPS diminishes.

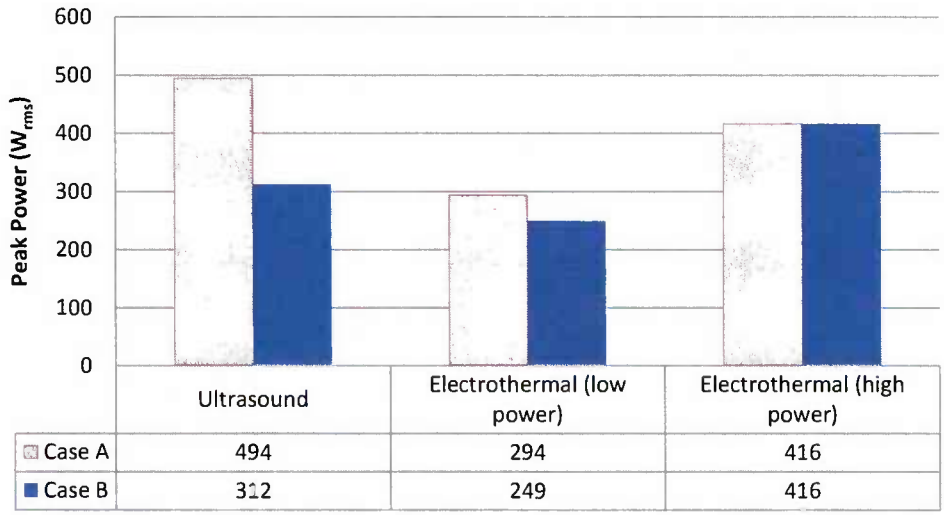

	Ultrasound	Electrothermal (low power)	Electrothermal (high power)
Case A	494	294	416
Case B	312	249	416

Figure 81: Peak power to de-ice

Even though the actuators were able to de-ice at colder temperatures, the actuators had to be driven at a voltage that exceeded the dynamic failure voltage. For case A, one of the actuators failed catastrophically. 15% of the volume of one of the actuators fractured and blew out. Also, the local temperatures increased well over the 180°F maximum operational temperature of the FM-73 adhesive because the resin liquefied and was ejected resin from the bondline (see Figure 82). Once the actuator failed, the impedance of the system changed, resulting in a large impedance mismatch between the actuators and the amplifier. As a result most of the power from the amplifier was reflected back and no additional actuators were damaged. Testing of the ultrasonic system was halted after the actuator failed.

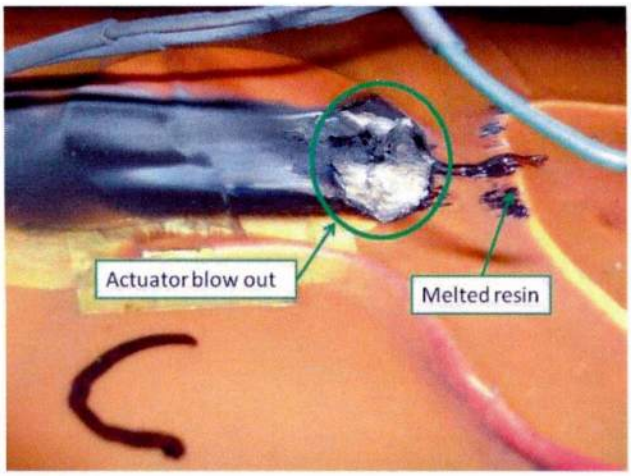

Figure 82: Failed actuator region after over powering the system

The stress in the actuators is proportional to the voltage applied. To de-ice case A, the maximum rms voltage peaked at 253 V_{rms} from the amplifier. An approximate failure rms voltage was estimated to be 15% below the maximum voltage. It is recommended that the piezoelectric PZT-4 disk actuators operating at the ultrasonic radial resonance and running in compression only, not be driven with rms voltages greater than 215 V_{rms}.

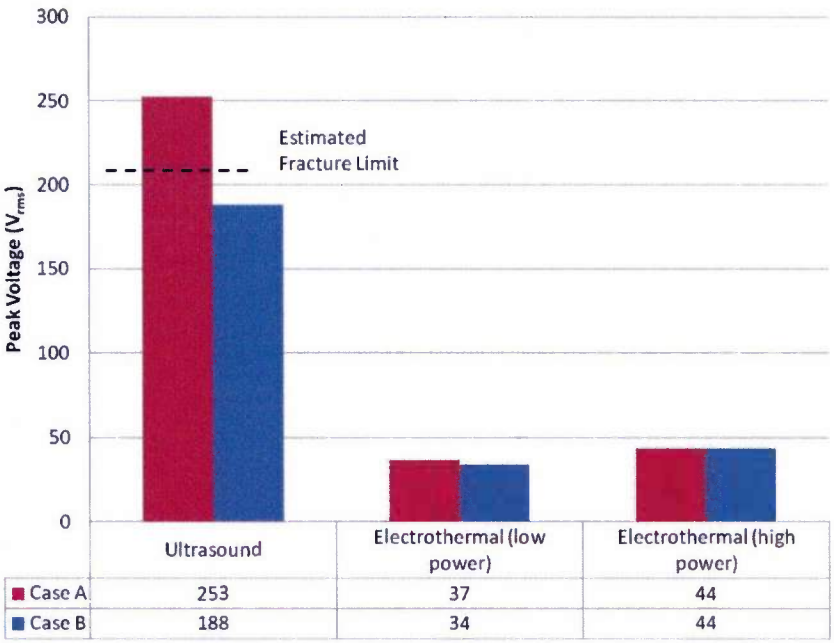

Figure 83: Maximum applied voltage rms

Two factors that may have skewed the results were the rotor speed and the ice adhesion strength. Although the test facility can match centrifugal forces comparable to full size rotorcraft, the test stand cannot match air speeds. The flow over the out board sections of the blades of a full-scale helicopter are much greater than the flow over the experimental de-icing blades. The higher airflow over a full size blade will increase convective cooling. More convective cooling means more power to the electrothermal IPS to reach the same temperature. The ultrasonic IPS relies on mechanical forces and is not affected by the air flow over the blade. The ice adhesion strength to the surface is very important to mechanical de-icing systems such as ultrasound and has little affect on electrothermal systems. The higher the adhesion strength the more power was required for the ultrasonic IPS to de-ice. As discussed in the previous chapter, the TiAlN coating used on the exterior of the leading edge cap was not optimized and had a high adhesion strength. The manufacturing process for the TiAlN can be optimized to reduce the ice adhesion strength and in turn reduce the power required for ultrasonic IPS. The low airflow over the blades and the high ice adhesion coating tend to favor the electrothermal IPS. Once the TiAlN coating is refined, the experimental comparison between ultrasound and electrothermal IPS should be repeated.

4.5. Qualitative Comparison

- Power Required

  With the current TiAlN coating that was not optimized for low ice adhesion strength, the power required to de-ice was the same for both the electrothermal and ultrasonic systems. Once the ice adhesion strength on the TiAlN coating is decreased by reducing surface roughness the power required for the ultrasonic IPS should decrease more than the electrothermal system making ultrasound the preferred IPS.

- Fabrication

  Both the ultrasonic and electrothermal de-icing systems utilize composite manufacturing techniques. Both layups are simple and require few curing cycles. The difference between the two de-icing systems is the type of stress the composite must handle. It is favorable to use composite with a high operational temperature limit for the electrothermal IPS so the heating elements can

run hotter without the chance of melting the resin. The down side to high temperature composites is the high temperature required to cure. In comparison, the FM-73 film adhesive used for the ultrasonic IPS must transfer shear stress from the actuator efficiently without debonding. As discussed earlier, the film adhesive must be selected such that the shear modulus maximizes the amount of transferred shear stress for optimum performance.

- Driver Complexity

The driving system for the ultrasonic IPS is much more complicated than the driving system for the electrothermal IPS. The software for the ultrasonic must interact with four devices to monitor the dynamics of the IPS and power the actuators. The impedance analyzer must run a frequency sweep for each de-icing zone. Then, the software determines the optimal frequency to operate. Next, the amplifier tries to match the impedance of the de-icing zone and power the actuators. Using generic laboratory amplifiers and impedance analyzers that are not optimized for this de-icing system makes the driving process slow. The high power electricity must also be managed so it does not destroy the impedance analyzer or computer while driving the actuators. The controller of the electrothermal IPS is a straight forward program that only has to open and close a few relays, one for each heater zone, in a preset order and amount of time. The heater zone order, power on time, and delay are simple inputs making a wide range of power configuration.

5. Conclusions and Future Work

5.1. Conclusions

5.1.1. Tailored Stress Concentrators

The first part of this research experimentally and numerically evaluated the idea that additive discontinuities could increase dynamic stresses for the ultrasonic de-icing system. Axisymmetric finite element models where used to evaluate the optimal location for the stress concentrators. Then a finite element model was created to predict the de-icing performance of a bench top experimental model.

Lastly, the experimental results were compared to the finite element model and the feasibility of tailored stress concentrators was evaluated. The conclusions drawn from this research are as follows:

- Initial finite element models of tailored stress concentrators showed an increase in average interfacial shear stress of 20% if placed at stress minimum. The results are representative of an idealized structure fully covered by ice, which is not representative of helicopter rotor blades, where only the leading edge region accretes ice. The initial models could not be fabricated for testing, so a second set was made.
- The finite element models used for bench top testing showed tailored stress concentrators increase the local stress at the edge of the concentration but decrease the average ice interfacial shear stress by 9%.
- Experiments show the addition of tailored stress concentrations do not decrease the required power to de-ice for a round plate bench top configuration.
- Axisymmetric finite element models of the piezoelectric actuator and plate system have been validated; however, when ice is added to the model the FEA cannot predict the proper out-of-plane velocities or impedance. The model assumption that that ice is uniform and homogeneous may not be valid.

Since finite element models showed tailored stress concentrators only increase the average interfacial shear stress for very specific systems, and experiments showed there was no reduction in power required to de-ice, additive tailored stress concentrators as researched here may not beneficial. Even if the tailored stress concentrators could significantly increase the interfacial shear stress, it would be difficult to manufacture this type of stress concentration into highly curved structures such as helicopter blade leading edges, since the stress concentrators must be placed at low stress locations at the ice formation interface.

5.1.2. Ice Adhesion Strength of Erosion Resistant Materials

In this research, the ice adhesion strength of impact ice to erosion-resistant materials was experimentally measured and compared to that of metallic materials commonly used in helicopter rotor blade leading edges. In addition, the effects of environmental and material surface properties to ice adhesion strength were determined. The conclusions made from this research are as follows:

- The surface roughness of erosion resistant materials is of most importance to ice adhesion performance. Comparing the TiAlN to the uncoated baseline metallic materials at the lowest surface roughness value, TiAlN has a 59% higher impact ice adhesion strength than the average uncoated metallic materials. To have better performance, the TiAlN must be manufactured with less surface roughness.
- The rotor testing procedure based on beam bending due to centrifugal loading used to measure impact ice adhesion strength is as accurate as other experimental procedures with a standard deviation of less than 20%.
- Ambient temperature and surface roughness are the two most influential parameters for impact ice adhesion strength. It has been shown that impact ice adhesion strength can increase up to a factor of 6.7 from -8°C to -16°C, and up to a factor of 2.5 from 20 μin Ra to 100 μin Ra.
- Over the entire icing envelop tested, the impact ice adhesion strength of TiAlN is 70% higher than the average adhesion strength of all the erosion resistant materials tested and TiN is 33% higher than the average adhesion strength of all the erosion resistant uncoated metallic materials tested.
- It is possible to predict impact ice adhesion strength to within 22% for a variety of surface roughness values by empirically extrapolating from a known ice adhesion strength value if the ice adhesion strength temperature dependence is known.

The trend toward increasingly more erosion-resistant leading caps will continue as new coating systems are developed. During the development process, impact ice adhesion strength performance must be taken into consideration. To decrease the ice adhesion strength of TiAlN and TiN, the coating systems will have to be manufactured in such a way that the surface roughness is minimized. Minimizing surface roughness while increasing erosion resistance is the key to developing the next generation of rotor blade leading edge caps.

5.1.3. Comparison of Electrothermal and Ultrasonic IPS

Electrothermal and ultrasonic piezoelectric IPSs have been compared side by side for the first time during this research. Both systems were compared using a TiAlN coated erosion cap. As mentioned this erosion cap has ice adhesion strength values close to 60% larger than other metals, and as expected, mechanical de-icing systems relying in excess ice interface transverse shear stress to debond the ice, such as ultrasonic de-icing, performed poorly as compared to results obtained to standard isotropic materials. The two systems were tested at two different icing conditions and the power required to de-ice and the robustness of the systems were compared. After the completion of the experimental evaluation the following conclusions are made:

- Both IPSs have similar de-icing performance at similar power given the high ice adhesion strength of the erosion resistant coating. The ultrasonic IPS required 289 W_{rms} of average power to de-ice at -15°C, and the electrothermal IPS could de-ice at -15°C using a power of 294 W_{rms}. At -8°C the ultrasonic IPS requires 243 W_{rms} of average power, and the electrothermal IPS can de-ice using a power of 249 W_{rms}.
- The power supplied to the electrothermal IPS can be increased to 416 W_{rms} to increase de-icing performance; however, the ultrasonic IPS is already operating near the actuator failure limits.

The ultrasonic IPS performed remarkably well considering the ultrasonic IPS is only a laboratory experiment and the electrothermal IPS is a production quality system. The current ultrasonic IPS has to operate right up to the failure limit of the PZT-4 actuator disk to provide de-icing. This negligible small

margin of safety leads to broken actuators when trying to de-ice at cold temperatures. The ultrasonic IPS will work better with a lower ice adhesion strength leading edge coating. With a better coating the power required for the ultrasonic IPS will decrease, and the actuators will not have to work so close to the failure limit. The electrothermal IPS is reliable, robust, and can be manufactured into complex structures. However, it still has the tradition problems of run back water and the chance to thermally damage the host structure.

5.2. Future Work

5.2.1. Expand Tested Icing Conditions for Ultrasonic IPS

Until this point the ultrasonic IPS has been tested under typical helicopter icing conditions covering the majority of the FAR part 29 appendix C. Experiments run by Overmeyer captured many icing conditions but were limited in quantifying the power required for different ice thicknesses and centrifugal *g* forces (39). Power required for three ice thicknesses was tested but only at one centrifugal force 390 *g's*. Additional studies should be conducted to obtain a higher resolution on the power required to de-ice different ice thicknesses. Also a study on power required to de-ice at lower centrifugal forces should be conducted to understand the performance of the ultrasonic IPS along the span of a helicopter blade or a fix-wing aircraft at zero centripetal force. The last icing condition that the ultrasonic IPS needs to be tested at is warm temperatures between 0°C and -5°C. Ice accreted at warms temperatures has a lot of runback prior to melting so the impinging limits move aft. Warm ice also has low stiffness making it hard for mechanical IPSs to create large enough stresses to delaminate the ice.

5.2.2. Low Ice Adhesion Erosion Coating

Decreasing the ice adhesion strength of the erosion coating will decrease the power required of the ultrasonic de-icing system. The ultrasonic actuators would not have to develop as much interfacial shear stress to delaminate the ice. To decrease the ice adhesion strength, the surface roughness of the erosion cap must decrease. There are two elements that affect the final erosion cap surface roughness: the substrate surface roughness and the coating manufacturing process. The substrate should be polished to

reduce surface roughness prior to the application of the erosion resistant coating. A limitation to reducing the surface roughness of the substrate is the reduction in adhesion strength of the coating. The substrate should be polished as much as possible to reduce ice adhesion strength without decreasing the integrity of the coating. The coating manufacturing process can also be modified to reduce surface roughness. The distance from the target to the arc and the magnetic field that controls the plasma flow should be adjusted to filter out large particles from building up on the substrate.

5.2.3. Thinner Leading Edge Skins

If the leading edge erosion cap is covered in a highly erosion resistant material, the thickness of the erosion cap substrate can be reduced to increase performance of electrothermal and ultrasonic de-icing systems. The thinner cap should allow the PZT actuators to introduce larger ice interface transverse shear stresses for less input power. However if the thickness is reduced significantly, the structure will become so compliant that the actuator will only be able to create stresses locally, reducing the protection area affected by a PZT actuator. An optimal erosion cap thickness should be determined for a specific system. A thinner erosion cap will also benefit the electrothermal IPS because the surface temperature will increase faster as the heat does not have to travel as far. Ideally, the heater elements should be placed on the surface to minimize the power required, but due to erosion concerns a very thin, highly erosion resistant, and thermally conductive material should be used as the erosion cap. In both IPSs the structural integrity of the rotor blade should be considered. Any loads that are typically carried by the leading edge skin will have to be transferred to a different part of the structure.

5.2.4. Robust Ultrasonic Actuators - Magnetostrictive IPS

Current PZT actuators used for ultrasonic de-icing are working right up to the limit of the material at difficult icing conditions (low temperatures, i.e. < -15°C). If the actuators are driven too hard and over heat, the actuators will easily catastrophically fail (see Figure 84). PZT is not a robust enough material to build reliable ultrasonic IPS. To adress this problem a new material for the ultrasonic actuators should be studied.

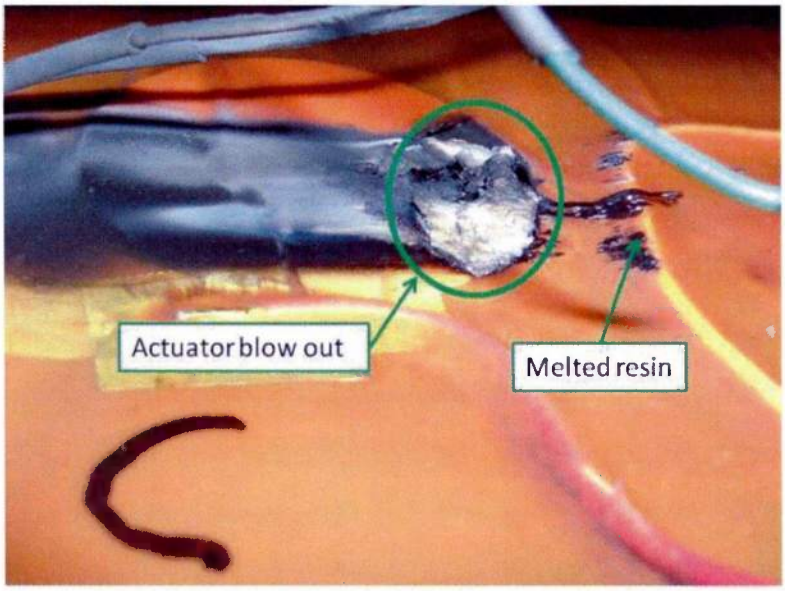

Figure 84: Failed actuator region after over powering the system

Another smart material similar to PZT that can be used as an actuator is a magnetostrictive material. A magnetostrictive material strains when in proximity to a magnetic field. When the magnetic field is applied, the magnetic domains of the material rotate to align with the applied magnetic field. The material will strain as the magnetic domains rotate. To make a simple actuator, wire is wound around a rod of magnetostrictive material and alternating current is applied to the coil of wire. The rod will vibrate axially, and this motion can be used to make an actuator. Rods can be placed in the nose of the leading edge cap to vibrate the erosion cap to create stress that will delaminate ice (see Figure 85). A conformal adapter will have to interface the rod to the complex curvature of the leading edge nose. Since magnetostrictive material is brittle (similar to PZT), the span-wise bending stress in the blade will have to be understood so the rods are segmented and placed strategically such that they do not break under blade bending load.

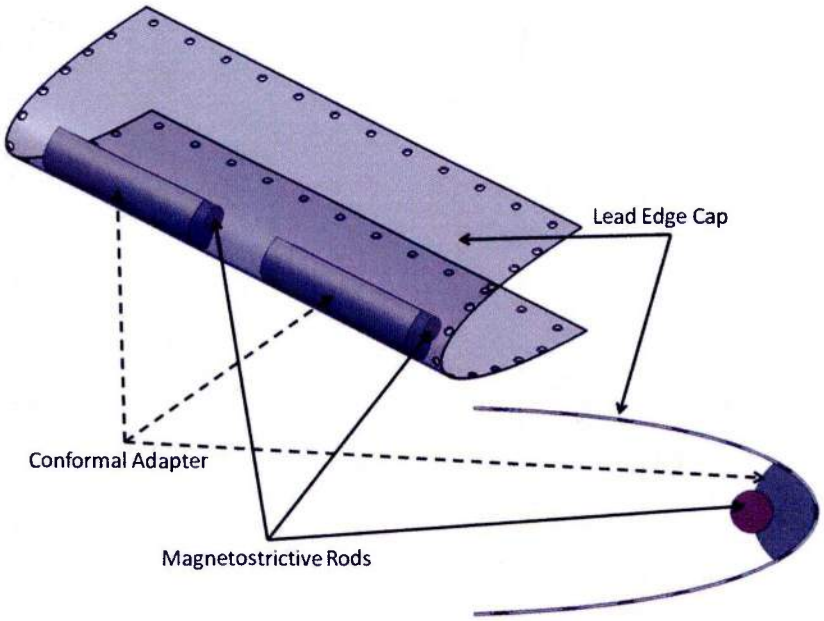

Figure 85:Magnetostrictive IPS

References

1. Leary, William M.,We Freeze to Please: A History of NASA's Icing Research Tunnel and Quest for Flight Saftey: The NASA History Series, 2002 , Vols. NASA SP-2002-4226.

2. Boeing. Boeing Research Aero-Icing Tunnel. Boeing Technology Services. [Online] http://www.boeing.com/boeing/commercial/techsvcs/boeingtech/bts_aerof.page.

3. Herman, E., Goodrich Icing Wind Tunnel Overview, Improvements and Capabilities. Reno, NV : 44th American Institute of Aeronautics and Astronautics Aerospace Science Meeting and Exhibit, AIAA-2006-862, 2006.

4. Al-Khalil, K. Salamon, L. Tension, G., Development of the Cox icing Reserach Facility. Reno, NV : 36th AIAA Aerospace Science Meeting and Exhibit, AIAA-98-0097, 1998.

5. Ragni, A. et al., Calibration of the CIRA IWT in the High Speed Configuration. Reno, NV : 43rd AIAA Aerospace Sciences Meeting and Exhibit, AIAA-2005-471, 2005.

6. Bailey, D.L., Samolewicz, J.J., MacPhail, D.C. Description of the Spray Rig Used to Study Icing on Helicopters in Flight : Laboratories, Ottawa, Canada : Division of Mechanical Engineering, Low Temperature Laboratory, 1960. LR-186A, File M4-A3-R26.

7. Peterson, A., Oldenburg, J., Spray Nozzle Investigation for the Improved Helicopter Icing Spray System (IHISS). Reno, NV : AIAA 28th Aerospace Sciences Meeting, AIAA-90-0666., 1990.

8. Bell, J., Icing at the McKinley Climatic Laboratory. Reno, NV : 41st Aerospace Sciences Meeting and Exhibit AIAA-2003-902, Jan. 6-9, 2003.

9. Palacios, J., Han, Y., Brouwers, E., Smith, E., Icing Environment Rotor Test Stand Liquid Water Content Measurement Procedures and Ice Shape Correlation. American Helicopter Society Journal (Paper # 1562),

10. Brouwers, E. The Experimental Investigation of a Rotor Icing Model with Shedding. University Park, PA : MS Thesis, The Pennsylvania State University, Department of Aerospace Engineering, May 2010.

11. Han, Y. Theoretical and Experimental Study of Scale Methods for Rotor Blade Ice Accretion Testing. Unversity Park, PA : Masters Thesis, The Pennsylvania State University, Department of Aerospace Engineering, August 2011.

12. Ruff, G. and Berkowitz, B. Users Manual for NASA Lewis Ice Accretion Prediction Code. 1990. NASA CR 185129.

13. Federal Aviation Regulation Part 25 "Airworthiness Standards: Transport Category Airplanes" and Part 29 "Airworthiness Standards: Transport Category Rotorcraft", FAA, Washington DC.

14. Han, Y. and Palacios, J., Analytical and Experimental Determination of Airfoil Performance Degradation due to Ice Accretion. New Orleans : AIAA, 2012. AIAA 2012-2794.

15. Gent, R., Dart, N. and Candsdale, J., Aircraft Icing: Philosophical Transactions of the Royal Society of London Series, 2000, Vol. 358.

16. Brouwers, E. Peterson, A. Palacios, J. Centolanza, L., Ice Adhesion Strength Measurements for Rotor Blade Leading Edge Materials. Virginia Beach, VA : AHS-2011-272.

17. Burkett, B., Ice Phobic Coatings on Controlled and Covered Surfaces. Fort Worth , American Helicopter Society 68th forum, 2012.

18. Coffman, H., Helicopter Rotor Icing Protection Methods, Journal of the American Helicopter Society, April 1987, Vol. 32.

19. Buschhorn, S. et al., Electrothermal Icing Protection of Aerosurfaces uing Conductive Polymer Nanocomposites. Boston, AIAA, 2013. AIAA 2013-1729.

20. Flemming, R., A History of Ice Protection System Development at Sikorsky Aircraft. Chicago, IL : FAA In-Flight Icing/Ground De-Icing International Conference and Exhibition, 2003. 2003-01-2092.

21. Botura, G., Sweet, D., and Flosdorf, D. Development and Demonstration of Low Power Electrothermal De-icing System. Reno, NV : 43rd AIAA Aerospace Sciences Meeting and Exhibit, 2005. AIAA 2005-1460.

22. Magenheim, B., Demonstration of the Microwave Ice Protection Concept. Fort Eustis, Virginia : Applied Technology Laboratory, U.S. Army Research and Technology Laboratories, May 1978. USAAMRDL-TR-77-34.

23. Feher, L. and Thumm, M., High Frequency Microwave Anti-De-Icing System for Carbon Reinforced Airfoil Structures: Proceedings of SPIE, 2001, Vol. 4371. 0277-786X.

24. Norbert, W., Design of an Advanced Pneumatic Deicer for Composite Rotor Blade: Journal of Aircraft, 1989 , Vols. 26 pp.947-950.

25. Schulz, M., Riemenschneider, J., and Palacios, J., Investigation of Active Twist Rotor for Blade De-Icing. Phoenix: 2013. 69th AHS International Forum.

26. Goehner, R., Glover,N., Hensley D., Electro-Impulse-Deicing-EIDI : ERDC/CRREL TR-09-X, 1987.

27. . Overmeyer, A.,Palacios, J., Smith, E., Rotating Testing of a Low-Power, Non-Thermal Ultrasonic De-icing Sysytem for Helicopter Rotor Blades: SAE Internaltional, 2011. 2011-38-0098.

28. Palacios, J., Smith, E., Rose, J., and Royer, R., Instantaneous De-Icing of Freezer Ice via Ultrasonic Actuation: AIAA Journal , June 2011, Vol. 49.

29. Palacios, J., Smith, E., Rose, J., and Royer, R.,Ultrasonic De-Icing of Wind-Tunnel Impact Icing : Journal of Aircraft, 2011, Vol. 48.

30. Venna, S., Lin, Y., and Botura, G., Piezoelectric Transducer Actuated Leading Edge De-Icing with Simultaneous Shear and Impulse Forces: Journal of Aircraft, 2007, Vols. 44, pp. 509-515.

31. Palacios, J.L. Design, Fabrication, and Testing of an Ultrasonic De-Icing System for Helicopter Rotor Blades. University Park, PA : PhD Thesis, The Pennsylvania State University, Department of Aerospace Engineering, May 2008.

32. US Army Research Laboratory. ARL's new cold spray compound looks promising as helicopter sand erosion solution in harsh desert terrain. ARL News. [Online] 2011. http://www.arl.army.mil/www/default.cfm?page=745.

33. Calvert, M., Wong, T., and James, A., Blade Contour Deformation and Helicopter Performance.: 24th Applied Aerodynamic Conference, 2006. AIAA 2006-3167.

34. Hamed, A., Tabakoff, W., and Wenglarz, R., Erosion and Deposistion in Turbomachinery. Cininnati : Journal of Propulsion and Power, 2006, Vol. 22.

35. Aquaro, D. and Fontani, E.,Erosion of Ductile and Brittle Materials: Meccanica, 2001, Vol. 36.

36. Trexler, M. and Kopchik, J., Development of a Novel Erosion Resistant Coating Sysytem for use on Rotorcraft Blades: Fort Worth, AHS International 68th Forum, 2012.

37. [Online] Hontek. http://www.rain-sand-erosion.com/ps.html.

38. Zhu, Y. Palacios, J., Rose, J., Smith, E., Numerical Simulation and Experimential Validation of Tailored Wave Guides for Ultrasonic De-icing and Aluminum Plates: The Pennsylvania State University, 2010.

39. Overmeyer, A., Actuator Bondline Optimization and Experimental Deicing of Rotor Blade Ultrasonic Deicing System: Masters Thesis, Pennsylvania State University, 2012.

40. Borawski, B., Multilayer Erosion Resistant Coatings for Protection of Aerospace Componants: PhD Disseration, Pennsylvania State University, 2011.

41. Laforte, C. and Beisswenger, A. Icephobic Material Centrifuge Adhesion Test. Montreal. International Workshop on Atmospheric Icing on Structures. 2005.

42. Hassan, M., Lee, H., and Lim, S., The variation of ice adhesion strength with substrate surface roughness: Measurment Science and Technology, Vol. 7.

43. Reich, A., Interface Influences Upon Ice Adhesion to Airfoil Materials: 32nd Aerospace Sciences Meeting and Exhibit, Reno, NV 1994 : AIAA 94-0714.

44. Bond, J. and Shin, T., Results of an icing test on a NACA 0012 Airfoil in the NASA Lewis Icing Reseach Tunnel. Reno : 1992. 30th Aerospace Sciences.

45. Stallabrass, J. and Price, R., On the Adhesion of Ice to Various Materials. Ottawa, CA : National Research Laboratory, 1962. LR-350, M4-A3-R26.

46. Tsao J., Kreeger R., Evaluation of Scaling Methods for Rotorcraft Icing. NASA/TM-2010-215801.

47. Overmeyer, A., Actuator Bondline Optimization and Experimental Deicing of Rotor Blade Ultrasonic Deicing System.: Pennsylvania State University , 2012.

Distribution List

(a) Applied Research Laboratory
The Pennsylvania State University
Attn: Dr. Douglas E. Wolfe
PO Box 30
University Park, PA 16804
Email: dew125@arl.psu.edu

(b) Defense Technical Information Center (DTIC)
Attn: DTIC-BSC
8725 John J. Kingman Road, Suite 0944
Fort Belvoir, VA 22060-0944
Email: TR@dtic.mil

(c) The Pennsylvania State University
Attn: Jose Palacios
Dept. of Aerospace Engineering
Email: jlp324@psu.edu